ABSTRACT

HART, NATHAN HENRY. A Residual-Based *A Posteriori* Spatial Error Estimator for the S_N Neutron Transport Equation. (Under the direction of Yousry Azmy.)

Error estimators determine the reliability of discretized numerical methods; as numerical simulations evolve to represent more and more complex systems, validation of the approximations becomes essential, and this step is often overlooked. Within a specific energy and S_N angular discretization of the neutron transport equation, estimators of the spatial discretization error are relied upon for adaptive mesh refinement and propagation of error analysis. *A posteriori* estimators have the benefit of high accuracy, but they often sacrifice computational resources to achieve this. In this work, a mathematically sound two-step estimator is introduced and applied to test problems. The "residual source estimator" uses an approximation of the residual as a fixed source for a transport-like problem, in which the discretization error is estimated using the same transport routines as the discretized angular flux solution. A detailed derivation of the residual, an approximation of the residual by Taylor series expansion, and an approximation of higher-order derivatives using low-order solutions are detailed to demonstrate practical application of such an estimator.

The resultant error estimation for the Discontinuous Galerkin Finite Element Method of order 0 discretization is compared for several cases with varying optical thickness (total cross-section), scattering ratio, and solution regularity. The residual source estimator is compared against two estimators that have been shown to perform well: the "Ragusa-Wang" estimator and the "DAZ" estimator/indicator. By using the Method of Manufactured Solutions, true reference solutions provide an objective basis for determining the quality of the estimator. The local behavior of estimators relative to the true error is observed via an "effectivity index", and global quantities, namely, the global effectivity index, fraction of local estimates that overestimate the true error, fraction of local estimates within some accuracy bound, and standard deviation of the effectivity index give some indication of the advantages of each estimator.

The performance of the residual source estimator is encouraging. For problems with solutions in H^1 (true solution discontinuous in its first derivative along the singular characteristics), the residual source estimator is generally accurate, precise, and computationally affordable compared to similarly performing estimators. For problems with solutions in H^0 (true solution itself is discontinuous along the singular characteristics), the residual source estimator is competitive versus other estimators, but it suffers in problems that are adversely affected to a significant level by the discontinuity.

A Residual-Based *A Posteriori* Spatial Error Estimator for the S_N Neutron Transport Equation

by
Nathan Henry Hart

A thesis submitted to the Graduate Faculty of
North Carolina State University
in partial fulfillment of the
requirements for the Degree of
Master of Science

Nuclear Engineering

Raleigh, North Carolina

2018

APPROVED BY:

Dmitriy Anistratov	Zhilin Li
Jon Dahl External Member	Yousry Azmy Chair of Advisory Committee

DEDICATION

To my parents.

BIOGRAPHY

Born and raised in the south suburbs of Chicago, Illinois, to Paul and Deborah Hart, the author took an interest in engineering by playing with LEGOs and watching Mythbusters and narrowed his interests to nuclear engineering after spending many nights playing the Fallout game series in high school. Inspired by the Western scenery, he attended The University of New Mexico in Albuquerque, where he graduated *cum laude* in 2015 with his Bachelors of Science in nuclear engineering in addition to meeting his wife, Lindsey. While in Albuquerque he worked at the Gamma Irradiation Facility at Sandia National Laboratories under Dr. Maryla Wasiolek and Don Hanson doing MCNP modeling of the Low Intensity Cobalt Array. He was introduced to computational neutron transport by Dr. Anil Prinja at UNM, and elected to pursue these studies for a Doctorate degree in nuclear engineering.

He currently works towards this goal at North Carolina State University under Dr. Yousry Azmy, and he is supported by the Consortium for Nonproliferation Enabling Capabilities (CNEC) and a Nuclear Energy University Programs (NEUP) Fellowship. He is also working towards a Nuclear Nonproliferation Science and Policy Graduate Certificate at NCSU. He has spent two recent summers in New Mexico working at Los Alamos National Laboratory under Dr. Jon Dahl on neutron lifetime studies in the deterministic transport code PARTISN, and he plans to return again in summer, 2018. The author likes to spend his time by planning wilderness backpacking trips, playing bass and guitar, managing fantasy football teams, and looking for new historic military arms to add to his collection.

ACKNOWLEDGEMENTS

My sincerest appreciation goes to my friends and family who have supported me during my time on earth, especially my parents and my beautiful wife Lindsey. I owe more than I could ever express in words, and I hope this thesis can be seen as a return on investment of sorts for your dedication. I would also like to thank all my professors, teachers, and advisors throughout my entire educational career, particularly my graduate advisor Dr. Yousry Azmy. In addition, I would like to thank Dr. Sean O'Brien and Dr. Sebastian Schunert for helping me understand the basics of this work as well as Dr. Jose Duo for working with me closely on some of the later aspects of the work and for continued advice warranting a role as a technical consultant for this thesis.

This material is based upon work supported under a Department of Energy, Office of Nuclear Energy, Integrated University Program Graduate Fellowship. Any opinions, findings, conclusions or recommendations expressed in this publication are those of the authors and do not necessarily reflect the views of the Department of Energy Office of Nuclear Energy.

"The only thing I know, is that I know nothing."

– Attributed to Socrates

"If I can stuff my mouth with enough salami, I won't be able to answer any difficult questions."

– Mark, from Peep Show

TABLE OF CONTENTS

LIST OF TABLES . . . . **vii**

LIST OF FIGURES . . . . **viii**

Chapter 1 Background **1**
- 1.1 *A Posteriori* Spatial Discretization Error Estimation 1
- 1.2 Residual-Based Error Estimators 3
- 1.3 Estimators *vs.* Indicators *vs.* Bounds 6
- 1.4 Motivation 7

Chapter 2 Introduction **8**
- 2.1 The Neutron Transport Equation 8
- 2.2 DGFEM-Λ 9
- 2.3 Method of Manufactured Solutions 10
- 2.4 Discretization Error 12

Chapter 3 Residual Source Estimator **15**
- 3.1 Derivation of the Residual and Estimator 15
- 3.2 Empirical Proof of Validity 16
- 3.3 Observed Convergence of Residual and Error 20

Chapter 4 Approximating the Residual **24**
- 4.1 Taylor Expansion Approximation 24
  - 4.1.1 Derivation 24
  - 4.1.2 Resultant Residual and Error Approximation 29
- 4.2 Approximating Derivatives 33
  - 4.2.1 Derivation 33
  - 4.2.2 Resultant Residual and Error Approximation 35

Chapter 5 Alternative Estimators **39**
- 5.1 Ragusa-Wang Estimator 39
- 5.2 Duo-Azmy-Zikatanov Estimator and Indicator 41

Chapter 6 Estimators Comparison and Assessment for H^1 Problems **44**
- 6.1 H^1 Case Study 44
  - 6.1.1 H^1 Case 1 44
  - 6.1.2 H^1 Case 2 59
  - 6.1.3 H^1 Case 3 67
- 6.2 H^1 General Behavior 75
- 6.3 H^1 Conclusions 86

Chapter 7 Estimators Comparison and Assessment for H^0 Problems **88**
- 7.1 H^0 Case Study 88
  - 7.1.1 H^0 Case 1 88
- 7.2 H^0 General Behavior 99
- 7.3 H^0 Conclusions 102

Chapter 8 Conclusions **108**

Bibliography **111**

LIST OF TABLES

Table 2.1 S_4 Level-Symmetric Quadrature/Octant 8
Table 2.2 MMS Boundary Conditions 12

LIST OF FIGURES

Figure 2.1 SCs for Level Symmetric S_4 Quadrature 12

Figure 3.1 $\log_{10} \theta^{(i,j)}_{ang.}$ Histogram for LeR/MMS 17
Figure 3.2 $\log_{10} \theta^{(i,j)}_{sca.}$ Histogram for LeR/MMS 17
Figure 3.3 $\log_{10} |R^0_h(x,y)|$ in Quadrant 1, $\mu_n = \eta_n = 0.35002$, $N_X = N_Y = 32$ 18
Figure 3.4 $\log_{10} |R^0_h(x,y)|$ in Quadrant 1, $\mu_n = 0.35002$, $\eta_n = 0.86889$, $N_X = N_Y = 32$ 18
Figure 3.5 $\log_{10} |R^0_h(x,y)|$ in Quadrant 1, $\mu_n = 0.86889$, $\eta_n = 0.35002$, $N_X = N_Y = 32$ 18
Figure 3.6 Local $\log_{10}$-Angular L_2 Norm of Solution Error, $N_X = N_Y = 32$ 19
Figure 3.7 Local $\log_{10}$-Scalar L_2 Norm of Solution Error, $N_X = N_Y = 32$ 19
Figure 3.8 $\log_{10} |R^0_h(x,y)|$ in Quadrant 1, $\mu_n = \eta_n = 0.35002$, $N_X = N_Y = 512$ 19
Figure 3.9 $\log_{10} |R^0_h(x,y)|$ in Quadrant 1, $\mu_n = 0.35002$, $\eta_n = 0.86889$, $N_X = N_Y = 512$ 19
Figure 3.10 $\log_{10} |R^0_h(x,y)|$ in Quadrant 1, $\mu_n = 0.86889$, $\eta_n = 0.35002$, $N_X = N_Y = 512$ 20
Figure 3.11 Local $\log_{10}$-Angular L_2 Norm of Solution Error, $N_X = N_Y = 512$ 20
Figure 3.12 Local $\log_{10}$-Scalar L_2 Norm of Solution Error, $N_X = N_Y = 512$ 20
Figure 3.13 Local L_∞ spatial norm residual convergence in domain 21
Figure 3.14 Local L_∞ spatial norm residual convergence on boundary 21
Figure 3.15 Local L_∞ spatial norm residual convergence on SC-influenced cell 21
Figure 3.16 Global L_2 norm residual convergence 22
Figure 3.17 Global L_2 norm error convergence 22

Figure 4.1 $\log_{10} \left| R^0_h(x,y) - \mathcal{R}^0_{h,\text{TE-MMS}}(x,y) \right|$ in Quadrant 1, $\mu_n = \eta_n = 0.35002$, $N_X = N_Y = 32$ 29
Figure 4.2 $\log_{10} \left| R^0_h(x,y) - \mathcal{R}^0_{h,\text{TE-MMS}}(x,y) \right|$ in Quadrant 1, $\mu_n = 0.35002$, $\eta_n = 0.86889$, $N_X = N_Y = 32$ 29
Figure 4.3 $\log_{10} \left| R^0_h(x,y) - \mathcal{R}^0_{h,\text{TE-MMS}}(x,y) \right|$ in Quadrant 1, $\mu_n = 0.86889$, $\eta_n = 0.35002$, $N_X = N_Y = 32$ 30
Figure 4.4 $\log_{10} \theta^{(i,j)}_{ang.}$ for LeR/TE-MMS, $N_X = N_Y = 32$ 30
Figure 4.5 $\log_{10} \theta^{(i,j)}_{sca.}$ for LeR/TE-MMS, $N_X = N_Y = 32$ 30
Figure 4.6 $\log_{10} \theta^{(i,j)}_{ang.}$ for LeR/TE-MMS, $N_X = N_Y = 512$ 31
Figure 4.7 $\log_{10} \theta^{(i,j)}_{sca.}$ for LeR/TE-MMS, $N_X = N_Y = 512$ 31
Figure 4.8 $\log_{10}(\theta^{(i,j)}_{ang.})$ Histogram for LeR/TE-MMS, $N_X = N_Y = 512$ 31
Figure 4.9 $\log_{10}(\theta^{(i,j)}_{sca.})$ Histogram for LeR/TE-MMS, $N_X = N_Y = 512$ 32
Figure 4.10 $\log_{10} \left| R^0_h(x,y) - \mathcal{R}^0_{h,\text{TE-AD}}(x,y) \right|$ in Quadrant 1, $\mu_n = \eta_n = 0.35002$, $N_X = N_Y = 32$ 35

Figure 4.11 $\log_{10}\left|R_h^0(x,y) - \mathcal{R}_{h,\text{TE-AD}}^0(x,y)\right|$ in Quadrant 1, $\mu_n = 0.35002$, $\eta_n = 0.86889$, $N_X = N_Y = 32$ . . . 35
Figure 4.12 $\log_{10}\left|R_h^0(x,y) - \mathcal{R}_{h,\text{TE-AD}}^0(x,y)\right|$ in Quadrant 1, $\mu_n = 0.86889$, $\eta_n = 0.35002$, $N_X = N_Y = 32$ . . . 36
Figure 4.13 $\log_{10}\theta_{ang.}^{(i,j)}$ for LeR/TE-AD Estimator, $N_X = N_Y = 32$ . . . 36
Figure 4.14 $\log_{10}\theta_{sca.}^{(i,j)}$ for LeR/TE-AD Estimator, $N_X = N_Y = 32$ . . . 36
Figure 4.15 $\log_{10}\theta_{ang.}^{(i,j)}$ for LeR/TE-AD Estimator, $N_X = N_Y = 512$ . . . 37
Figure 4.16 $\log_{10}\theta_{sca.}^{(i,j)}$ for LeR/TE-AD Estimator, $N_X = N_Y = 512$ . . . 37
Figure 4.17 $\log_{10}(\theta_{ang.}^{(i,j)})$ Histogram for LeR/TE-AD Estimator, $N_X = N_Y = 512$ . . . 37
Figure 4.18 $\log_{10}(\theta_{sca.}^{(i,j)})$ Histogram for LeR/TE-AD Estimator, $N_X = N_Y = 512$ . . . 38

Figure 5.1 Convergence of Estimated Solution vs. True Solution . . . 40

Figure 6.1 $\log_{10}\theta_{ang.}^{(i,j)}$ for LeR/TE-AD Estimator, H^1 Case 1, $N_X = N_Y = 32$ . . . 45
Figure 6.2 $\log_{10}\theta_{ang.}^{(i,j)}$ for RW Estimator, H^1 Case 1, $N_X = N_Y = 32$ . . . 45
Figure 6.3 $\log_{10}\theta_{ang.}^{(i,j)}$ for DAZ Indicator, H^1 Case 1, $N_X = N_Y = 32$ . . . 45
Figure 6.4 $\log_{10}\theta_{ang.}^{(i,j)}$ Histogram for LeR/TE-AD Estimator, H^1 Case 1, $N_X = N_Y = 32$ . . . 46
Figure 6.5 $\log_{10}\theta_{ang.}^{(i,j)}$ Histogram for RW Estimator, H^1 Case 1, $N_X = N_Y = 32$ . . . 46
Figure 6.6 $\log_{10}\theta_{ang.}^{(i,j)}$ Histogram for DAZ Indicator, H^1 Case 1, $N_X = N_Y = 32$ . . . 47
Figure 6.7 $\log_{10}\theta_{sca.}^{(i,j)}$ for LeR/TE-AD Estimator, H^1 Case 1, $N_X = N_Y = 32$ . . . 47
Figure 6.8 $\log_{10}\theta_{sca.}^{(i,j)}$ for RW Estimator, H^1 Case 1, $N_X = N_Y = 32$ . . . 47
Figure 6.9 $\log_{10}\theta_{sca.}^{(i,j)}$ Histogram for LeR/TE-AD Estimator, H^1 Case 1, $N_X = N_Y = 32$ . . . 48
Figure 6.10 $\log_{10}\theta_{sca.}^{(i,j)}$ Histogram for RW Estimator, H^1 Case 1, $N_X = N_Y = 32$ . . . 48
Figure 6.11 $\log_{10}\theta_{ang.}^{(i,j)}$ for LeR/TE-AD Estimator, H^1 Case 1, $N_X = N_Y = 512$ . . . 49
Figure 6.12 $\log_{10}\theta_{ang.}^{(i,j)}$ for RW Estimator, H^1 Case 1, $N_X = N_Y = 512$ . . . 49
Figure 6.13 $\log_{10}\theta_{ang.}^{(i,j)}$ for DAZ Indicator, H^1 Case 1, $N_X = N_Y = 512$ . . . 49
Figure 6.14 $\log_{10}\theta_{ang.}^{(i,j)}$ Histogram for LeR/TE-AD Estimator, H^1 Case 1, $N_X = N_Y = 512$ . . . 50
Figure 6.15 $\log_{10}\theta_{ang.}^{(i,j)}$ Histogram for RW Estimator, H^1 Case 1, $N_X = N_Y = 512$ . . . 51
Figure 6.16 $\log_{10}\theta_{ang.}^{(i,j)}$ Histogram for DAZ Indicator, H^1 Case 1, $N_X = N_Y = 512$ . . . 51
Figure 6.17 $\log_{10}\theta_{sca.}^{(i,j)}$ for LeR/TE-AD Estimator, H^1 Case 1, $N_X = N_Y = 512$ . . . 52
Figure 6.18 $\log_{10}\theta_{sca.}^{(i,j)}$ for RW Estimator, H^1 Case 1, $N_X = N_Y = 512$ . . . 52
Figure 6.19 $\log_{10}\theta_{sca.}^{(i,j)}$ Histogram for LeR/TE-AD Estimator, H^1 Case 1, $N_X = N_Y = 512$ . . . 52
Figure 6.20 $\log_{10}\theta_{sca.}^{(i,j)}$ Histogram for RW Estimator, H^1 Case 1, $N_X = N_Y = 512$ . . . 53
Figure 6.21 Angular Error/Estimator L_2 Norm Convergence for H^1 Case 1 . . . 53
Figure 6.22 Angular Effectivity Convergence for H^1 Case 1 . . . 54

Figure 6.23 Angular Error/DAZ Estimator Global L_2 Norm Convergence for H^1 Case 1 . . . 55
Figure 6.24 Scalar Error/Estimator Convergence for H^1 Case 1 . . . 55
Figure 6.25 Scalar Effectivity Convergence for H^1 Case 1 . . . 56
Figure 6.26 Computation Time for Angular Estimators, H^1 Case 1 . . . 56
Figure 6.27 Computation Time for Scalar Estimators, H^1 Case 1 . . . 57
Figure 6.28 $\log_{10}\theta^{(i,j)}_{ang.}$ for LeR/TE-AD Estimator, H^1 Case 2, $N_X = N_Y = 32$ . . . 59
Figure 6.29 $\log_{10}\theta^{(i,j)}_{ang.}$ for RW Estimator, H^1 Case 2, $N_X = N_Y = 32$ . . . 59
Figure 6.30 $\log_{10}\theta^{(i,j)}_{ang.}$ for DAZ Indicator, H^1 Case 2, $N_X = N_Y = 32$ . . . 59
Figure 6.31 $\log_{10}\theta^{(i,j)}_{ang.}$ Histogram for LeR/TE-AD Estimator, H^1 Case 2, $N_X = N_Y = 32$ . . . 60
Figure 6.32 $\log_{10}\theta^{(i,j)}_{ang.}$ Histogram for RW Estimator, H^1 Case 2, $N_X = N_Y = 32$ . . . 61
Figure 6.33 $\log_{10}\theta^{(i,j)}_{ang.}$ Histogram for DAZ Indicator, H^1 Case 2, $N_X = N_Y = 32$ . . . 61
Figure 6.34 $\log_{10}\theta^{(i,j)}_{ang.}$ for LeR/TE-AD Estimator, H^1 Case 2, $N_X = N_Y = 512$ . . . 62
Figure 6.35 $\log_{10}\theta^{(i,j)}_{ang.}$ for RW Estimator, H^1 Case 2, $N_X = N_Y = 512$ . . . 62
Figure 6.36 $\log_{10}\theta^{(i,j)}_{ang.}$ for DAZ Indicator, H^1 Case 2, $N_X = N_Y = 512$ . . . 62
Figure 6.37 $\log_{10}\theta^{(i,j)}_{ang.}$ Histogram for LeR/TE-AD Estimator, H^1 Case 2, $N_X = N_Y = 512$ . . . 63
Figure 6.38 $\log_{10}\theta^{(i,j)}_{ang.}$ Histogram for RW Estimator, H^1 Case 2, $N_X = N_Y = 512$ . . . 64
Figure 6.39 $\log_{10}\theta^{(i,j)}_{ang.}$ Histogram for DAZ Indicator, H^1 Case 2, $N_X = N_Y = 512$ . . . 64
Figure 6.40 Angular Error/Estimator L_2 Norm Convergence for H^1 Case 2 . . . 65
Figure 6.41 Angular Effectivity Convergence for H^1 Case 2 . . . 65
Figure 6.42 Scalar Error/Estimator L_2 Norm Convergence for H^1 Case 2 . . . 66
Figure 6.43 Scalar Effectivity Convergence for H^1 Case 2 . . . 66
Figure 6.44 $\log_{10}\theta^{(i,j)}_{ang.}$ for LeR/TE-AD Estimator, H^1 Case 3, $N_X = N_Y = 32$ . . . 67
Figure 6.45 $\log_{10}\theta^{(i,j)}_{ang.}$ for RW Estimator, H^1 Case 3, $N_X = N_Y = 32$ . . . 67
Figure 6.46 $\log_{10}\theta^{(i,j)}_{ang.}$ for DAZ Indicator, H^1 Case 3, $N_X = N_Y = 32$ . . . 67
Figure 6.47 $\log_{10}\theta^{(i,j)}_{ang.}$ Histogram for LeR/TE-AD Estimator, H^1 Case 3, $N_X = N_Y = 32$ . . . 68
Figure 6.48 $\log_{10}\theta^{(i,j)}_{ang.}$ Histogram for RW Estimator, H^1 Case 3, $N_X = N_Y = 32$ . . . 69
Figure 6.49 $\log_{10}\theta^{(i,j)}_{ang.}$ Histogram for DAZ Indicator, H^1 Case 3, $N_X = N_Y = 32$ . . . 69
Figure 6.50 $\log_{10}\theta^{(i,j)}_{ang.}$ for LeR/TE-AD Estimator, H^1 Case 3, $N_X = N_Y = 512$ . . . 70
Figure 6.51 $\log_{10}\theta^{(i,j)}_{ang.}$ for RW Estimator, H^1 Case 3, $N_X = N_Y = 512$ . . . 70
Figure 6.52 $\log_{10}\theta^{(i,j)}_{ang.}$ for DAZ Indicator, H^1 Case 3, $N_X = N_Y = 512$ . . . 70
Figure 6.53 $\log_{10}\theta^{(i,j)}_{ang.}$ Histogram for LeR/TE-AD Estimator, H^1 Case 3, $N_X = N_Y = 512$ . . . 71
Figure 6.54 $\log_{10}\theta^{(i,j)}_{ang.}$ Histogram for RW Estimator, H^1 Case 3, $N_X = N_Y = 512$ . . . 71
Figure 6.55 $\log_{10}\theta^{(i,j)}_{ang.}$ Histogram for DAZ Indicator, H^1 Case 3, $N_X = N_Y = 512$ . . . 72
Figure 6.56 Angular Error/Estimator L_2 Norm Convergence for H^1 Case 3 . . . 72

Figure 6.57 Angular Effectivity Convergence for H^1 Case 3 73
Figure 6.58 Scalar Error/Estimator L_2 Norm Convergence for H^1 Case 3 73
Figure 6.59 Scalar Effectivity Convergence for H^1 Case 3 74
Figure 6.60 Global Angular Effectivity vs. computation time 75
Figure 6.61 Fraction of cells with $\theta_{ang.}^{(i,j)} - 1 \geq 0$ vs. computation time 76
Figure 6.62 Fraction of cells within some bound vs. computation time 77
Figure 6.63 Standard deviation of $\log_{10}\theta_{ang.}^{(i,j)}$ vs. computation time 78
Figure 6.64 Global Angular Effectivity vs. σ_t, $c = 0.1$, $N_X = N_Y = 32$, H^1 78
Figure 6.65 Global Angular Effectivity vs. σ_t, $c = 0.1$, $N_X = N_Y = 512$, H^1 78
Figure 6.66 Global Angular Effectivity vs. σ_t, $c = 0.5$, $N_X = N_Y = 32$, H^1 79
Figure 6.67 Global Angular Effectivity vs. σ_t, $c = 0.5$, $N_X = N_Y = 512$, H^1 79
Figure 6.68 Global Angular Effectivity vs. σ_t, $c = 0.9$, $N_X = N_Y = 32$, H^1 79
Figure 6.69 Global Angular Effectivity vs. σ_t, $c = 0.9$, $N_X = N_Y = 512$, H^1 79
Figure 6.70 Fraction of cells with $\theta_{ang.}^{(i,j)} - 1 \geq 0$ vs. σ_t, $c = 0.1$, $N_X = N_Y = 32$, H^1 80
Figure 6.71 Fraction of cells with $\theta_{ang.}^{(i,j)} - 1 \geq 0$ vs. σ_t, $c = 0.1$, $N_X = N_Y = 512$, H^1 80
Figure 6.72 Fraction of cells with $\theta_{ang.}^{(i,j)} - 1 \geq 0$ vs. σ_t, $c = 0.5$, $N_X = N_Y = 32$, H^1 80
Figure 6.73 Fraction of cells with $\theta_{ang.}^{(i,j)} - 1 \geq 0$ vs. σ_t, $c = 0.5$, $N_X = N_Y = 512$, H^1 80
Figure 6.74 Fraction of cells with $\theta_{ang.}^{(i,j)} - 1 \geq 0$ vs. σ_t, $c = 0.9$, $N_X = N_Y = 32$, H^1 81
Figure 6.75 Fraction of cells with $\theta_{ang.}^{(i,j)} - 1 \geq 0$ vs. σ_t, $c = 0.9$, $N_X = N_Y = 512$, H^1 81
Figure 6.76 Fraction of cells with $|\theta_{ang.}^{(i,j)} - 1| \leq$ specified bounds vs. σ_t, $c = 0.1$, $N_X = N_Y = 32$, H^1 81
Figure 6.77 Fraction of cells with $|\theta_{ang.}^{(i,j)} - 1| \leq$ specified bounds vs. σ_t, $c = 0.1$, $N_X = N_Y = 512$, H^1 82
Figure 6.78 Fraction of cells with $|\theta_{ang.}^{(i,j)} - 1| \leq$ specified bounds vs. σ_t, $c = 0.5$, $N_X = N_Y = 32$, H^1 82
Figure 6.79 Fraction of cells with $|\theta_{ang.}^{(i,j)} - 1| \leq$ specified bounds vs. σ_t, $c = 0.5$, $N_X = N_Y = 512$, H^1 83
Figure 6.80 Fraction of cells with $|\theta_{ang.}^{(i,j)} - 1| \leq$ specified bounds vs. σ_t, $c = 0.9$, $N_X = N_Y = 32$, H^1 83
Figure 6.81 Fraction of cells with $|\theta_{ang.}^{(i,j)} - 1| \leq$ specified bounds vs. σ_t, $c = 0.9$, $N_X = N_Y = 512$, H^1 84
Figure 6.82 Standard deviation of $\log_{10}\theta_{ang.}^{(i,j)}$ vs. σ_t, $c = 0.1$, $N_X = N_Y = 32$, H^1 84
Figure 6.83 Standard deviation of $\log_{10}\theta_{ang.}^{(i,j)}$ vs. σ_t, $c = 0.1$, $N_X = N_Y = 512$, H^1 84
Figure 6.84 Standard deviation of $\log_{10}\theta_{ang.}^{(i,j)}$ vs. σ_t, $c = 0.5$, $N_X = N_Y = 32$, H^1 85
Figure 6.85 Standard deviation of $\log_{10}\theta_{ang.}^{(i,j)}$ vs. σ_t, $c = 0.5$, $N_X = N_Y = 512$, H^1 85
Figure 6.86 Standard deviation of $\log_{10}\theta_{ang.}^{(i,j)}$ vs. σ_t, $c = 0.9$, $N_X = N_Y = 32$, H^1 85
Figure 6.87 Standard deviation of $\log_{10}\theta_{ang.}^{(i,j)}$ vs. σ_t, $c = 0.9$, $N_X = N_Y = 512$, H^1 85
Figure 6.88 Computation time vs. σ_t, $c = 0.1$, $N_X = N_Y = 32$, H^1 86
Figure 6.89 Computation time vs. σ_t, $c = 0.1$, $N_X = N_Y = 512$, H^1 86

Figure 6.90 Computation time vs. σ_t, $c = 0.5$, $N_X = N_Y = 32$, H^1 86
Figure 6.91 Computation time vs. σ_t, $c = 0.5$, $N_X = N_Y = 512$, H^1 86
Figure 6.92 Computation time vs. σ_t, $c = 0.9$, $N_X = N_Y = 32$, H^1 87
Figure 6.93 Computation time vs. σ_t, $c = 0.9$, $N_X = N_Y = 512$, H^1 87

Figure 7.1 $\log_{10}\theta^{(i,j)}_{ang.}$ for LeR/TE-AD Estimator, H^0 Case 1, $N_X = N_Y = 32$ 89
Figure 7.2 $\log_{10}\theta^{(i,j)}_{ang.}$ for RW Estimator, H^0 Case 1, $N_X = N_Y = 32$ 89
Figure 7.3 $\log_{10}\theta^{(i,j)}_{ang.}$ for DAZ Indicator, H^0 Case 1, $N_X = N_Y = 32$ 89
Figure 7.4 $\log_{10}\theta^{(i,j)}_{ang.}$ Histogram for LeR/TE-AD Estimator, H^0 Case 1, $N_X = N_Y = 32$ 90
Figure 7.5 $\log_{10}\theta^{(i,j)}_{ang.}$ Histogram for RW Estimator, H^0 Case 1, $N_X = N_Y = 32$ . . . 90
Figure 7.6 $\log_{10}\theta^{(i,j)}_{ang.}$ Histogram for DAZ Indicator, H^0 Case 1, $N_X = N_Y = 32$ . . . 91
Figure 7.7 $\log_{10}\theta^{(i,j)}_{sca.}$ for LeR/TE-AD Estimator, H^0 Case 1, $N_X = N_Y = 32$ 91
Figure 7.8 $\log_{10}\theta^{(i,j)}_{sca.}$ for RW Estimator, H^0 Case 1, $N_X = N_Y = 32$ 91
Figure 7.9 $\log_{10}\theta^{(i,j)}_{sca.}$ Histogram for LeR/TE-AD Estimator, H^0 Case 1, $N_X = N_Y = 32$ 92
Figure 7.10 $\log_{10}\theta^{(i,j)}_{sca.}$ Histogram for RW Estimator, H^0 Case 1, $N_X = N_Y = 32$ . . . 92
Figure 7.11 $\log_{10}\theta^{(i,j)}_{ang.}$ for LeR/TE-AD Estimator, H^0 Case 1, $N_X = N_Y = 512$ . . . 93
Figure 7.12 $\log_{10}\theta^{(i,j)}_{ang.}$ for RW Estimator, H^0 Case 1, $N_X = N_Y = 512$ 93
Figure 7.13 $\log_{10}\theta^{(i,j)}_{ang.}$ for DAZ Indicator, H^0 Case 1, $N_X = N_Y = 512$ 93
Figure 7.14 $\log_{10}\theta^{(i,j)}_{ang.}$ Histogram for LeR/TE-AD Estimator, H^0 Case 1, $N_X = N_Y = 512$ 94
Figure 7.15 $\log_{10}\theta^{(i,j)}_{ang.}$ Histogram for RW Estimator, H^0 Case 1, $N_X = N_Y = 512$ . . 94
Figure 7.16 $\log_{10}\theta^{(i,j)}_{ang.}$ Histogram for DAZ Indicator, H^0 Case 1, $N_X = N_Y = 512$ . . 95
Figure 7.17 $\log_{10}\theta^{(i,j)}_{sca.}$ for LeR/TE-AD Estimator, H^0 Case 1, $N_X = N_Y = 512$ . . . 95
Figure 7.18 $\log_{10}\theta^{(i,j)}_{sca.}$ for RW Estimator, H^0 Case 1, $N_X = N_Y = 512$ 95
Figure 7.19 $\log_{10}\theta^{(i,j)}_{sca.}$ Histogram for LeR/TE-AD Estimator, H^0 Case 1, $N_X = N_Y = 512$ 96
Figure 7.20 $\log_{10}\theta^{(i,j)}_{sca.}$ Histogram for RW Estimator, H^0 Case 1, $N_X = N_Y = 512$ . . 96
Figure 7.21 Angular Error/Estimator L_2 Norm Convergence for H^0 Case 1 97
Figure 7.22 Angular Effectivity Convergence for H^0 Case 1 97
Figure 7.23 Scalar Error/Estimator L_2 Norm Convergence for H^0 Case 1 98
Figure 7.24 Scalar Effectivity Convergence for H^0 Case 1 98
Figure 7.25 Global Angular Effectivity vs. σ_t, $c = 0.1$, $N_X = N_Y = 32$, H^0 99
Figure 7.26 Global Angular Effectivity vs. σ_t, $c = 0.1$, $N_X = N_Y = 512$, H^0 99
Figure 7.27 Global Angular Effectivity vs. σ_t, $c = 0.5$, $N_X = N_Y = 32$, H^0 99
Figure 7.28 Global Angular Effectivity vs. σ_t, $c = 0.5$, $N_X = N_Y = 512$, H^0 99
Figure 7.29 Global Angular Effectivity vs. σ_t, $c = 0.9$, $N_X = N_Y = 32$, H^0 100
Figure 7.30 Global Angular Effectivity vs. σ_t, $c = 0.9$, $N_X = N_Y = 512$, H^0 100
Figure 7.31 Fraction of cells with $\theta^{(i,j)}_{ang.} - 1 \geq 0$ vs. σ_t, $c = 0.1$, $N_X = N_Y = 32$, H^0 . . 101

Figure 7.32 Fraction of cells with $\theta_{ang.}^{(i,j)} - 1 \geq 0$ vs. σ_t, $c = 0.1$, $N_X = N_Y = 512$, H^0 . 101
Figure 7.33 Fraction of cells with $\theta_{ang.}^{(i,j)} - 1 \geq 0$ vs. σ_t, $c = 0.5$, $N_X = N_Y = 32$, H^0 . . 101
Figure 7.34 Fraction of cells with $\theta_{ang.}^{(i,j)} - 1 \geq 0$ vs. σ_t, $c = 0.5$, $N_X = N_Y = 512$, H^0 . 101
Figure 7.35 Fraction of cells with $\theta_{ang.}^{(i,j)} - 1 \geq 0$ vs. σ_t, $c = 0.9$, $N_X = N_Y = 32$, H^0 . . 102
Figure 7.36 Fraction of cells with $\theta_{ang.}^{(i,j)} - 1 \geq 0$ vs. σ_t, $c = 0.9$, $N_X = N_Y = 512$, H^0 . 102
Figure 7.37 Fraction of cells with $|\theta_{ang.}^{(i,j)} - 1| \leq$ specified bounds vs. σ_t, $c = 0.1$, $N_X = N_Y = 32$, H^0 102
Figure 7.38 Fraction of cells with $|\theta_{ang.}^{(i,j)} - 1| \leq$ specified bounds vs. σ_t, $c = 0.1$, $N_X = N_Y = 512$, H^0 103
Figure 7.39 Fraction of cells with $|\theta_{ang.}^{(i,j)} - 1| \leq$ specified bounds vs. σ_t, $c = 0.5$, $N_X = N_Y = 32$, H^0 103
Figure 7.40 Fraction of cells with $|\theta_{ang.}^{(i,j)} - 1| \leq$ specified bounds vs. σ_t, $c = 0.5$, $N_X = N_Y = 512$, H^0 104
Figure 7.41 Fraction of cells with $|\theta_{ang.}^{(i,j)} - 1| \leq$ specified bounds vs. σ_t, $c = 0.9$, $N_X = N_Y = 32$, H^0 104
Figure 7.42 Fraction of cells with $|\theta_{ang.}^{(i,j)} - 1| \leq$ specified bounds vs. σ_t, $c = 0.9$, $N_X = N_Y = 512$, H^0 105
Figure 7.43 Standard deviation of $\log_{10} \theta_{ang.}^{(i,j)}$ vs. σ_t, $c = 0.1$, $N_X = N_Y = 32$, H^0 . . . 105
Figure 7.44 Standard deviation of $\log_{10} \theta_{ang.}^{(i,j)}$ vs. σ_t, $c = 0.1$, $N_X = N_Y = 512$, H^0 . . 105
Figure 7.45 Standard deviation of $\log_{10} \theta_{ang.}^{(i,j)}$ vs. σ_t, $c = 0.5$, $N_X = N_Y = 32$, H^0 . . . 105
Figure 7.46 Standard deviation of $\log_{10} \theta_{ang.}^{(i,j)}$ vs. σ_t, $c = 0.5$, $N_X = N_Y = 512$, H^0 . . 105
Figure 7.47 Standard deviation of $\log_{10} \theta_{ang.}^{(i,j)}$ vs. σ_t, $c = 0.9$, $N_X = N_Y = 32$, H^0 . . . 106
Figure 7.48 Standard deviation of $\log_{10} \theta_{ang.}^{(i,j)}$ vs. σ_t, $c = 0.9$, $N_X = N_Y = 512$, H^0 . . 106
Figure 7.49 Computation time vs. σ_t, $c = 0.1$, $N_X = N_Y = 32$, H^0 106
Figure 7.50 Computation time vs. σ_t, $c = 0.1$, $N_X = N_Y = 512$, H^0 106
Figure 7.51 Computation time vs. σ_t, $c = 0.5$, $N_X = N_Y = 32$, H^0 106
Figure 7.52 Computation time vs. σ_t, $c = 0.5$, $N_X = N_Y = 512$, H^0 106
Figure 7.53 Computation time vs. σ_t, $c = 0.9$, $N_X = N_Y = 32$, H^0 107
Figure 7.54 Computation time vs. σ_t, $c = 0.9$, $N_X = N_Y = 512$, H^0 107

Chapter 1

Background

1.1 *A Posteriori* Spatial Discretization Error Estimation

Several *a posteriori* error estimators have been developed for solving differential equations with the finite elements method. Generally these are developed with effective adaptive mesh refinement (AMR) as the main purpose. This review is intended to summarize the findings that led to or prompted further study of this topic in this work.

Madsen derived an *a posteriori* error bound for numerical approximations to the steady-state, one-speed transport equation in rectangular geometry for the L_2 and L_1 norms, provided the absorption cross-section is bounded below away from zero [1]. This estimator uses linearity to apply the transport operator to the error function, thereby extending a bound on the true solution to a bound on the error. The resulting error estimator process requires a "smoothing" of the numerical solution, which Madsen assumes to be a point-wise discretization. This global bound was demonstrated to decrease with mesh refinement in Madsen's original work, though no reference solutions were provided as an empirical validation. O'Brien later heuristically applied this global bound as a local indication of the solution error, confirming the global error bound and empirically demonstrating a local bound [2].

Babuška and Rheinboldt developed an *a posteriori* error estimate for one-dimensional model problems involving a linear, self-adjoint operator of the second order with Dirichlet boundary conditions that was later expanded to eigenvalue and parabolic problems [3]. This estimate provided global asymptotic upper and lower bounds on the error in the energy norm by deriving local indicators as a function of the residual (integrated by Gaussian quadrature). Similar asymptotic error estimates can be derived for other norms as well [3]. These estimators were seen to increase in efficiency (effectivity) as the mesh was refined. This process was later applied to adaptive mesh refinement with compelling results [4].

Gratsch and Bathe outlined several error estimators in the context of the global energy-norm for elliptic linear problems [5]. Some estimators were derived to bound the error globally while some were merely intended to accurately portray the error profile as indicators. They explored three types of estimators: 1) an explicit error estimator that bounds the global energy norm of the error from above by direct computation of interior element residuals and jumps at the element boundaries, 2) implicit error estimators that involve the solution of auxiliary boundary value problems using cell-wise or subdomain-wise residuals, and 3) a recovery-based error estimator, in which an "improved" approximation to the gradient is calculated, and the gradient from the FEM calculation is subtracted from it to estimate the error. While many of the estimators were intended to bound, the authors acknowledge that upper and lower bounds on the error are not useful if the difference between the two are too large, which is the case in their work. Additionally, they find that all error bounds analyzed are not actually guaranteed to bound the error in practice.

Ragusa and Wang have worked extensively on *h*-, *p*-, and *hp*-adaptivity in AMR for neutron transport. These adaptivity methods increase spatial accuracy of the discrete solution progressively by refining the spatial mesh, spatial discretization method order, and a combination of both, respectively. In one work, they implemented an *hp*-adaptivity scheme for multigroup diffusion that captured the advantages of both *h*- and *p*-adaptivity schemes, namely appropriate refinement in regions where the solution is not smooth and a higher convergence rate in regions where the solution is smooth, respectively [6]. As a result, this method was shown to converge regardless of the choice of initial mesh, which is not always true for *p*-adaptivity strategies, and to converge at a higher rate than a purely *h*-adaptivity strategy [6]. In neutron transport they have developed and implemented an *h*-adaptivity scheme utilizing a two-mesh difference-based error estimator in which a solution on a uniformly-refined mesh, integrated over angle as scalar flux or current, is effectively utilized as a reference solution for the coarse mesh solution [7]. This was inspired by [8] in which a full goal-oriented *hp*-adaptivity scheme was also proposed requiring refinement of the mesh *and* degree of polynomial approximation in finite elements to acquire a reference solution. The additional transport solve on the refined mesh required by Ragusa and Wang's estimator was preconditioned with a projection of the unrefined mesh solution onto the refined mesh to decrease computational cost. When applied to problems with a higher-order discontinuous-Galerkin finite element method discretization it proved to be an effective AMR driver.

Wang and Ragusa performed a comparative analysis of the AMR performance of three error quantities [9]: a difference-based variant of a two-mesh error estimate [7] (referred to in O'Brien and Azmy's work as "Ragusa-Wang" estimator [10]), a projection-based variant of a two-mesh error estimate, and a jump-based error indicator related to the interface residual in [11]. In their analysis, they find that the difference-based variant of a two-mesh error estimate is most accurate. Their analysis also included an examination of goal-oriented error estimates applied to AMR, in which the adjoint transport equation is solved given a quantity of interest (i.e., localized reaction rates) and used in conjunction with an *a posteriori* error estimate to give an importance-weighted error estimate. Goal-oriented AMR was found to outperform standard AMR when solution magnitudes were low in regions containing quantities of interest.

Fournier, *et al.* also analyzed a cell boundary jump-discontinuity-based estimator, similar to the one used by Wang and Ragusa [9], rooted in finite volume methods to drive AMR routines [12]. This estimator was shown to accurately portray the error distribution in the domain, even at singular characteristics, although a normalization factor was used. This was compared *vis-a-vis* the “Radau Estimator”, [13], which had trouble identifying the SC-intersected cells as high error cells.

O’Brien and Azmy performed a comparative analysis of the accuracy of three *a posteriori* error quantities [10]: the O’Brien residual source estimator [2], the Ragusa-Wang estimator [7], and jump-discontinuitiy indicator [12], though functionally similar to that presented in [9]. This analysis was further explored in O’Brien’s M.S. thesis [2] with the addition of the Madsen estimator [1] and a cell-centered two-mesh estimator. It was found that in terms of accuracy the Ragusa-Wang estimator was superior to all other estimators considered at the cost of a larger computation time. The Method of Manufactured Solutions (MMS) was used to generate reference solutions to the spatially continuous S_N transport equation. O’Brien also showed that the Madsen error estimator was impractically too large compared to the true error, bringing into question its use as anything but the most cautious bound.

1.2 Residual-Based Error Estimators

The use of the “residual” of the discretization in spatial error estimates is a well-established concept. In most works the “residual” is considered to be the “leftover term” that remains when the discrete solution is inserted into the continuous bilinear problem.

Bank and Weiser proposed three *a posteriori* global error estimators in the energy-norm for elliptic PDEs using finite element methods on triangular meshes. These estimators were based on solving local Neumann problems in each element [14], which requires solving the bilinear form for the discretization error using some residual as an input, though they distinguish between the element residual and the inter-element jump discontinuity in the gradient of the solution. The resulting estimators are derived to give upper and lower bounds on the global error. However, when numerical results were gathered on a test problem, only the third estimator derived was shown to converge to the true error norm with mesh refinement, bringing the utility of the other two estimators into question. Additionally, only the first estimator was actually shown to bound the global error from above for the cases examined.

Kuzmin and Korotov introduce a residual-based, goal-oriented error estimate for steady convection-diffusion equations [15]. This relates the error in a quantity of interest as a function of the upper bounds for the magnitudes of various weak form residuals. These residuals require knowledge of the discrete forward solution, the discrete adjoint solution, and the true continuous adjoint solution. This requires one to generate another (higher-order) approximation of the true adjoint solution, as the discrete adjoint solution cannot be used as an approximation in this context, lest the estimator return trivial results [15]. This estimator was tested for a one-dimensional convection-diffusion equation, and it was found to provide an excellent estimate for select test problems.

Segeth introduces the "explicit residual *a posteriori* error estimator" in the local energy-norm for linear second order elliptic PDEs discretized on regular triangular meshes. The estimator equation has three distinct parts: the first part relates the residual of the "strong" solution and the "boundary terms", the second expresses that the gradient of the discrete solution may have jump-discontinuities across boundary edges, and the third expresses that the discrete solution may not satisfy the boundary conditions exactly. This estimator provides a "two-sided" local estimate of the error and is useful in theory, but it requires calculation of constants that, in general, must be approximated [16]. This estimator has shown to asymptotically converge to the true error, but accurate error estimation relies on the calculation of constants that, by nature, are unknown.

Gratsch and Bathe also examined several residual-based estimators for elliptic ODEs [5]. The explicit error estimator uses the local L_2 norm of the residual in conjunction with jump discontinuities to place a cautious bound on the error. Because the explicit error estimators rely on unknown constants, an accurate representation of the error magnitude cannot be guaranteed. However, this makes them suitable for AMR, which places more emphasis on the relative magnitude of the local error estimate throughout the domain rather than the absolute magnitude. The implicit estimators use the residual and jump discontinuities as sources for element-wise or subdomain-wise problems, the solution of which is an error estimate. These estimators do not have unknown constants. The element-wise residual method has been shown to only bound the error from above if the local problem is computed exactly. The subdomain-wise residual method show good results in terms of effectivity indices on upper and lower bounds of the error, and the estimator is reliable on coarse meshes as well [17].

Duo, Azmy, and Zikatanov introduced and implemented a local *a posteriori* error indicator in [18] for AMR. Similar to O'Brien's heuristic application of Madsen's global bound as a local error indicator, this error indicator was heuristically derived from a global error estimator valid for problems with solutions in H^r, where $r \geq 1$, derived by Duo [19]. This global estimate was derived by using the Cauchy-Schwarz inequality to bound the global error norm from above by an expression that utilizes the norm of the estimated residual and inter-element jumps of varying polynomial order, similar to that in [5]. This required approximating a higher-order AHOT-N solution via a succession of local single sweep problems for each cell in the mesh. For two-dimensional Cartesian geometry, Duo introduced a shielding benchmark for AMR as well as a MMS-AHOT-N interface to provide true, continuous reference solutions for evaluating estimator performance [18, 19]. The resultant global estimator proved to bound the global error from above and converge with the same order as the error, but it was exceedingly cautious for problems of spatial order $\Lambda = 0$. It did not locally bound the error, but it was an effective AMR driver for the shielding benchmark.

Fournier, Le Tellier, and Suteau implemented an *a posteriori* error estimator for neutron transport in the context of AMR for DGFEM discretizations [20]. The estimator is based on a cell-by-cell Taylor series expansion of the true error inserted into the bilinear DGFEM transport operator, resulting in an error estimator dependent on Radau polynomials one order higher than that of the method [13]. The estimator also requires one to project the residual on a given polynomial factor to obtain solutions β_x and β_y essential to calculating the estimate. The estimator is valid for conforming meshes with uniform polynomial basis order, but they implement a modification for use on non-conforming meshes and varying polynomial basis order. They examined its accuracy relative to the true error on a non-scattering, zero fixed source problems, and they observed strong agreement in regions in which the true solution was infinitely differentiable but poor agreement near SCs.

Lathouwers introduces a goal-oriented spatial adaptivity scheme for S_N transport on unstructured triangulared meshes [21]. The *a posteriori* global error estimator used is derived to calculate the error in a computed response functional by summing up elemental error indicators. These local indicators are of a form similar to that in [18], except a bound is not applied to remove the practical dependence on the adjoint solution. As a result, the adjoint and forward solutions are used as inputs for the dual-weighted residuals that drive AMR. As the problems were refined, the global error estimator asymptotically reached perfect agreement with the true error in quantity of interest. Lathouwers points out that the adjoint solution could be made cheaper by reducing the order of the adjoint problem (i.e., reducing number of cells or computational order) with minimal loss in indicator effectiveness.

Jeffers, *et al.*, presented a goal-based h-adaptivity scheme for the 1-D diamond difference spatial discretization of the S_N transport equation [22]. This required establishing a quantity-of-interest (i.e., reaction rate, k_{eff}-eigenvalue) and using the adjoint solution computed in the same manner as the forward solution to generate local dual-weighted residuals (DWRs) for use as error indicators in an AMR process. Jeffers, *et al.* posit the possibility of using a higher-order adjoint solution as a weighting function, though this generally did not give better convergence to the AMR process. This estimator also tended to be locally cautious.

O'Brien introduced a residual-based, two-step estimator in which the residual, defined as the deviation from equality when the numerical solution is inserted into the spatially-continuous transport equation, is calculated *a posteriori*, integrated over angle, and used as an isotropic source in a fully-converged transport-like problem, where the discretized transport equation is used as an approximation of the spatially-continuous transport equation, to solve for the error estimate [2]. The additional computational cost of the required extra solution was deemed acceptable provided the estimator was competitive with Ragusa and Wang's mesh-based two-step estimator [7]. However, it was found that this estimator did not give reliable estimates of the true error, as the effectivity values were not centered at exact agreement, and the estimator accuracy did not get improve with higher order spatial discretization.

1.3 Estimators *vs.* Indicators *vs.* Bounds

The literature is oftentimes vague or conflicting when referring to error estimation quantities. Sometimes the explicit distinction of an error *bound* is made when referring to a quantity that provides an upper or lower bound on the error. However, it is also common for such quantities to be called *estimators.* A distinction is regularly made between *estimators* and *indicators*, quickly followed by a proverbial “throwing up hands” and relinquishing an attempt at consistent usage. An attempt here will be made to clarify terminology and reasoning for the purpose of precise interpretation of this work.

Traditionally in the finite elements method the terminology “error estimate” refers to a mathematically proven bound on the error norm derived via some error analysis [23]. This can relate the error to a convergence rate with respect to the true solution [24]. In this sense, Madsen’s global error bound is really an *estimator* [1], and Duo, Azmy, and Zikatanov’s distinction between the global error bound as an *estimator versus* the heuristically derived local *indicator* is correct [18]. However, strict adherence to this definition might suggest that error quantities that do not have mathematically proven bounds, such as Ragusa and Wang’s [7] and O’Brien’s [2] are not *estimators.*

Gratsch and Bathe define an “error estimate” as a “quantity that is an approximation to the actual unknown error” *versus* upper or lower bounds which are “quantities that are always larger, respectively, or smaller, respectively, than the actual unknown error” [5]. They further expand on the error estimate definition as providing “an estimate and ideally bounds for the solution error in a specified norm…” [5]. While not explicitly defining an “indicator”, Gratshe and Bathe do note that indicators are useful “[to] only obtain an indication of the error or to drive a mesh adaptivity scheme…” [5]. While Ragusa and Wang do not explicitly define the difference between an *estimator* and an *indicator*, they are careful to distinguish that the jump-based indicator is heuristic and not intended to provide a reliable estimate of the error [9]. However, they ultimately drop the distinction for simplicity’s sake. O’Brien makes an important distinction on the two observed definitions of “error estimate”. The first is that the estimator is a ”global error that is usually a totality, in some norm, of the indicators”, where indicators are ”the error associated with a particular element” [2]. The second is that the estimator is ”a more rigorous estimate of the error” and an indicator ”merely gives signs indicative of the size of the error” [2].

This work adopts a stance that such quantities fall into two categories: error *estimators* and error *indicators.* An estimator is a quantity that ideally provides an accurate representation of the magnitude of the error, whether that be the error itself or a reliable bound. This definition is consistent with the traditional FEM usage of “error estimate” to denote a mathematically proven bound *and* with Gratsch and Bathe’s definition of the estimate. This means that the terminology encompassing error *estimate* and error *bound* is not mutually exclusive, and the boundedness is merely considered a property of an estimator, such as in [18]. An indicator is a quantity that gives some indication of the behavior of the error, whether that be the magnitude, shape, or other quality, but cannot be reliably expected to quantify the error itself. This definition is consistent with Gratsch and Bathe and O'Brien as well as the usage of the term in the literature.

1.4 Motivation

This work attempts to introduce a practical new *a posteriori* spatial discretization error estimator for S_N neutron transport methods that borrows from concepts introduced in earlier works. Many of the estimators presented previously have proven to be computationally inexpensive but inaccurate or, conversely, accurate and precise but computationally costly. An estimator that has a sound mathematical basis (i.e., not developed heuristically) is introduced in this work and shown to be competitive *vis-a-vis* other established estimators in terms of accuracy and precision as well as being only moderately computationally burdensome. This estimator uses the residual in a process similar to O'Brien, and Bank and Weiser by using it as a source for the bilinear form of the DGFEM transport equation[2, 14]; although unlike in Bank and Weiser's work this problem is solved as a global problem rather than locally. Unlike O'Brien's, this residual is defined as the deviation from equality when the projected true solution is inserted into the discretized transport equation; we also retain the residual's anisotropy rather than condensing it into an isotropic quantity. This residual is approximated by using Taylor series expansions to provide the approximation of the true solution, and the higher-order derivatives are "reconstructed" *a posteriori* with the solutions from the DGFEM equation.

This work outlines the definition of the residual, derives the transport-like "residual source estimator", and demonstrates empirically the sound mathematical reasoning of the estimator using MMS. The process of approximating the residual *a posteriori* using a Taylor series expansion approximation of the true solution is also outlined. The behavior of this new estimator is observed for a variety of cases using true MMS-calculated solutions for reference. The residual source estimator is then compared against two estimators introduced by Ragusa and Wang and Duo, Azmy, and Zikatanov, in addition to an *en route* residual-based indicator.

Chapter 2

Introduction

2.1 The Neutron Transport Equation

All the methods, derivations, and results presented in this work are applied to the steady-state neutron transport equation in 2-D Cartesian coordinates with one-group treatment. Boundary conditions are restricted to fixed incoming angular flux.

Table 2.1 S_4 Level-Symmetric Quadrature/Octant

n	w_n	μ_n	η_n
1	0.08333	0.35002	0.35002
2	0.08333	0.35002	0.86889
3	0.08333	0.86889	0.35002

The method of angular discretization is the discrete ordinates (S_N) method, specifically S_4 with level symmetric quadrature, Table 2.1 [25], and scattering is restricted to isotropic scattering. All media are homogeneous and non-multiplying. Most of these restrictions are due to the limitations of our version of MMS, which will be covered later, and while extensions beyond these restrictions should be possible and even trivial in some cases, rederivation of the forthcoming residual source estimator would be required. The neutron transport equation as described is given by the following equations:

$$\vec{\Omega}_n \cdot \nabla\psi_n(x,y) + \sigma_t\psi_n(x,y) = \sigma_s \sum_{m=1}^{N} w_m\psi_m(x,y) + q(x,y),\ (x,y) \in \mathcal{D},\ n = 1,\ldots,N, \tag{2.1}$$

$$\psi_n(x,y) = \psi^{[BC]}(x,y),\ \hat{n}\cdot\vec{\Omega}_n < 0,\ (x,y) \in \partial\mathcal{D}, \tag{2.2}$$

where $\mathcal{D} \in [0,X] \times [0,Y]$ is the domain, $\partial\mathcal{D}$ is the domain boundary, and the scalar flux is defined as

$$\phi(x,y) \equiv \sum_{m=1}^{N} w_m \psi_m(x,y). \tag{2.3}$$

In 2-D Cartesian geometry, we represent the ordinate unit vector as $\vec{\Omega}_n = (\mu_n, \eta_n)$ and the gradient operator as the vector $\nabla = (\frac{\partial}{\partial x}, \frac{\partial}{\partial y})$. The total cross-section σ_t controls the optical thickness and is given as a unitless number. The scattering ratio c refers to the ratio of the scattering cross-section to the total cross-section σ_s/σ_t. For the purposes of this work, Eq. 2.1 and 2.2 are considered to be the "true" neutron transport equation, and any error calculated will be relative to the spatially continuous exact solution of that equation.

2.2 DGFEM-Λ

The neutron transport equation, even after the many levels of approximation from the previous section are applied, generally cannot be solved in its spatially continuous form. As a result, a spatial discretization method must be utilized to make the equation solvable. This work uses the Discontinuous Galerkin Finite Element Method of order Λ (DGFEM-Λ) because it has been used in previous related works and because it has some key advantages over other methods. One advantage is that it can be refined by increasing the order Λ. Another advantage is that it has the potential to capture discontinuities in the solution and its derivatives. Yet another advantage is the already strongly developed mathematical theory of FEM.

First, the notation of DGFEM must be established. The domain partitioned into a discrete mesh is represented by a set of cells, $K^{(i,j)} \in [x_{i-1}, x_i] \times [y_{j-1}, y_j]$, where $i = 1, ..., N_X$ and $j = 1, ..., N_Y$, and the boundary of a discrete cell is $\partial K^{(i,j)}$. Oftentimes the spatial variables are scaled such that the bounds of the cells are $[-1,1] \times [-1,1]$. This gives spatial variables $\tilde{x}_i = 2(x - x_{c,i})/\Delta x$ and $\tilde{y}_j = 2(y - y_{c,j})/\Delta y$, where $(x_{c,i}, y_{c,j})$ is the midpoint of cell $K^{(i,j)}$, and Δx and Δy are the dimensions of the cell in the x and y direction, respectively. Because DGFEM is a discontinuous method, the external and internal traces of the cell boundary or quantity are indicated by $+$ or $-$, respectively. In this work only uniform rectangular partitions are considered, and, in fact, all problem configurations considered in this work have $N_X = N_Y$. The mesh size is representative of the thickness of cells and is given by $h \equiv \max_{(i,j)}\{\Delta x_i, \Delta y_j\}$. The inner product in the x and y dimensions is given by Eq. 2.4 while the inner product in a single dimension x (or y) is given by Eq. 2.5 (or the analogous integral in y),

$$(f(x,y), g(x,y)) \equiv \int_{\Delta x_i} dx \int_{\Delta y_j} dy \; f(x,y)g(x,y), \tag{2.4}$$

$$\langle f(x), g(x) \rangle_x \equiv \int_{\Delta x_i} dx \; f(x,y)g(x,y). \tag{2.5}$$

Equation 2.1 is multiplied by some test function in a local test function space, $v(x,y) \in$

$V(K^{(i,j)})$, and integrated over the element $K^{(i,j)}$ to give,

$$\begin{aligned}\mu_n\left[\left\langle v^{(i,j)}(x_i^-,y),\psi_n^{(i,j)}(x_i^+,y)\right\rangle_y-\left\langle v^{(i,j)}(x_{i-1}^-,y),\psi_n^{(i,j)}(x_{i-1}^+,y)\right\rangle_y\right]&\\+\eta_n\left[\left\langle v^{(i,j)}(x,y_j^-),\psi_n^{(i,j)}(x,y_j^+)\right\rangle_x-\left\langle v^{(i,j)}(x,y_{j-1}^-),\psi_n^{(i,j)}(x,y_{j-1}^+)\right\rangle_x\right]&\\-\mu_n\left(\frac{\partial v^{(i,j)}}{\partial x},\psi_n^{(i,j)}(x,y)\right)-\eta_n\left(\frac{\partial v^{(i,j)}}{\partial y},\psi_n^{(i,j)}(x,y)\right)&\\+\left(v^{(i,j)},\sigma_t\psi_n^{(i,j)}(x,y)-\left(\sigma_s\phi(x,y)^{(i,j)}+q^{(i,j)}(x,y)\right)\right)&=0. \quad (2.6)\end{aligned}$$

The external trace of the flux on the outgoing edges is set equal to the internal trace of the flux on the outgoing edges, a process called "upstreaming"[26]. The test space for DGFEM-Λ is defined as

$$V(K^{(i,j)})=\left\{v_{g,h}(x,y)=P_g(\tilde{x}_i)P_h(\tilde{y}_j)\mid\forall g,h=0,...,\Lambda\right\}, \quad (2.7)$$

and the trial space, the finite representation of the solution, is given by

$$\psi_n(x,y)=\sum_{k=0}^{\Lambda}\sum_{l=0}^{\Lambda}\mathrm{sgn}(\mu_n)^k\mathrm{sgn}(\eta_n)^l(2k+1)(2l+1)P_k(\tilde{x}_i)P_l(\tilde{y}_j)\psi_{n,k,l}^{(i,j)}, \quad (2.8)$$

where $P_g(\tilde{x})$, *etc.*, are Legendre polynomials of order g. Legendre moments of the angular flux solution, $\psi_{k,l}^{(i,j)}$ are given by

$$\psi_{n,k,l}^{(i,j)}\equiv\frac{1}{\Delta x\Delta y}\left(P_k(\tilde{x}_i)P_l(\tilde{y}_j),\psi_n(x,y)\right). \quad (2.9)$$

Generally, Eq. 2.9 can be used to represent moments of any other quantity defined over the cell's volume, such as the fixed source. In this work the DGFEM equations are solved by the source iteration (SI) method with relative iterative tolerance of 10^{-10} or until the number of iterations is equal to 400.

2.3 Method of Manufactured Solutions

Since this work is focused on error estimation, it is imperative that reference solutions be accurate. Oftentimes reference solutions are computed via a highly refined solution; however, this work implements the Method of Manufactured Solutions (MMS), a method that allows for the calculation of true, continuous solutions to the transport equation [19]. The version of MMS used in this work finds solutions by setting the combined source, $Q(x,y)=\sigma_s\phi(x,y)+q(x,y)$, to a constant and solving for the angular flux via the Method of Characteristics (MoC), Eq. 2.10 [19]. Because the cross sections and combined source are uniform, the resultant angular flux equations can be solved analytically with no approximation in space.

$$\psi_n(x,y) = \begin{cases} \psi_n^{[N,S]}\left(x - \mathrm{sgn}(\mu_n)|\frac{\mu_n}{\eta_n}|\bar{y}\right) e^{-\frac{\sigma_t}{|\eta_n|}\bar{y}} + \frac{Q}{\sigma_t}(1 - e^{-\frac{\sigma_t}{|\eta_n|}\bar{y}}), \text{ for } \bar{y} < |\frac{\eta_n}{\mu_n}|\bar{x}, \\ \psi_n^{[W,E]}\left(y - \mathrm{sgn}(\eta_n)|\frac{\eta_n}{\mu_n}|\bar{x}\right) e^{-\frac{\sigma_t}{|\mu_n|}\bar{x}} + \frac{Q}{\sigma_t}(1 - e^{-\frac{\sigma_t}{|\mu_n|}\bar{x}}), \text{ for } \bar{y} > |\frac{\eta_n}{\mu_n}|\bar{x}, \end{cases} \tag{2.10}$$

where $\bar{x} = \frac{1-\mathrm{sgn}(\mu_n)}{2}X + \mathrm{sgn}(\mu_n)x$ and $\bar{y} = \frac{1-\mathrm{sgn}(\eta_n)}{2}Y + \mathrm{sgn}(\eta_n)y$. The fixed source $q(x,y)$ can be found by finding the scattering source that results from the MoC solution and subtracting it from the combined source [19],

$$q(x,y) = Q - \sigma_s\phi(x,y) = Q - \sigma_s\sum_{m=1}^{N} w_m\psi_m(x,y). \tag{2.11}$$

This fixed source as computed by Eq. 2.11, is used as an input to the discrete transport equation, the solution to which can be compared against the true MMS-derived solutions, Eq. 2.10. The value of the fixed source is set equal to σ_t to prevent negative flux and sources. In practice the true MMS solutions and fixed source are projected onto the same space as the discrete transport equation for easy storage and direct comparison.

The discontinuities inherent to problem boundary conditions will affect the regularity of the solution along the singular characteristics (SCs)[19], lines across which the solution is discontinuous in the same derivative as the BCs. In 3-D geometry, the irregularities appear as a plane emanating from a discontinuity rather than lines [27], and in 1-D this feature does not exist. In the problems presented in this work, the north and south boundary conditions will be reflections of each other, and the east and west boundaries will be likewise. No discontinuities will occur on a midpoint of the boundary, i.e., the only discontinuities in the boundary conditions will exist at the corners. This means that one SC per ordinate will emanate from each of the four corners of the problem with slope equal to η_n/μ_n, see Figure 2.1[2].

The true solution of the transport equation belongs in the Sobolev space,

$$\psi_n(x,y) \in H^r(\mathcal{D}) = \{\psi_n(x,y), D^\alpha\psi_n \in L_2(\mathcal{D}), |\alpha| \leq r\}, n = 1, \ldots, N, \tag{2.12}$$

where r corresponds to the lowest derivative $D^r\psi_n(x,y)$, in multi-index notation [23], that is regular. In problems presented in this work, the space the solution belongs to depends on BCs, and henceforth, a problem where the solution belongs to $H^r(\mathcal{D})$ will be described as an "H^r" problem. It has been shown that arbitrarily high degrees of solution regularity can be achieved with MMS by modifying the boundary conditions, including infinitely regular [27]. However, because it is impossible to introduce conditions in a real life problem that would elicit degrees of regularity higher than $r = 1$, only H^0 and H^1 problems are considered in this work.

The boundary conditions that yield these parameters are shown in Table 2.2. The function $F(Q, \sigma_s)$ is a simple function that ensures that Eq. 2.11 does not go negative at any point in

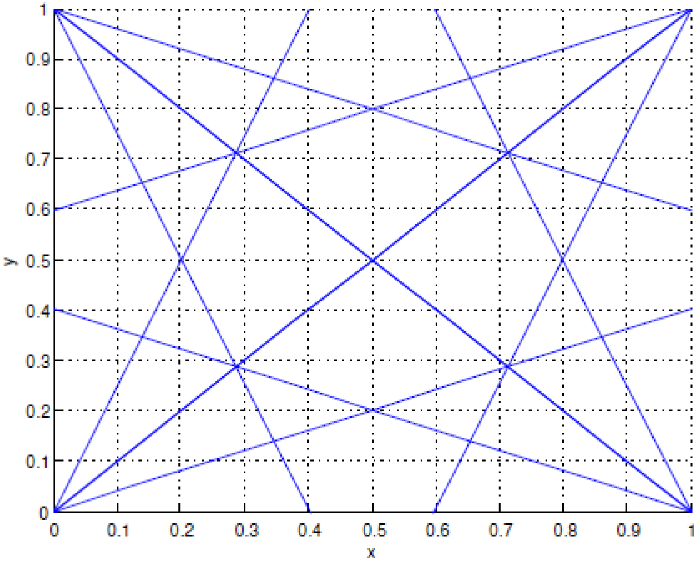

Figure 2.1 SCs for Level Symmetric S_4 Quadrature

	$\psi^{[N,S]}$	$\psi^{[W,E]}$
H^0	0	$F(Q,\sigma_s)$
H^1	0	0

Table 2.2 MMS Boundary Conditions

the domain, thereby introducing a non-physical solution to the problem [2]. It is given as

$$F(Q,\sigma_s) = \frac{Q-\sigma_s}{\sigma_s}.$$

Recall that $Q = \sigma_t$. Note that the source and boundary condition's dependence on the total and scattering cross sections means that changes to these parameters cannot be done without changing the resulting fixed source of the MMS problem.

2.4 Discretization Error

The spatial discretization error is the difference between the solution to the discretized transport equation and the true solution to the S_N transport equation projected onto the discrete mesh. Mathematically this is defined as

$$\varepsilon_h^\Lambda \equiv \psi_h^\Lambda - \left[\Pi_h^\Lambda \psi\right], \tag{2.13}$$

where Π_h^Λ indicates projection onto the mesh with size h and onto the DGFEM-Λ space, and ψ_h^Λ is the numerical solution to the discretized DGFEM-Λ S_N transport equation on the mesh with size h. Note that the discretization error is a local, cell-wise polynomial and is unique for each mesh size and DGFEM-Λ solution space.

Traditionally, due to the memory requirements of storing the angular quantities in addition to the practical focus on the scalar flux in transport problems, transport solutions and derivative quantities (i.e., reaction rates, leakage rates, *etc.*) are presented as scalar quantities. To remain consistent with this practice, as well as to remove intra-cell spatial dependencies of the reported local error, the error is presented in two local norms: the "angular" L_2 and "scalar" L_2 norms. The "angular" L_2 norm is simply the norm of the angular flux error,

$$\begin{aligned} E^{(i,j)}_{ang.} &= \sqrt{\sum_{n=1}^{N} w_n \int_{\Delta x_i} dx \int_{\Delta y_j} dy \; \varepsilon_n^2(x,y)} \\ &= \sqrt{\sum_{n=1}^{N} w_n \int_{\Delta x_i} dx \int_{\Delta y_j} dy \; \left(\psi^{\Lambda}_{h,n}(x,y) - \left[\Pi^{\Lambda}_{h}\psi_n\right](x,y)\right)^2}. \end{aligned} \tag{2.14}$$

We have found this to be a more accurate error norm. However, as mentioned previously, the angular solution to the transport equation is often not reported by transport codes, and previous works have traditionally defined "error" as the scalar flux error. Therefore, the "scalar" L_2 norm is presented as a measure consistent with this quantity,

$$\begin{aligned} E^{(i,j)}_{sca.} &= \sqrt{\int_{\Delta x_i} dx \int_{\Delta y_j} dy \left(\sum_{n=1}^{N} w_n \varepsilon_n(x,y)\right)^2} \\ &= \sqrt{\int_{\Delta x_i} dx \int_{\Delta y_j} dy \left(\phi^{\Lambda}_{h}(x,y) - \left[\Pi^{\Lambda}_{h}\phi\right](x,y)\right)^2}. \end{aligned} \tag{2.15}$$

Calculating these norms in the global sense is relatively simple, and the global "angular" and "scalar" L_2 norms are given in Eqs. 2.16 & 2.17, respectively,

$$E_{ang.} = \sqrt{\sum_{i=1}^{N_X} \sum_{j=1}^{N_Y} E^{(i,j)2}_{ang.}}, \tag{2.16}$$

$$E_{sca.} = \sqrt{\sum_{i=1}^{N_X} \sum_{j=1}^{N_Y} E^{(i,j)2}_{sca.}}, \tag{2.17}$$

When presented as norms of the error estimate, where the error estimate is given by 'ϵ', the norms given by Eqs. 2.14-2.17 will be represented with a lowercase 'e'. For brevity, error and error estimates formulated with an "angular" or "scalar" L_2 norm will be short-handed as angular or scalar estimates. Previous works ([3, 10, 12]) have presented the level of agreement between the true error and error estimate in terms of an "effectivity index", $\theta^{(i,j)}$, which, for either norm type, is the ratio of the estimated error norm to the true error norm,

$$\theta^{(i,j)}_{ang./sca.} = \left| \frac{e^{(i,j)}_{ang./sca.}}{E^{(i,j)}_{ang./sca.}} \right| . \tag{2.18}$$

The global effectivity index is merely the same expression as Eq. 2.18 with global norms in the ratio rather than local. It is advantageous to report the effectivity index on a $\log_{10}$-scale to emphasize the order of magnitude differences in both senses, overestimation and underestimation.

Chapter 3

Residual Source Estimator

3.1 Derivation of the Residual and Estimator

The residual in some form or another has been used to estimate the error in finite elements methods in many works, e.g., [3, 5, 18]. The "residual" as defined in this work is not necessarily identical to how it has been defined in other works. A broad definition of the residual is the deviation from the particle balance equation, Eq. 2.1, induced by applying a discretization to either the solution or the operator. More specifically, the definition of the residual in this work is the quantity that remains when the true solution to the continuous transport equation is projected onto the DGFEM-Λ space and operated on by the complete discretized DGFEM-Λ transport operator. To mathematically define this, the continuous transport operator and discretized transport operator are recast as Eqs. 3.1 and 3.2, respectively, where ordinate subscripts and explicit spatial dependencies are dropped for brevity and $\mathcal{S}$ represents the S_N scattering operator.

$$L\psi = \mathcal{S}\psi + q \tag{3.1}$$

$$L_h^\Lambda \psi_h^\Lambda = \mathcal{S}\psi_h^\Lambda + \Pi_h^\Lambda q \tag{3.2}$$

Projecting the true solution of Eq. 3.1 onto the h-mesh and the DGFEM-Λ space, and inserting the result into Eq. 3.2 gives the mathematical definition of the residual.

$$R_h^\Lambda \equiv \mathcal{S}\left[\Pi_h^\Lambda \psi\right] + \Pi_h^\Lambda q - L_h^\Lambda\left[\Pi_h^\Lambda \psi\right] \tag{3.3}$$

Note that the residual has h and Λ sub and superscripts, respectively, due to the fact that the residual as defined in this work exists on the discrete mesh in the DGFEM-Λ space. Also important to note is that the residual is an angular quantity and could be negative.

To derive an estimator based on the residual, the observation is made that $\Pi_h^\Lambda q$ appears in both Eqs. 3.2 and 3.3. This observation leads to

$$R_h^\Lambda = \mathcal{S}\left[\Pi_h^\Lambda \psi\right] + L_h^\Lambda \psi_h^\Lambda - \mathcal{S}\psi_h^\Lambda - L_h^\Lambda\left[\Pi_h^\Lambda \psi\right].$$

Because both the scattering operator and the discretized transport operator are linear, the difference between the discrete and continuous solutions can be equated to the spatial discretization error and elicit the relationship

$$R_h^\Lambda = -\mathcal{S}\varepsilon_h^\Lambda + L_h^\Lambda \varepsilon_h^\Lambda.$$

With some minor rearranging and a realization that the boundary conditions of the discrete problem are known quantities and, therefore, the true solution projected onto the mesh and DGFEM-Λ space, the transport-like Eqs. 3.4 and 3.5 for the spatial discretization error are found.

$$L_h^\Lambda \varepsilon_h^\Lambda = \mathcal{S}\varepsilon_h^\Lambda + R_h^\Lambda,\ (x,y) \in \mathcal{D},\ n = 1, \dots, N, \tag{3.4}$$

$$\varepsilon_n(x,y) = 0,\ \hat{n} \cdot \vec{\Omega}_n < 0,\ (x,y) \in \partial\mathcal{D}. \tag{3.5}$$

These equations can be solved analogously to the DGFEM-Λ equations with the same method used for converging the scattering source, i.e., source iterations. If one had knowledge of the true residual, the true spatial discretization error on mesh h could be computed exactly, with no error aside from machine precision and that incurred by finite iteration of the scattering source. However, knowledge of the true residual of course implies knowledge of the true solution and, therefore, the true error, reducing this to a trivial exercise of circular logic. Nevertheless, in the next section, the true residual will be used as a fixed source for a transport calculation in the manner described in an attempt to prove the validity of this idea.

Equations 3.4 and 3.5 are the footing of the residual source estimator (LeR). While most error estimators and indicators attempt to directly estimate the error in the solution, the residual source estimator is the process by which a residual approximation results in an error estimate. The significance of this difference will be seen in Chapter 5.

3.2 Empirical Proof of Validity

A few test problems are selected to show that the residual source estimator using the residual calculated via MMS as an input (LeR/MMS) will result in the true error, thus empirically proving the principle underlying the residual source estimator approach. The features of the true residual and true error will also be observed. The first problem is an H^1 problem with $\sigma_t = 1.0$, $c = 0.9$, and $N_X = N_Y = 32$.

When plotting a histogram of the local effectivity index for the angular and scalar estimators in $\log_{10}$-scale, one would expect to see a straight vertical line at $\log_{10} \theta^{(i,j)}_{ang./sca.} = 0$ if the error from the residual source estimator is identical to the true, directly-calculated error. Figures 3.1 and 3.2 exhibit this with some minor deviation due to iterative or round-off error. With confidence that the residual source estimator with the MMS-calculated residual returns the true error, the MMS-calculated residual can be taken to be the true residual, and the proposed process of the residual source estimator taken to be of sound logic.

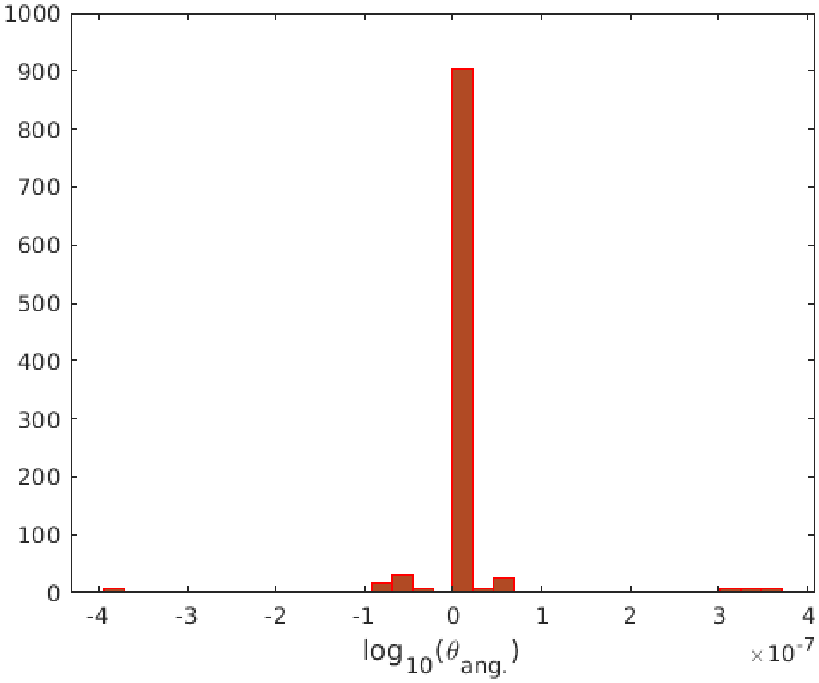

Figure 3.1 $\log_{10}\theta^{(i,j)}_{ang.}$ Histogram for LeR/MMS

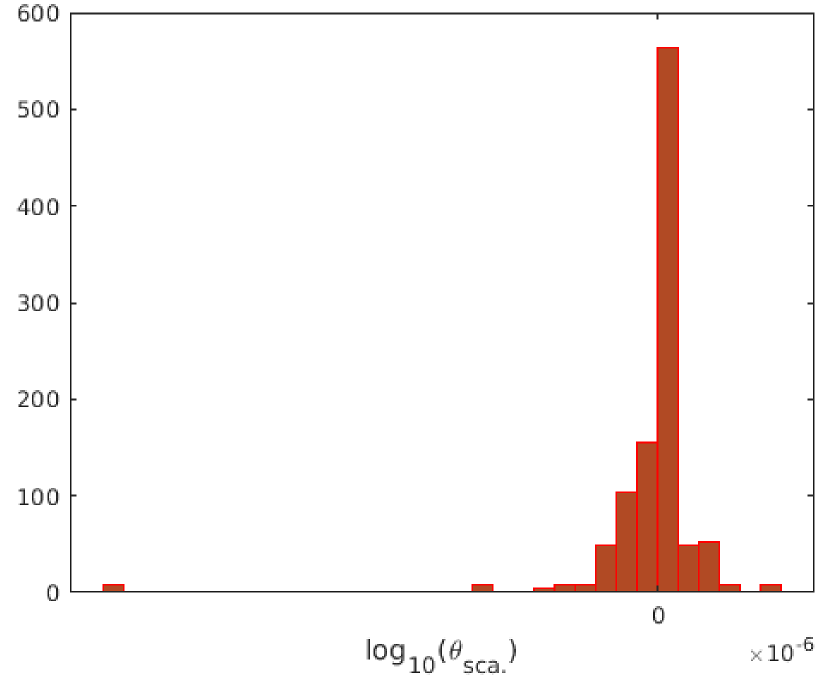

Figure 3.2 $\log_{10}\theta^{(i,j)}_{sca.}$ Histogram for LeR/MMS

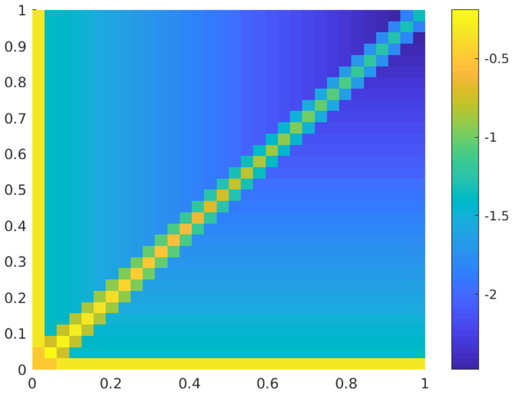

Figure 3.3 $\log_{10}|R_h^0(x,y)|$ in Quadrant 1, $\mu_n = \eta_n = 0.35002$, $N_X = N_Y = 32$

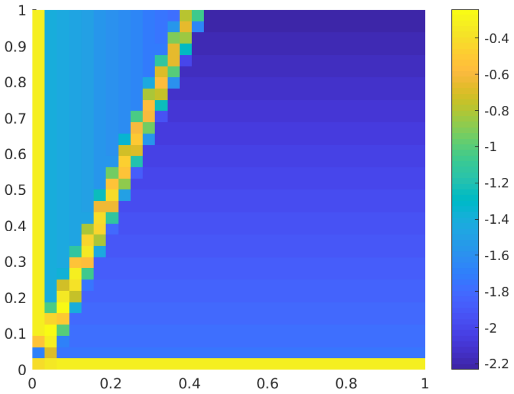

Figure 3.4 $\log_{10}|R_h^0(x,y)|$ in Quadrant 1, $\mu_n = 0.35002$, $\eta_n = 0.86889$, $N_X = N_Y = 32$

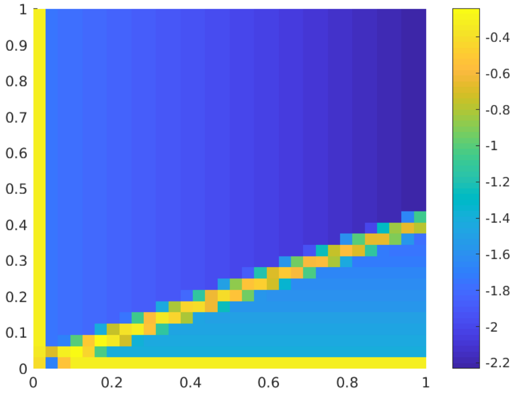

Figure 3.5 $\log_{10}|R_h^0(x,y)|$ in Quadrant 1, $\mu_n = 0.86889$, $\eta_n = 0.35002$, $N_X = N_Y = 32$

Key observations can be made by examining the true residual for the ordinates in Quadrant 1 where $\mu_n > 0$ and $\eta_n > 0$, Figures 3.3-3.5. The residual exists in the same space as the fixed source and angular flux; therefore, it can be easily plotted, as in DGFEM-0 it is represented as a piecewise constant value for each ordinate. The SC that extends from the problem's origin is the most noticeable feature, and this results in a larger residual due to the discontinuity in the true solution's derivative. Figure 3.3 shows that cells that border cells intersected by the SC also exhibit larger residual values. This is because, recalling Eq. 3.2, the DGFEM operator requires integrating the solution in the neighboring upwind cells, which may be discontinuous. Another key feature is a large residual on the inflow boundaries. This is because only the point-wise angular flux is defined at the boundary. Away from these two features, the residual is small and decreases with distance from the inflow boundary. This is because the solution is flatter and is captured better by a DGFEM-0 approximation.

The local angular L_2 and local scalar L_2 norms of the solution error in this example are

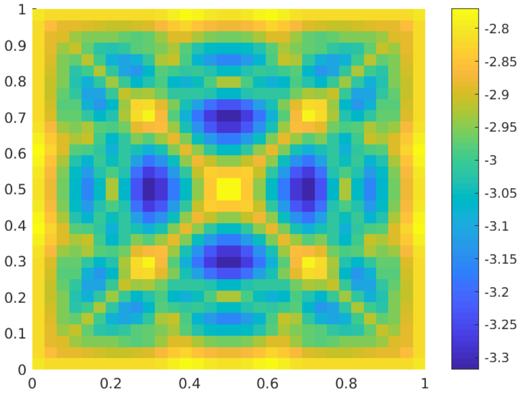

Figure 3.6 Local $\log_{10}$-Angular L_2 Norm of Solution Error, $N_X = N_Y = 32$

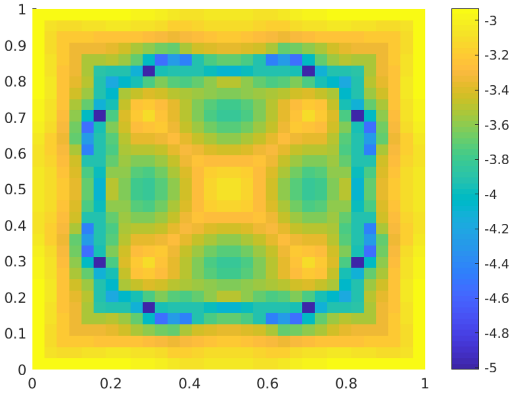

Figure 3.7 Local $\log_{10}$-Scalar L_2 Norm of Solution Error, $N_X = N_Y = 32$

shown in Figures 3.6 and 3.7, respectively. The two key features evident in these plots are the increased error along the SC's and the increased error close to the boundaries due to larger gradients resulting in poorer representation by a DGFEM-0 approximation. The next problem configuration considered is identical except for being more refined, $N_X = N_Y = 512$.

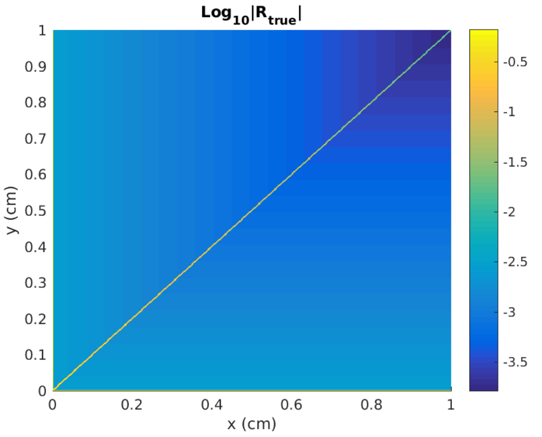

Figure 3.8 $\log_{10}|R_h^0(x,y)|$ in Quadrant 1, $\mu_n = \eta_n = 0.35002$, $N_X = N_Y = 512$

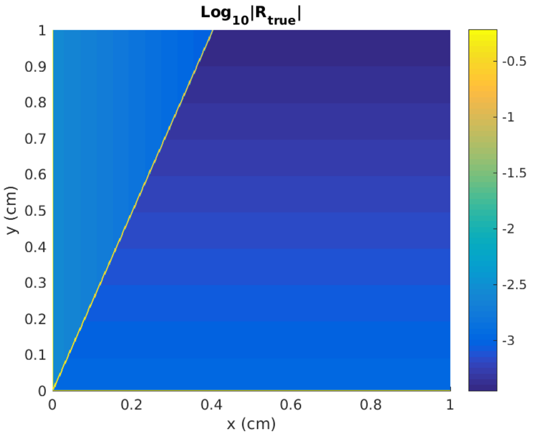

Figure 3.9 $\log_{10}|R_h^0(x,y)|$ in Quadrant 1, $\mu_n = 0.35002$, $\eta_n = 0.86889$, $N_X = N_Y = 512$

Figures 3.8-3.10 for the refined mesh problem show that the true residual in cells unaffected by SCs or boundaries seems to decrease with decreasing mesh size, but the residual converges to a constant with decreasing mesh size otherwise. While hard to see with this resolution, there still exists a strip of larger residual values along the inflow boundary.

The associated local angular L_2 and local scalar L_2 norms of the solution error are shown in Figures 3.11 and 3.12, respectively. These plots show both local error norm convergence with

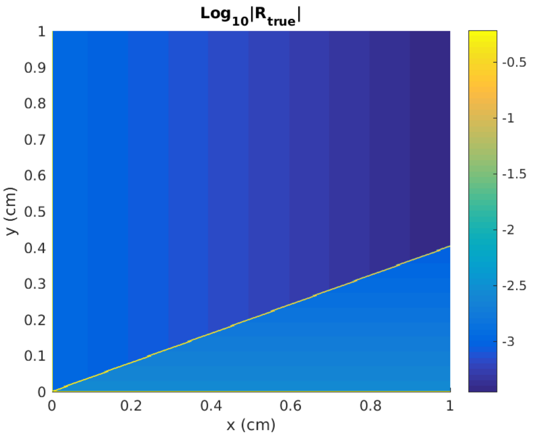

Figure 3.10 $\log_{10}|R_h^0(x,y)|$ in Quadrant 1, $\mu_n = 0.86889$, $\eta_n = 0.35002$, $N_X = N_Y = 512$

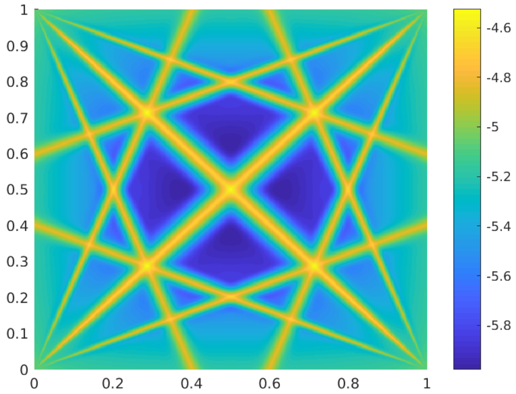

Figure 3.11 Local $\log_{10}$-Angular L_2 Norm of Solution Error, $N_X = N_Y = 512$

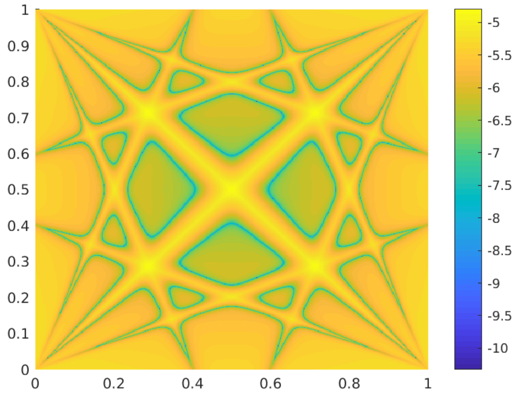

Figure 3.12 Local $\log_{10}$-Scalar L_2 Norm of Solution Error, $N_X = N_Y = 512$

decreasing mesh size and the increasing prominence of the SC's relative to other features as the mesh is refined.

3.3 Observed Convergence of Residual and Error

It is valuable to examine the local convergence of the residual in an H^1 problem with decreasing mesh size to confirm the assertions made in the previous subsection.

The local L_∞ spatial norm for a cell in the domain is plotted with decreasing mesh size in Figure 3.13 and shown to converge with $\mathcal{O}(h)$ as mesh size is decreased.

The local L_∞ spatial norms for cells on the boundary and SC intersected areas, plotted in Figures 3.14 and 3.15, respectively, show convergence to a constant with $\mathcal{O}(h)$. Because in the DGFEM-0 space the residual is represented by a piecewise constant function in space, the convergence of the local L_∞ norm in space also represents the pointwise convergence. We

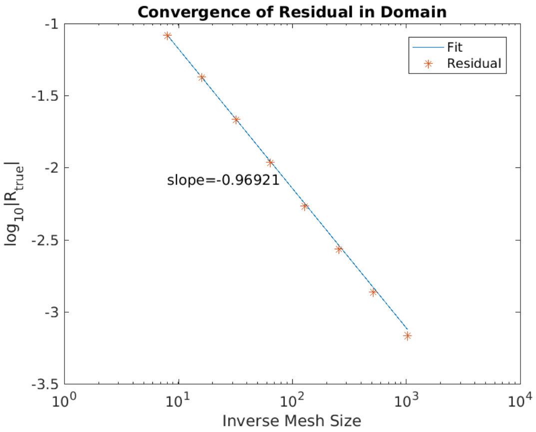

Figure 3.13 Local L_∞ spatial norm residual convergence in domain

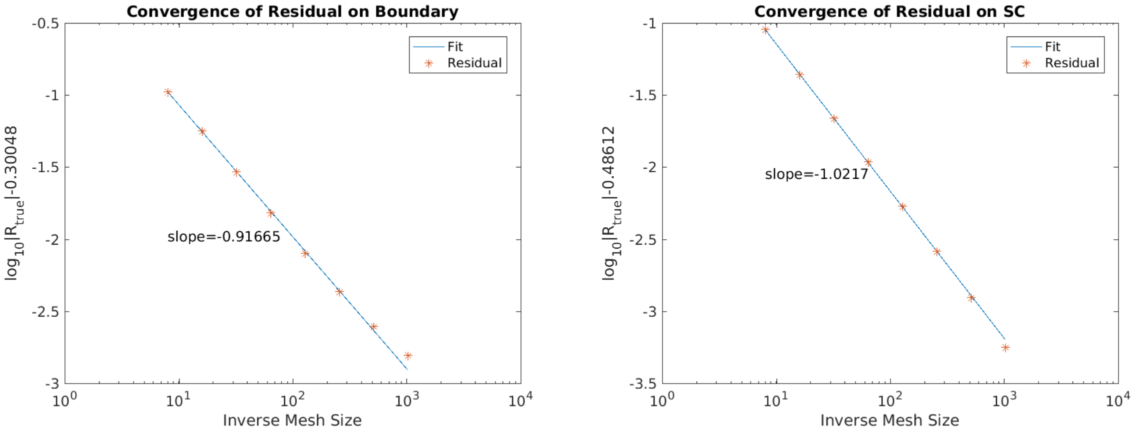

Figure 3.14 Local L_∞ spatial norm residual convergence on boundary

Figure 3.15 Local L_∞ spatial norm residual convergence on SC-influenced cell

can therefore say that the convergence in the local L_2 norm is going to be bounded above by the convergence in the local L_2 spatial norm, which will be $\mathcal{O}(h)$, $\mathcal{O}(1)$, and $\mathcal{O}(1)$ for the domain (sans boundary-neighboring and SC-influenced cells), incoming boundary layer, and SC-influenced cells, respectively.

The global convergence in both L_2 norms (angular and scalar) of the error and residual are shown in Figures 3.16 and 3.17, respectively. The residual converges with approximate $\mathcal{O}(h^{\frac{1}{2}})$, and the error converges with an error that approaches $\mathcal{O}(h)$ (angular error convergence order closer to $\mathcal{O}(h^{0.8})$ for this problem), as expected from theory [24]. Observing the local convergence of the residual allows us to estimate and confirm the global convergence of the residual. In a given ordinate the number of cells on the incoming boundary will be $N_X + N_Y - 1$. The number of cells affected by a SC and not also on an incoming boundary will linearly scale with the number of cells. For example, in a square domain with $N_X = N_Y$, given an ordinate where $\mu_n = \eta_n$, the number of cells affected by a SC and not also on an incoming boundary is

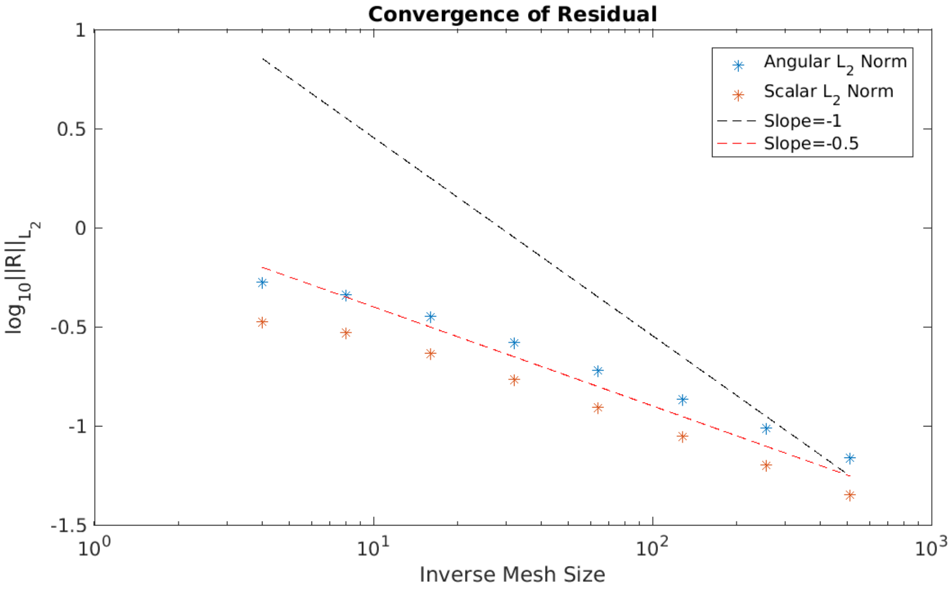

Figure 3.16 Global L_2 norm residual convergence

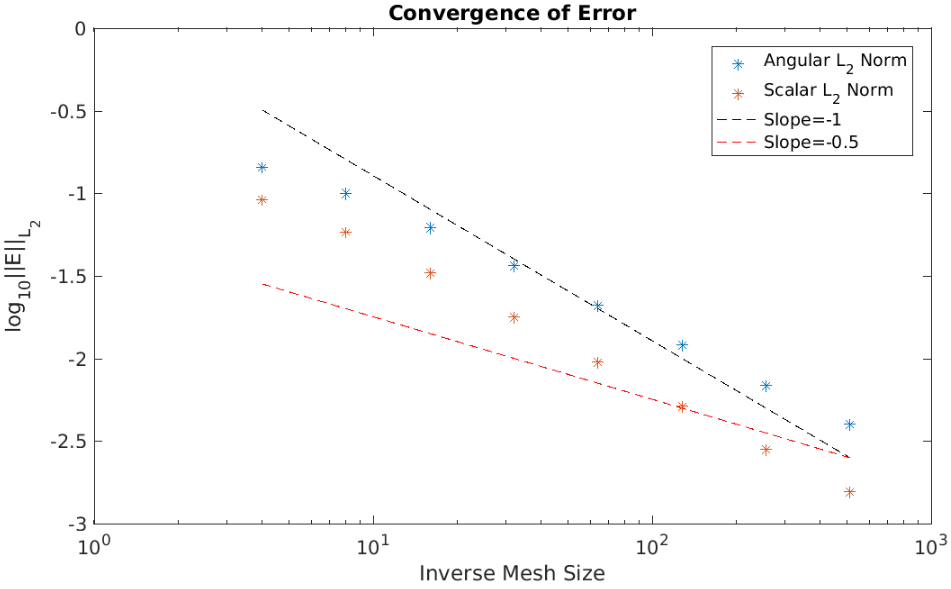

Figure 3.17 Global L_2 norm error convergence

$(N_X - 1) + (N_X - 2) + (N_Y - 2) = 3N_X - 5$.

Therefore, as $h \to 0$, it can be approximated that the number of cells on the boundary is proportional to $\frac{1}{h}$ and the number of cells on the SC and not also on the boundary is also proportional to $\frac{1}{h}$. For small h the number of cells not on the boundary or the SC is proportional to $\frac{1}{h^2}$. It is known from observing the local convergence of the residual that cells that are on the boundary or the SC converge with $\mathcal{O}(h)$ in the local L_2 norm, whereas the cells that do not fall on these points converge with $\mathcal{O}(h^2)$. The global convergence of the residual can then be calculated:

$$\begin{aligned}\|R\|^2_{ang.} &= \sum_{i=1}^{N_X}\sum_{j=1}^{N_Y} \|R\|^{(i,j)2}_{ang.} \\ &\leq \sum_{(i,j)\in BC\cup SC} \|R\|^{(i,j)2}_{ang.} + \sum_{(i,j)\notin BC\cup SC} \|R\|^{(i,j)2}_{ang.}.\end{aligned}$$

If it is assumed that h is sufficiently small, then to a first-order approximation the equivalency holds,

$$\begin{aligned}\|R\|^2_{ang.} &\leq \sum_{(i,j)\in BC\cup SC} h^2 C^{(i,j)2} + \sum_{(i,j)\notin BC\cup SC} h^4 C^{(i,j)2} \\ &\leq \max_{(i,j)}\left\{C^{(i,j)2}\right\}\left[\sum_{(i,j)\in BC\cup SC} h^2 + \sum_{(i,j)\notin BC\cup SC} h^4\right] \\ &\leq \max_{(i,j)}\left\{C^{(i,j)2}\right\}\left[\nu h + \xi h^2\right],\end{aligned}$$

where ν and ξ are generic proportionality constants. This gives the equivalency,

$$\|R\|^2_{ang.} \leq \max_{(i,j)}\left\{C^{(i,j)2}\right\} \max\{\nu,\xi\}\left[h + h^2\right],$$

and because $h << 1$, the following bound is found,

$$\|R\|_{ang.} \leq \Gamma h^{\frac{1}{2}},$$

where $\Gamma = \sqrt{2\max_{(i,j)}\left\{C^{(i,j)2}\right\}\max\{\nu,\xi\}}$.

The scalar L_2 norm can be shown to have the same bound in an analogous manner. This shows that, even though the error theoretically converges with $\mathcal{O}(h)$ for an H^1 problem, the residual in the same space as the distributed source will properly converge with $\mathcal{O}(h^{\frac{1}{2}})$. In Section 4.1.1 truncated equations for the residual will be found that confirm the empirically observed local convergence this analysis is based on. For H^0 problems we have observed the local pointwise convergence of the residual to be $\mathcal{O}(h^{-1})$ on cells that border SC-intersected cells, meaning the local residual *increases* with mesh refinement. If a similar process to the one shown in this section is done, the global residual can be shown to increase with $\mathcal{O}(h^{\frac{-1}{2}})$ in the L_2 norm for H^0 problems. Because having a residual convergence order that is different than the error convergence order, let alone increasing with mesh refinement, seems counter-intuitive, it is important to stress that the "residual" as defined in this work is not necessarily the "residual" that would bound the convergence of the numerical solution.

Chapter 4

Approximating the Residual

The residual source estimator in its approximate form is the solution to the equation

$$L_h^\Lambda \epsilon_h^\Lambda = \mathcal{S}\epsilon_h^\Lambda + \mathcal{R}_h^\Lambda, \tag{4.1}$$

where $\mathcal{R}_h^\Lambda$ is the approximated residual and ϵ_h^Λ is the error estimate. When approximating the residual, it is necessary to go outside the space of the solution to try and recapture some of the missing components of the true solution that have been truncated by the discretization method [5, 19]. As a result, all residual approximations strive to capture higher order derivatives or moments.

The primary approximation method of the residual introduced in this work is based on a Taylor Expansion. The process for deriving an *a posteriori* estimator will be to approximate the true solution with a Taylor Expansion about a cell corner, use this expression to approximate moments, use these moments to find direct approximate expressions for the residual, and, finally, use DGFEM-0 solutions to approximate the derivatives appearing in the residual expressions.

4.1 Taylor Expansion Approximation

4.1.1 Derivation

The first step in deriving the residual approximation is to approximate the true solution with a Taylor Expansion. Given a cell $K^{(i,j)}$ and direction $\vec{\Omega}_n$, the cell "origin", (x_i, y_j), is that cell's upwind corner. Dropping direction subscripts for brevity, the Taylor Expansion representation of the true solution is given as

$$\begin{aligned}\psi_{TE}^{(i,j)}(x,y) = \psi(x_i,y_j) + \delta_x\psi_x(x_i,y_j) + \delta_y\psi_y(x_i,y_j) \\ + \frac{\delta_x^2}{2}\psi_{xx}(x_i,y_j) + \delta_x\delta_y\psi_{xy}(x_i,y_j) + \frac{\delta_y^2}{2}\psi_{yy}(x_i,y_j) + \ldots + \mathcal{O}(\delta^\beta),\end{aligned} \tag{4.2}$$

where $\delta_x = (x - x_i)$, $\delta_y = (y - y_j)$, and the truncation order β is chosen to appropriately capture the necessary order of accuracy for the applicable method order. For DGFEM-0, it will be seen that order $\beta = 3$ is sufficient. Here it is important to note that this expression does not hold along singular characteristics, as the solution or derivatives are undefined on the discontinuities, depending on the order of the true solution's regularity.

Next, the necessary moments for solving the DGFEM-0 equations must be derived from the Taylor Expansion. The zeroth moment in cell $K^{(i,j)}$ is found by integrating Eq. 4.2 over the cell bounds, producing

$$\begin{aligned}\psi_{0,0}^{(i,j)} \approx \frac{\text{sgn}(\mu)\text{sgn}(\eta)}{\Delta x \Delta y} & \int_{x_i}^{x_i+\text{sgn}(\mu)\Delta x} dx \int_{y_j}^{y_j+\text{sgn}(\eta)\Delta y} dy \; \psi_{TE}^{(i,j)}(x,y) \\ &= \psi + \text{sgn}(\mu)\frac{\Delta x}{2}\psi_x + \text{sgn}(\eta)\frac{\Delta y}{2}\psi_y + \text{sgn}(\mu)\frac{\Delta x^2}{6}\psi_{xx} \\ &\quad + \text{sgn}(\mu)\text{sgn}(\eta)\frac{\Delta x \Delta y}{4}\psi_{xy} + \text{sgn}(\eta)\frac{\Delta y^2}{6}\psi_{yy}, \end{aligned} \tag{4.3}$$

where the (x_i, y_j) coordinates on the true angular flux value and derivatives that serve as Taylor Expansion coefficients are dropped for brevity. The moments in upwind cells $K^{(i-\text{sgn}(\mu_n),j)}$ and $K^{(i,j-\text{sgn}(\eta_n))}$ are likewise

$$\begin{aligned}\psi_{0,0}^{(i-\text{sgn}(\mu),j)} \approx \frac{\text{sgn}(\mu)\text{sgn}(\eta)}{\Delta x \Delta y} & \int_{x_i-\text{sgn}(\mu)\Delta x}^{x_i} dx \int_{y_j}^{y_j+\text{sgn}(\eta)\Delta y} dy \; \psi_{TE}^{(i,j)}(x,y) \\ &= \psi - \text{sgn}(\mu)\frac{\Delta x}{2}\psi_x + \text{sgn}(\eta)\frac{\Delta y}{2}\psi_y + \text{sgn}(\mu)\frac{\Delta x^2}{6}\psi_{xx} \\ &\quad - \text{sgn}(\mu)\text{sgn}(\eta)\frac{\Delta x \Delta y}{4}\psi_{xy} + \text{sgn}(\eta)\frac{\Delta y^2}{6}\psi_{yy}, \end{aligned} \tag{4.4}$$

and

$$\begin{aligned}\psi_{0,0}^{(i,j-\text{sgn}(\eta))} \approx \frac{\text{sgn}(\mu)\text{sgn}(\eta)}{\Delta x \Delta y} & \int_{x_i}^{x_i+\text{sgn}(\mu)\Delta x} dx \int_{y_j-\text{sgn}(\eta)\Delta y}^{y_j} dy \; \psi_{TE}^{(i,j)}(x,y) \\ &= \psi + \text{sgn}(\mu)\frac{\Delta x}{2}\psi_x - \text{sgn}(\eta)\frac{\Delta y}{2}\psi_y + \text{sgn}(\mu)\frac{\Delta x^2}{6}\psi_{xx} \\ &\quad - \text{sgn}(\mu)\text{sgn}(\eta)\frac{\Delta x \Delta y}{4}\psi_{xy} + \text{sgn}(\eta)\frac{\Delta y^2}{6}\psi_{yy}, \end{aligned} \tag{4.5}$$

respectively. Note that even though the integration is over different bounds, the point at which the Taylor Expansion is centered is still the "origin" of cell $K^{(i,j)}$. A similar treatment is applied to the scattering and fixed sources, and these moments are then inserted into the DGFEM-0 equations to find an approximate expression for the residual in cell $K^{(i,j)}$:

$$
\begin{aligned}
R_{0,0}^{(i,j)} = \sigma_s \phi_{0,0}^{(i,j)} + q_{0,0}^{(i,j)} - \sigma_t \psi_{0,0}^{(i,j)} \\
- \frac{|\mu|}{\Delta x} \left[\psi_{0,0}^{(i,j)} - \psi_{0,0}^{(i-\mathrm{sgn}(\mu),j)} \right] - \frac{|\eta|}{\Delta y} \left[\psi_{0,0}^{(i,j)} - \psi_{0,0}^{(i,j-\mathrm{sgn}(\eta))} \right].
\end{aligned}
$$

Plugging in Eqs. 4.3-4.5 to the above expression gives

$$
\begin{aligned}
R_{0,0}^{(i,j)} &= \sigma_s \left(\phi + \mathrm{sgn}(\mu) \frac{\Delta x}{2} \phi_x + \mathrm{sgn}(\eta) \frac{\Delta y}{2} \phi_y \right) \\
&+ \left(q + \mathrm{sgn}(\mu) \frac{\Delta x}{2} q_x + \mathrm{sgn}(\eta) \frac{\Delta y}{2} q_y \right) - \sigma_t \left(\psi + \mathrm{sgn}(\mu) \frac{\Delta x}{2} \psi_x + \mathrm{sgn}(\eta) \frac{\Delta y}{2} \psi_y \right) \\
&- \frac{|\mu|}{\Delta x} \left[\mathrm{sgn}(\mu) \Delta x \psi_x + \mathrm{sgn}(\mu) \mathrm{sgn}(\eta) \frac{\Delta x \Delta y}{2} \psi_{xy} \right] \\
&- \frac{|\eta|}{\Delta y} \left[\mathrm{sgn}(\eta) \Delta y \psi_y + \mathrm{sgn}(\mu) \mathrm{sgn}(\eta) \frac{\Delta x \Delta y}{2} \psi_{xy} \right] + \mathcal{O}(h^2).
\end{aligned}
$$

$\mathcal{O}(h^2)$ accuracy is considered sufficient for two reasons: the empirically observed residuals of cells not influenced by SCs or on the incoming boundary layer exhibit $\mathcal{O}(h)$ convergence in the local L_∞ norm, and the global error theoretically converges to zero with $\mathcal{O}(h)$ accuracy [24]. Essentially, it is not expected to obtain better residual convergence than the DGFEM-0 solution, especially since the residual will eventually be calculated with DGFEM-0 quantities. The expression is not accurate when intersected by a SC or directly downwind of a cell intersected by a SC in an H^0 or H^1 problem, however, because discontinuities in the solution and its first-order derivative will reduce the order of accuracy of the Taylor Expansion approximation of the solution. Terms are grouped to give the residual approximation

$$
\begin{aligned}
\mathcal{R}_{0,0}^{(i,j)} &= - \left\{ \sigma_t \psi + \mu \psi_x + \eta \psi_y - \sigma_s \phi - q \right\} \\
&+ \mathrm{sgn}(\mu) \frac{\Delta x}{2} \left(\sigma_s \phi_x + q_x - \sigma_t \psi_x - \mathrm{sgn}(\eta) |\eta| \psi_{xy} \right) \\
&+ \mathrm{sgn}(\eta) \frac{\Delta y}{2} \left(\sigma_s \phi_y + q_y - \sigma_t \psi_y - \mathrm{sgn}(\mu) |\mu| \psi_{xy} \right).
\end{aligned}
$$

The first term in the above equation is equal to zero per Eq. 2.1, giving the residual approximation for cell $K^{(i,j)}$

$$
\begin{aligned}
\mathcal{R}_{0,0}^{(i,j)} &= \mathrm{sgn}(\mu) \frac{\Delta x}{2} \left(\sigma_s \phi_x + q_x - \sigma_t \psi_x - \mathrm{sgn}(\eta) |\eta| \psi_{xy} \right) \\
&+ \mathrm{sgn}(\eta) \frac{\Delta y}{2} \left(\sigma_s \phi_y + q_y - \sigma_t \psi_y - \mathrm{sgn}(\mu) |\mu| \psi_{xy} \right). \quad (4.6)
\end{aligned}
$$

Equation 4.6 is not guaranteed to be accurate on SC's. Improving the approximations that led to Eq. 4.6 in order to improve the Taylor Expansion's accuracy on SC-intersected cells is outside the scope of this work. The leading order term agrees with the $\mathcal{O}(h)$ convergence in the local L_∞ norm observed in the empirically calculated true residual. The residual for a cell that shares a face with the $[W, E]$ boundary takes the form

$$\begin{aligned} R_{0,0}^{(i\in[W,E],j)} &= \sigma_s \phi_{0,0}^{(i\in[W,E],j)} + q_{0,0}^{(i\in[W,E],j)} - \sigma_t \psi_{0,0}^{(i\in[W,E],j)} \\ &\qquad - \frac{|\mu|}{\Delta x}\left[\psi_{0,0}^{(i\in[W,E],j)} - \psi_{l=0}^{[W,E]}\right] - \frac{|\eta|}{\Delta y}\left[\psi_{0,0}^{(i\in[W,E],j)} - \psi_{0,0}^{(i\in[W,E],j-\text{sgn}(\eta))}\right]. \end{aligned}$$

Note that incoming flux does not have x-dependency, hence the specification that $l = 0$. Similar to approximating the residual in the domain, Eqs. 4.3 and 4.5, along with the appropriate equation for the boundary moment, are inserted in the above equation to get the following equation, where a bar denotes that the quantity is known exactly from the BC'S:

$$\begin{aligned} R_{0,0}^{(i\in[W,E],j)} &= \sigma_s\left(\phi + \text{sgn}(\mu)\frac{\Delta x}{2}\phi_x + \text{sgn}(\eta)\frac{\Delta y}{2}\phi_y\right) \\ &+ \left(q + \text{sgn}(\mu)\frac{\Delta x}{2}q_x + \text{sgn}(\eta)\frac{\Delta y}{2}q_y\right) - \sigma_t\left(\bar{\psi} + \text{sgn}(\mu)\frac{\Delta x}{2}\psi_x + \text{sgn}(\eta)\frac{\Delta y}{2}\bar{\psi}_y\right) \\ &- \frac{|\mu|}{\Delta x}\left[\text{sgn}(\mu)\frac{\Delta x}{2}\psi_x + \text{sgn}(\mu)\frac{\Delta x^2}{6}\psi_{xx} + \text{sgn}(\mu)\text{sgn}(\eta)\frac{\Delta x\Delta y}{4}\psi_{xy}\right] \\ &\qquad - \frac{|\eta|}{\Delta y}\left[\text{sgn}(\eta)\Delta y\bar{\psi}_y + \text{sgn}(\mu)\text{sgn}(\eta)\frac{\Delta x\Delta y}{2}\psi_{xy}\right] + \mathcal{O}(h^2). \end{aligned}$$

Once again, the $\mathcal{O}(h^2)$ accuracy is only valid when the cell or a cell directly downwind is not intersected by a SC. Dropping the leading order term since it satisfies the exact transport equation at the point (x_i, y_j) and grouping terms gives the estimate

$$\begin{aligned} \mathcal{R}_{0,0}^{(i\in[W,E],j)} &= -\left\{\sigma_t\bar{\psi} + \mu\psi_x + \eta\bar{\psi}_y - \sigma_s\phi - q\right\} \\ &+ \text{sgn}(\mu)\frac{|\mu|}{2}\psi_x + \text{sgn}(\mu)\frac{\Delta x}{2}\left(\sigma_s\phi_x + q_x - \sigma_t\psi_x - \frac{|\mu|}{3}\psi_{xx} - \text{sgn}(\eta)|\eta|\psi_{xy}\right) \\ &\qquad + \text{sgn}(\eta)\frac{\Delta y}{2}\left(\sigma_s\phi_y + q_y - \sigma_t\bar{\psi}_y - \text{sgn}(\mu)\frac{|\mu|}{2}\psi_{xy}\right). \end{aligned}$$

Before the equation can be further simplified, it must be recognized that while this equation is valid, since the fixed source and scattering source exist on the internal trace of the boundary, the approximation requires modification, since neither quantity exists on the external trace of the boundary. Therefore, the combined source is substituted with its transport equation equivalent, and the equation is simplified to give the equation for the residual in a cell whose boundary includes the $[W, E]$ global boundary

$$\begin{aligned} \mathcal{R}_{0,0}^{(i\in[W,E],j)} &= \text{sgn}(\mu)\frac{|\mu|}{2}\psi_x + \text{sgn}(\mu)\frac{\Delta x}{2}\left(|\mu|\left(\text{sgn}(\mu) - \frac{1}{3}\right)\psi_{xx}\right) \\ &\qquad + \text{sgn}(\eta)\frac{\Delta y}{2}\left(\text{sgn}(\mu)\frac{|\mu|}{2}\psi_{xy} + \text{sgn}(\eta)|\eta|\bar{\psi}_{yy}\right). \qquad (4.7) \end{aligned}$$

Using an analogous derivation, the equation for the residual in a cell whose boundary includes the $[N, S]$ global boundary is

$$\mathcal{R}_{0,0}^{(i,j\in[N,S])} = \text{sgn}(\eta)\frac{|\eta|}{2}\psi_y + \text{sgn}(\mu)\frac{\Delta x}{2}\left(\text{sgn}(\eta)\frac{|\eta|}{2}\psi_{xy} + \text{sgn}(\mu)|\mu|\bar{\psi}_{xx}\right) + \text{sgn}(\eta)\frac{\Delta y}{2}\left(|\eta|\left(\text{sgn}(\eta) - \frac{1}{3}\right)\psi_{yy}\right). \quad (4.8)$$

These equations show that the residual on a cell that borders the global boundary converges with $\mathcal{O}(1)$ in the local L_∞ norm, in agreement with the empirical results reported in Section 3.3.

Using an analogous procedure, the residual in a cell that shares boundaries with both the $[W, E]$ and $[N, S]$ global boundaries (i.e., a corner cell) is given by

$$R_{0,0}^{(i\in[W,E],j\in[N,S])} = \sigma_s\phi_{0,0}^{(i\in[W,E],j\in[N,S])} + q_{0,0}^{(i\in[W,E],j\in[N,S])} - \sigma_t\psi_{0,0}^{(i\in[W,E],j\in[N,S])} - \frac{|\mu|}{\Delta x}\left[\psi_{0,0}^{(i\in[W,E],j\in[N,S])} - \psi_{l=0}^{[W,E]}\right] - \frac{|\eta|}{\Delta y}\left[\psi_{0,0}^{(i\in[W,E],j\in[N,S])} - \psi_{k=0}^{[N,S]}\right].$$

After substituting in Eq. 4.3 the equation becomes

$$\begin{aligned}R_{0,0}^{(i\in[W,E],j\in[N,S])} &= \sigma_s\left(\phi + \text{sgn}(\mu)\frac{\Delta x}{2}\phi_x + \text{sgn}(\eta)\frac{\Delta y}{2}\phi_y\right)\\ &+ \left(q + \text{sgn}(\mu)\frac{\Delta x}{2}q_x + \text{sgn}(\eta)\frac{\Delta y}{2}q_y\right) - \sigma_t\left(\bar{\psi} + \text{sgn}(\mu)\frac{\Delta x}{2}\bar{\psi}_x + \text{sgn}(\eta)\frac{\Delta y}{2}\bar{\psi}_y\right)\\ &- \frac{|\mu|}{\Delta x}\left[\text{sgn}(\mu)\frac{\Delta x}{2}\bar{\psi}_x + \text{sgn}(\mu)\frac{\Delta x^2}{6}\psi_{xx} + \text{sgn}(\mu)\text{sgn}(\eta)\frac{\Delta x\Delta y}{4}\bar{\psi}_{xy}\right]\\ &- \frac{|\eta|}{\Delta y}\left[\text{sgn}(\eta)\frac{\Delta y}{2}\bar{\psi}_y + \text{sgn}(\eta)\frac{\Delta y^2}{6}\bar{\psi}_{yy} + \text{sgn}(\mu)\text{sgn}(\eta)\frac{\Delta x\Delta y}{4}\bar{\psi}_{xy}\right] + \mathcal{O}(h^2).\end{aligned}$$

Note that while this equation as written is $\mathcal{O}(h^2)$ accurate, this feature, as with the other expressions, may be lost when intersected by a SC. By definition, the corner cell must be intersected by a SC in all problems except those that are infinitely differentiable. Grouping terms gives the estimate

$$\begin{aligned}\mathcal{R}_{0,0}^{(i\in[W,E],j\in[N,S])} &= -\left\{\sigma_t\bar{\psi} + \mu\bar{\psi}_x\eta\bar{\psi}_y - \sigma_s\phi - q\right\} + \text{sgn}(\mu)\frac{|\mu|}{2}\bar{\psi}_x + \text{sgn}(\eta)\frac{|\eta|}{2}\bar{\psi}_y\\ &+ \text{sgn}(\mu)\frac{\Delta x}{2}\left(\sigma_s\phi_x + q_x - \sigma_t\bar{\psi}_x - \frac{|\mu|}{3}\bar{\psi}_{xx} - \text{sgn}(\eta)\frac{|\eta|}{2}\bar{\psi}_{xy}\right)\\ &+ \text{sgn}(\eta)\frac{\Delta y}{2}\left(\sigma_s\phi_y + q_y - \sigma_t\bar{\psi}_y - \text{sgn}(\mu)\frac{|\mu|}{2}\bar{\psi}_{xy} - \frac{|\eta|}{3}\bar{\psi}_{yy}\right).\end{aligned}$$

The combined source is substituted, and the equation is simplified to give the estimate for the residual in a corner cell

$$\begin{aligned}\mathcal{R}_{0,0}^{(i\in[W,E],j\in[N,S])} &= \operatorname{sgn}(\mu)\frac{|\mu|}{2}\bar{\psi}_x + \operatorname{sgn}(\eta)\frac{|\eta|}{2}\bar{\psi}_y \\ &\quad + \operatorname{sgn}(\mu)\frac{\Delta x}{2}\left(|\mu|\left(\operatorname{sgn}(\mu)-\frac{1}{3}\right)\bar{\psi}_{xx} + \operatorname{sgn}(\eta)\frac{|\eta|}{2}\bar{\psi}_{xy}\right) \\ &\quad + \operatorname{sgn}(\eta)\frac{\Delta y}{2}\left(\operatorname{sgn}(\mu)\frac{|\mu|}{2}\bar{\psi}_{xy} + \left(\operatorname{sgn}(\eta)-\frac{1}{3}\right)\bar{\psi}_{yy}\right). \qquad (4.9)\end{aligned}$$

Now residual approximations exist for all three types of cells, domain cells, boundary cells, and corner cells, in terms of the point-wise true solution. With MMS these values are possible to obtain; however, to make a truly *a posteriori* estimator, they must be approximated. Because the fixed source, $q(x,y)$, is known exactly as part of the problem configuration, it needs not be approximated. The approximation of these quantities with DGFEM-0 solutions will be detailed in Section 4.2.

4.1.2 Resultant Residual and Error Approximation

With the introduction of this approximation, it is worthwhile to look at the resultant residual and error estimation and compare them to their true counterparts to identify where this first level of approximation will excel or fail. We consider the Taylor Expansion with MMS Quantities (TE-MMS) residual and resultant error estimation (LeR/TE-MMS) for the same cases as with the true residual to identify potential problem areas that may arise when a completely *a posteriori* estimator is implemented.

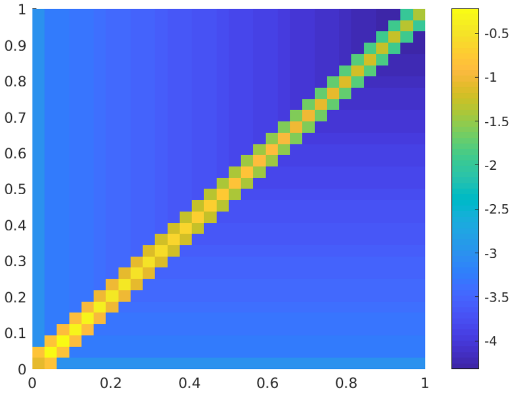

Figure 4.1 $\log_{10}\left|R_h^0(x,y) - \mathcal{R}_{h,\text{TE-MMS}}^0(x,y)\right|$ in Quadrant 1, $\mu_n = \eta_n = 0.35002$, $N_X = N_Y = 32$

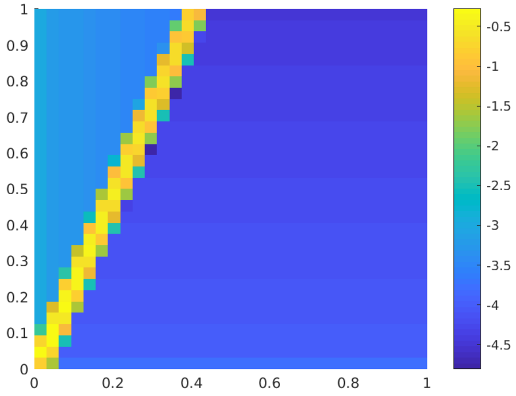

Figure 4.2 $\log_{10}\left|R_h^0(x,y) - \mathcal{R}_{h,\text{TE-MMS}}^0(x,y)\right|$ in Quadrant 1, $\mu_n = 0.35002$, $\eta_n = 0.86889$, $N_X = N_Y = 32$

Figures 4.1-4.3 show the $\log_{10}$-scale difference between the estimated and true residual for

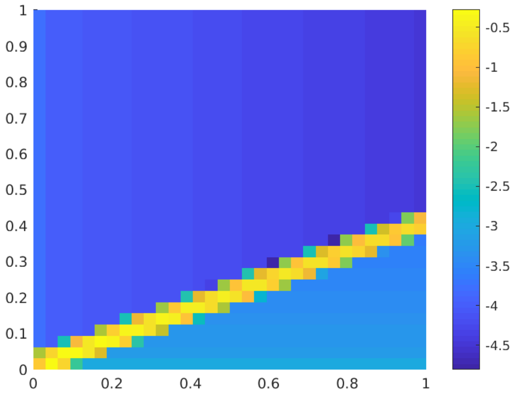

Figure 4.3 $\log_{10}\left|R_h^0(x,y) - \mathcal{R}^0_{h,\text{TE-MMS}}(x,y)\right|$ in Quadrant 1, $\mu_n = 0.86889$, $\eta_n = 0.35002$, $N_X = N_Y = 32$

Quadrant 1 for an H^1 problem with $\sigma_t = 1.0$, $c = 0.9$, and $N_X = N_Y = 32$. These plots show that the TE-MMS residual provides good agreement with the true residual on the boundaries and in the domain. However, approximation is poor along SC-influenced cells. This is because the discontinuities in the first derivative of the true solution are not properly accounted for in the Taylor Expansion approximation of the true solution.

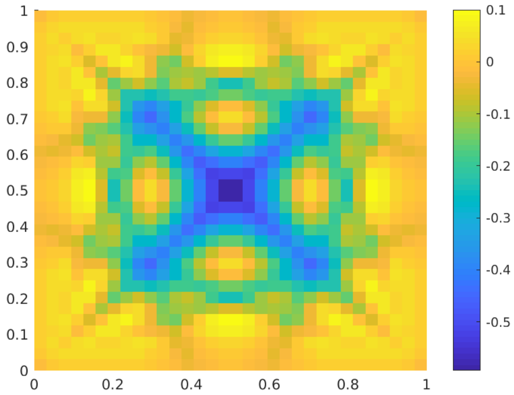

Figure 4.4 $\log_{10}\theta^{(i,j)}_{ang.}$ for LeR/TE-MMS, $N_X = N_Y = 32$

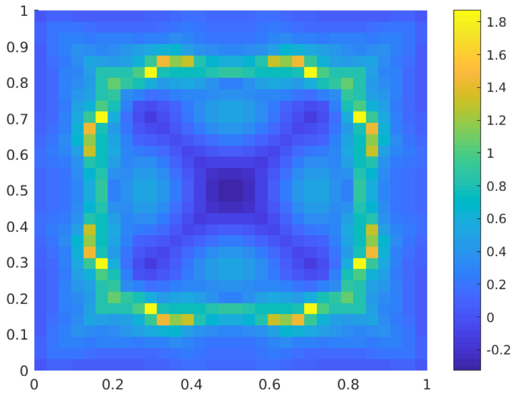

Figure 4.5 $\log_{10}\theta^{(i,j)}_{sca.}$ for LeR/TE-MMS, $N_X = N_Y = 32$

Plotting the $\log_{10}\theta^{(i,j)}_{ang./sca.}$ in the domain, where $\theta_{ang./sca.}$ is computed from the error estimated with the LeR/TE-MMS estimator, Figures 4.4 and 4.5, shows where potential problem regions may exist in estimating the error. Problem regions exist towards the center of the domain where the effects of SCs seem to magnify poor estimations in the error.

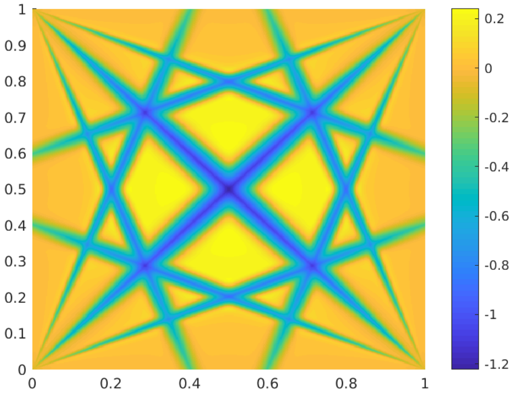

Figure 4.6 $\log_{10}\theta_{ang.}^{(i,j)}$ for LeR/TE-MMS, $N_X = N_Y = 512$

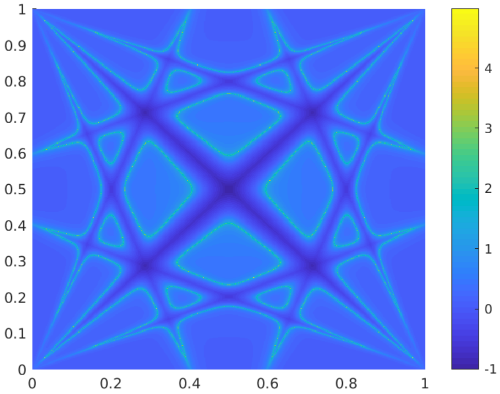

Figure 4.7 $\log_{10}\theta_{sca.}^{(i,j)}$ for LeR/TE-MMS, $N_X = N_Y = 512$

We can get a clearer picture by refining the mesh to $N_X = N_Y = 512$, Figures 4.6 and 4.7. These plots show obvious problem regions concentrated around the SCs due to the numerical spread of error from the poorly-approximated residual on the SC-intersected and neighboring cells. We know from Figures 3.6 and 3.7 and Figures 3.11 and 3.12 for $N_X = N_Y = 512$ that the areas around the SCs are also regions of large error.

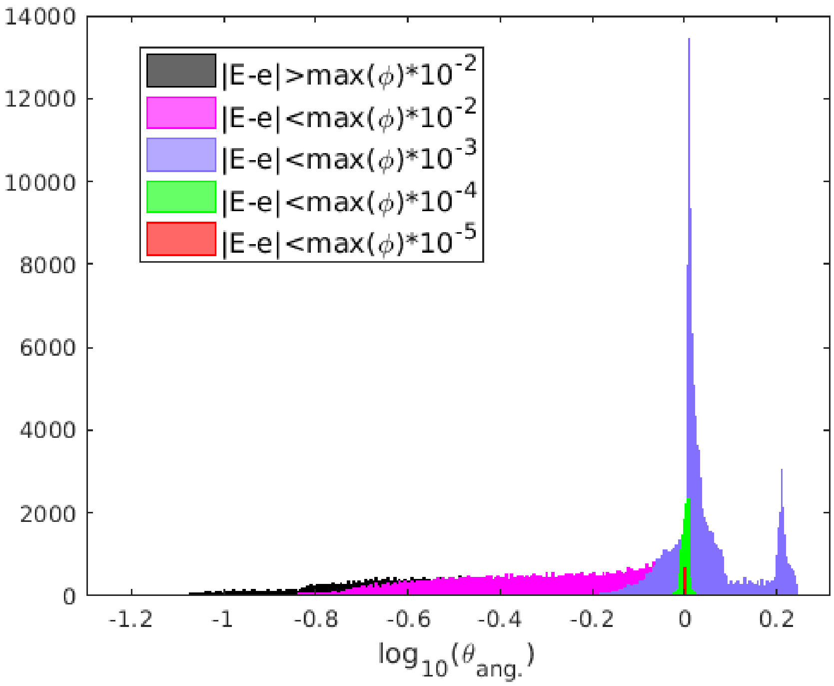

Figure 4.8 $\log_{10}(\theta_{ang.}^{(i,j)})$ Histogram for LeR/TE-MMS, $N_X = N_Y = 512$

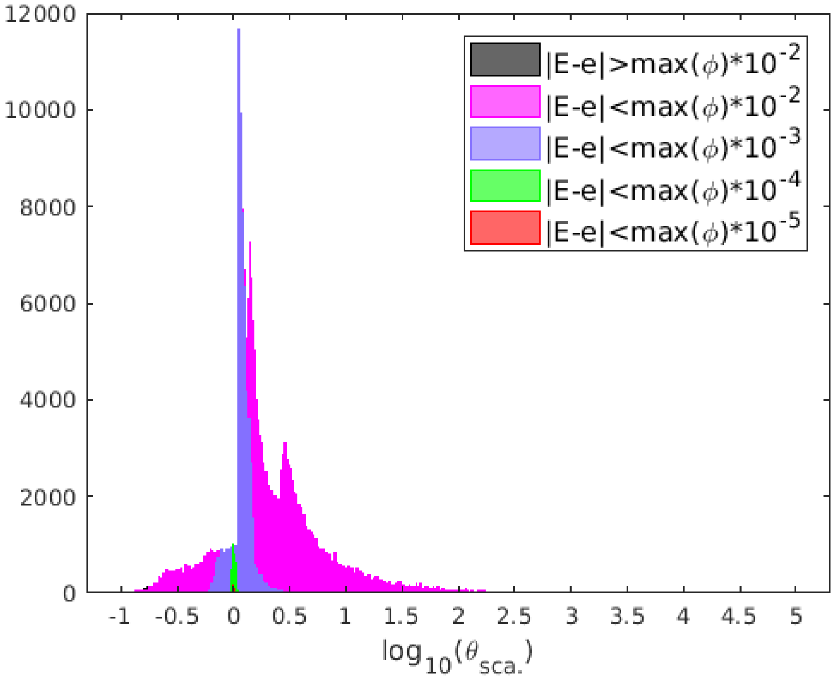

Figure 4.9 $\log_{10}(\theta^{(i,j)}_{sca.})$ Histogram for LeR/TE-MMS, $N_X = N_Y = 512$

Also useful is plotting histograms of $\log_{10}\theta^{(i,j)}_{ang./sca.}$ to determine the distribution of the estimator's accuracy over cells in the mesh. We can see from Figure 4.8 that the majority of angular effectivities are concentrated about a very tight window close to $\log_{10}(\theta^{(i,j)}_{ang.}) = 0$, meaning exact agreement. There exists a smaller peak of values at a slight over estimate ($\log_{10}(\theta^{(i,j)}_{ang.}) \approx 0.2$) that correspond with the interference-like pattern in the center area of the plot. Finally, the long string of underestimated values that stretch to $\log_{10}(\theta^{(i,j)}_{ang.}) \approx -1.2$ belong to the SCs and nearby cells. In Figure 4.9, the histogram of scalar effectivities, the pattern is somewhat similar, but the scalar L_2 norm clearly generally results in much larger over and underestimation; although, the bulk of values are still within one order of magnitude from exact. Note that the number of cells with very large effectivities is so small that they are nearly invisible in Figure **??**. The color-coding in the histogram plots corresponds to the absolute difference between the true error and estimated error. This is to point out areas where the true error is close to zero and the estimated error is also low but not low enough to give a good effectivity value (e.g., if $E = 10^{-8}$ and $e = 10^{-6}$ this will give an effectivity of $\log_{10}\theta^{(i,j)} = 2$, which suggests poor performance, even though the error estimate is sufficiently small to consider it a good approximation).

4.2 Approximating Derivatives

4.2.1 Derivation

To make a truly *a posteriori* estimator, the residual approximation must be based on DGFEM-0 solutions exclusively. Therefore, it is necessary to replace the pointwise MMS quantities with DGFEM-0 quantities. Because the residual is orthogonal to the solution space, however, all required derivative values in DGFEM-0 are zero (recall that DGFEM-0 approximates the solution as piecewise constant), meaning derivatives must be approximated. This is not entirely different than the process required in recovery-based error estimators, in which an "improved" approximation of gradients is used to reconstruct the error [28][5]; although in this case we attempt to reconstruct the residual. In this work the derivatives are approximated by integrating the Taylor Expansion across neighboring cells to the origin of the subject cell to find moment expressions and use those moment expressions to solve for the derivatives. The four resultant $\mathcal{O}(h^3)$ moment equations are

$$\begin{aligned}\psi_{0,0}^{(i,j)} \approx \psi + \mathrm{sgn}(\mu_n)\frac{\Delta x}{2}\psi_x + \mathrm{sgn}(\eta_n)\frac{\Delta y}{2}\psi_y + \mathrm{sgn}(\mu_n)\frac{\Delta x^2}{6}\psi_{xx} \\ + \mathrm{sgn}(\mu_n)\mathrm{sgn}(\eta_n)\frac{\Delta x \Delta y}{4}\psi_{xy} + \mathrm{sgn}(\eta_n)\frac{\Delta y^2}{6}\psi_{yy},\end{aligned}$$

$$\begin{aligned}\psi_{0,0}^{(i-\mathrm{sgn}(\mu_n),j)} \approx \psi - \mathrm{sgn}(\mu_n)\frac{\Delta x}{2}\psi_x + \mathrm{sgn}(\eta_n)\frac{\Delta y}{2}\psi_y + \mathrm{sgn}(\mu_n)\frac{\Delta x^2}{6}\psi_{xx} \\ - \mathrm{sgn}(\mu_n)\mathrm{sgn}(\eta_n)\frac{\Delta x \Delta y}{4}\psi_{xy} + \mathrm{sgn}(\eta_n)\frac{\Delta y^2}{6}\psi_{yy},\end{aligned}$$

$$\begin{aligned}\psi_{0,0}^{(i,j-\mathrm{sgn}(\eta_n))} \approx \psi + \mathrm{sgn}(\mu_n)\frac{\Delta x}{2}\psi_x - \mathrm{sgn}(\eta_n)\frac{\Delta y}{2}\psi_y + \mathrm{sgn}(\mu_n)\frac{\Delta x^2}{6}\psi_{xx} \\ - \mathrm{sgn}(\mu_n)\mathrm{sgn}(\eta_n)\frac{\Delta x \Delta y}{4}\psi_{xy} + \mathrm{sgn}(\eta_n)\frac{\Delta y^2}{6}\psi_{yy},\end{aligned}$$

and

$$\begin{aligned}\psi_{0,0}^{(i-\mathrm{sgn}(\mu_n),j-\mathrm{sgn}(\eta_n))} \approx \psi - \mathrm{sgn}(\mu_n)\frac{\Delta x}{2}\psi_x - \mathrm{sgn}(\eta_n)\frac{\Delta y}{2}\psi_y + \mathrm{sgn}(\mu_n)\frac{\Delta x^2}{6}\psi_{xx} \\ + \mathrm{sgn}(\mu_n)\mathrm{sgn}(\eta_n)\frac{\Delta x \Delta y}{4}\psi_{xy} + \mathrm{sgn}(\eta_n)\frac{\Delta y^2}{6}\psi_{yy}.\end{aligned}$$

It is noted that $\psi + \mathrm{sgn}(\mu_n)\frac{\Delta x^2}{6}\psi_{xx} + \mathrm{sgn}(\eta_n)\frac{\Delta y^2}{6}\psi_{yy}$ appears in all four equations, and it is collapsed into a single variable Ψ, resulting in a total of four unknowns and four equations.

Solving these equations gives $\mathcal{O}(\Delta^2)$ expressions for the first-order derivatives,

$$\psi_x \approx \frac{\text{sgn}(\mu_n)}{2\Delta x}\left(\psi_{0,0}^{(i,j)} - \psi_{0,0}^{(i-\text{sgn}(\mu_n),j)} + \psi_{0,0}^{(i,j-\text{sgn}(\eta_n))} - \psi_{0,0}^{(i-\text{sgn}(\mu_n),j-\text{sgn}(\eta_n))}\right) \tag{4.10}$$

$$\psi_y \approx \frac{\text{sgn}(\eta_n)}{2\Delta y}\left(\psi_{0,0}^{(i,j)} + \psi_{0,0}^{(i-\text{sgn}(\mu_n),j)} - \psi_{0,0}^{(i,j-\text{sgn}(\eta_n))} - \psi_{0,0}^{(i-\text{sgn}(\mu_n),j-\text{sgn}(\eta_n))}\right) \tag{4.11}$$

and an $\mathcal{O}(h)$ expression for the $\frac{\partial^2}{\partial x \partial y}$ derivative,

$$\begin{aligned}\psi_{xy} \approx \frac{\text{sgn}(\mu_n)\text{sgn}(\eta_n)}{\Delta x \Delta y}\Big(&\psi_{0,0}^{(i,j)} - \psi_{0,0}^{(i-\text{sgn}(\mu_n),j)} \\ &- \psi_{0,0}^{(i,j-\text{sgn}(\eta_n))} + \psi_{0,0}^{(i-\text{sgn}(\mu_n),j-\text{sgn}(\eta_n))}\Big)\end{aligned} \tag{4.12}$$

These equations are invalid for a cell that shares a face with the boundary. To account for this, the original system of equations must be re-derived for such a cell. Beginning with a cell sharing a face with the $[W,E]$ boundary, the $\mathcal{O}(h^3)$ equations are

$$\begin{aligned}\psi_{0,0}^{(i\in[W,E],j)} \approx \bar{\psi} + \text{sgn}(\mu_n)\frac{\Delta x}{2}\psi_x + \text{sgn}(\eta_n)\frac{\Delta y}{2}\bar{\psi}_y + \text{sgn}(\mu_n)\frac{\Delta x^2}{6}\psi_{xx} \\ + \text{sgn}(\mu_n)\text{sgn}(\eta_n)\frac{\Delta x \Delta y}{4}\psi_{xy} + \text{sgn}(\eta_n)\frac{\Delta y^2}{6}\bar{\psi}_{yy},\end{aligned}$$

and

$$\begin{aligned}\psi_{0,0}^{(i\in[W,E],j-\text{sgn}(\eta_n))} \approx \bar{\psi} + \text{sgn}(\mu_n)\frac{\Delta x}{2}\psi_x - \text{sgn}(\eta_n)\frac{\Delta y}{2}\bar{\psi}_y + \text{sgn}(\mu_n)\frac{\Delta x^2}{6}\psi_{xx} \\ - \text{sgn}(\mu_n)\text{sgn}(\eta_n)\frac{\Delta x \Delta y}{4}\psi_{xy} + \text{sgn}(\eta_n)\frac{\Delta y^2}{6}\bar{\psi}_{yy}.\end{aligned}$$

As before, a bar above a value indicates that it is known from the BC's. The problem can be immediately seen: there are three unknowns and only two equations. Because the residual on a boundary layer cell has been shown to converge with $\mathcal{O}(1)$ in the L_∞ norm it is considered acceptable to reduce the accuracy of the equations to $\mathcal{O}(h^2)$, giving the following equations:

$$\psi_{0,0}^{(i\in[W,E],j)} \approx \bar{\psi} + \text{sgn}(\mu_n)\frac{\Delta x}{2}\psi_x + \text{sgn}(\eta_n)\frac{\Delta y}{2}\bar{\psi}_y,$$

and

$$\psi_{0,0}^{(i\in[W,E],j-\text{sgn}(\eta_n))} \approx \bar{\psi} + \text{sgn}(\mu_n)\frac{\Delta x}{2}\psi_x - \text{sgn}(\eta_n)\frac{\Delta y}{2}\bar{\psi}_y.$$

The resulting $\mathcal{O}(h)$ accurate approximation for the x-derivative is

$$\psi_x \approx \frac{\text{sgn}(\mu_n)}{\Delta x}\left(\psi_{0,0}^{(i\in[W,E],j)} + \psi_{0,0}^{(i\in[W,E],j-\text{sgn}(\eta_n))} - 2\bar{\psi}\right). \tag{4.13}$$

Similarly, for a cell sharing a face with the $[N,S]$ boundary the $\mathcal{O}(h)$ accurate approximation for the y-derivative is

$$\psi_y \approx \frac{\text{sgn}(\eta_n)}{\Delta y}\left(\psi_{0,0}^{(i,j\in[W,E])} + \psi_{0,0}^{(i-\text{sgn}(\mu_n),j\in[W,E])} - 2\bar{\psi}\right). \tag{4.14}$$

For a cell sharing a face with both $[W, E]$ and $[N, S]$ boundaries (i.e., on a corner) there is no approximation of pointwise derivatives required, as all required corner values come from the BC's, provided the solution is sufficiently regular on the boundary. Note that, in general, all approximations do not necessarily maintain their order of accuracy along cells that are intersected by a SC, depending on the regularity of the solution.

4.2.2 Resultant Residual and Error Approximation

A comparison between the Taylor Expansion with approximated derivatives (TE-AD) residual and true residual, as well as the residual source estimate with TE-AD residual as an input (LeR/TE-AD) and true error, is now in order. Figures 4.10-4.12 show that the TE-AD residual approximates the true residual less accurately than the TE-MMS residual, generally (see Figures 4.1-4.3 for comparison). The absolute difference between the TE-AD and true residuals is about 1.5-2 orders of magnitude larger than the difference between the TE-MMS and true residuals. Because the true pointwise derivative of the scattering source is no longer perfectly approximated the SCs from other ordinates manifest in the residual for a given ordinate (recall that the true derivative of the combined source is zero for the problems in this work). Also note that numerical spreading in the discrete solution along the SCs has lead to larger error in the TE-AD residual near the SCs due to approximation of the pointwise derivatives with the

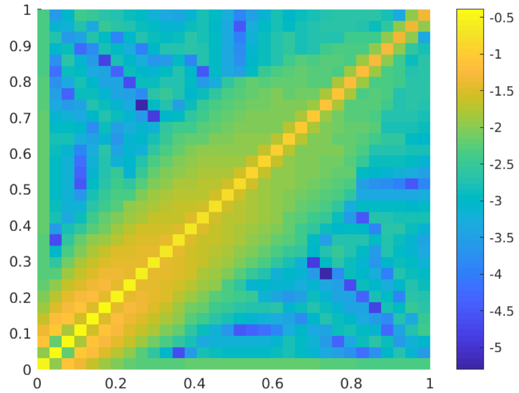

Figure 4.10 $\log_{10}\left|R_h^0(x,y) - \mathcal{R}_{h,\text{TE-AD}}^0(x,y)\right|$ in Quadrant 1, $\mu_n = \eta_n = 0.35002$, $N_X = N_Y = 32$

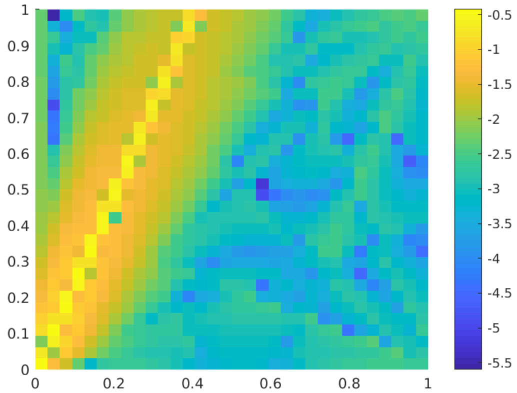

Figure 4.11 $\log_{10}\left|R_h^0(x,y) - \mathcal{R}_{h,\text{TE-AD}}^0(x,y)\right|$ in Quadrant 1, $\mu_n = 0.35002$, $\eta_n = 0.86889$, $N_X = N_Y = 32$

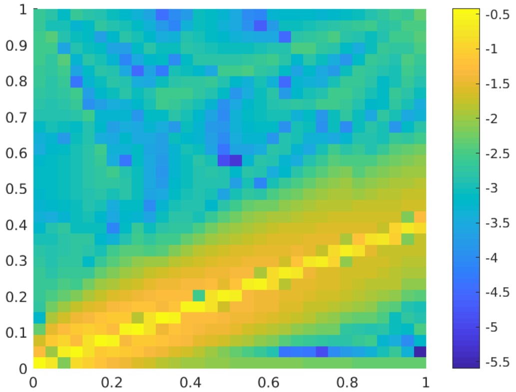

Figure 4.12 $\log_{10}\left|R_h^0(x,y) - \mathcal{R}^0_{h,\text{TE-AD}}(x,y)\right|$ in Quadrant 1, $\mu_n = 0.86889$, $\eta_n = 0.35002$, $N_X = N_Y = 32$

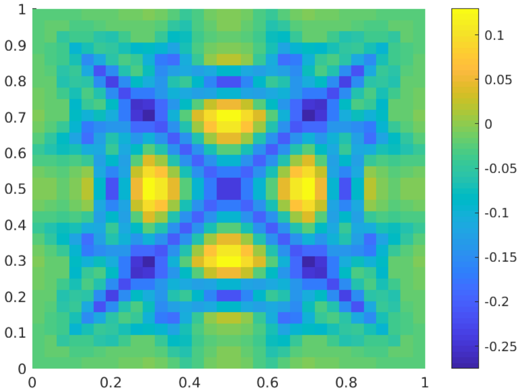

Figure 4.13 $\log_{10}\theta^{(i,j)}_{ang.}$ for LeR/TE-AD Estimator, $N_X = N_Y = 32$

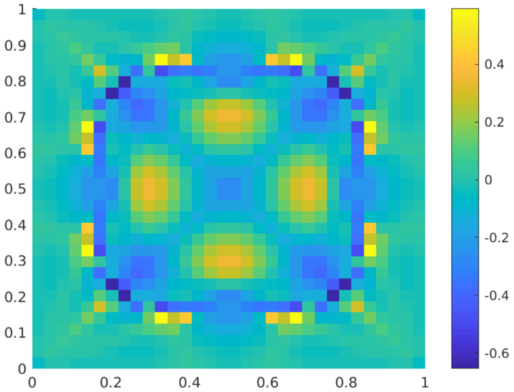

Figure 4.14 $\log_{10}\theta^{(i,j)}_{sca.}$ for LeR/TE-AD Estimator, $N_X = N_Y = 32$

numerical solution.

The resultant error estimations plotted in the domain, Figures 4.13 and 4.14, appear similar to the LeR/TE-MMS estimates, Figures 4.4-4.5, in terms of distribution, with areas of poorest accuracy of the estimated error located on the SCs and in interference-like patterns around the center of the domain.

Refining the mesh to $N_X = N_Y = 512$ and examining the error estimation, Figures 4.15 and 4.16, shows the distribution of errors more clearly. Also, the upper and lower bounds on the effectivity distribution are larger than the $N_X = N_Y = 32$ case.

The histogram of the angular effectivity, Figure 4.17, shows the majority of values are contained within a small window about $\log_{10}(\theta_{ang.}) = 0$. In this problem the angular effectivity favors overestimation slightly, although all values are bound between about $\log_{10}(\theta_{ang.}) = -0.3$

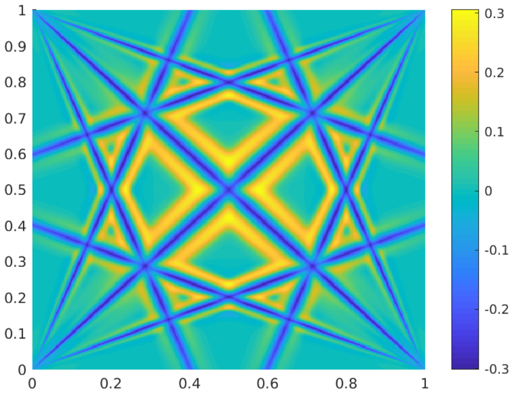

Figure 4.15 $\log_{10}\theta^{(i,j)}_{ang.}$ for LeR/TE-AD Estimator, $N_X = N_Y = 512$

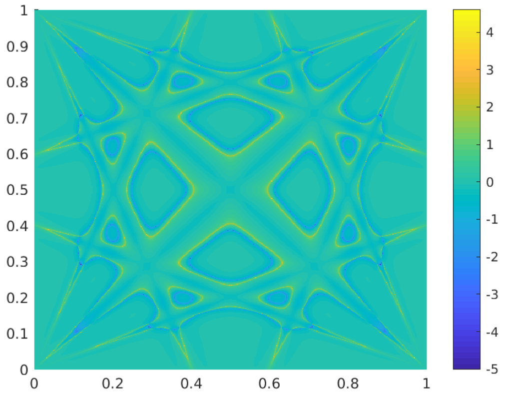

Figure 4.16 $\log_{10}\theta^{(i,j)}_{sca.}$ for LeR/TE-AD Estimator, $N_X = N_Y = 512$

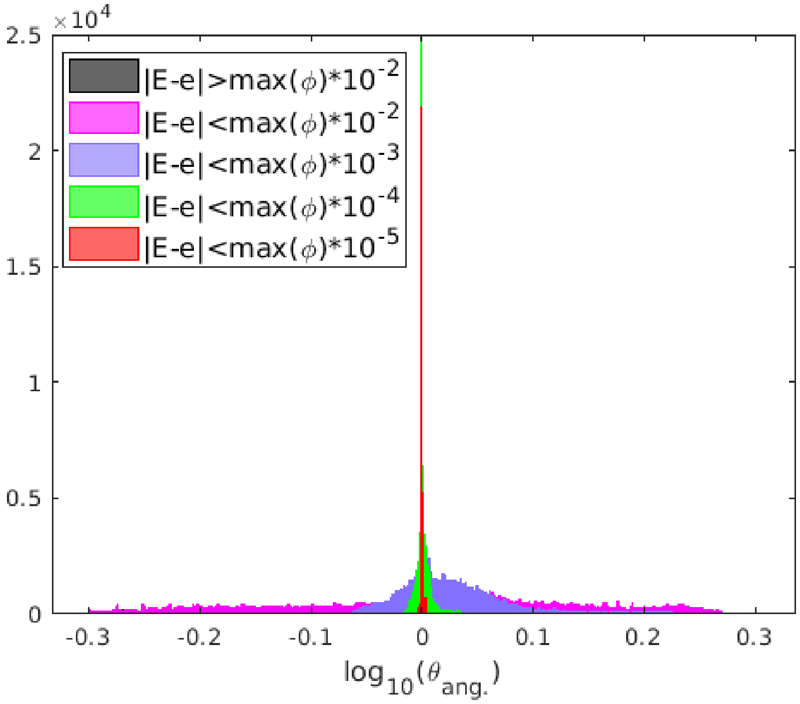

Figure 4.17 $\log_{10}(\theta^{(i,j)}_{ang.})$ Histogram for LeR/TE-AD Estimator, $N_X = N_Y = 512$

and $\log_{10}(\theta_{ang.}) = 0.3$. Versus the angular effectivity histogram for the LeR/TE-MMS estimate, Figure 4.8, the LeR/TE-AD estimate is surprisingly robust. The "peak" of values centered at exact agreement is higher than in the LeR/TE-MMS estimate, the minimum-to-maximum log_{10}-scale width of the effectivity distributions is smaller than the LeR/TE-MMS estimate, and there exists no additional "sub-peak" for values contained in the interference-like region. Intuitively, the residual with more approximations should be a poorer estimate, which begs the question of *why* the LeR/TE-AD estimate is superior to the LeR/TE-MMS estimate?

While the TE-MMS residual is generally a superior approximation away from SCs, the TE-AD residual approximation is actually superior in cells that are influenced by SCs because the derivatives are approximated by the numerical solution rather than a wholly incorrect (due to the irregularity) pointwise derivative representation. Because the true residual is so large in cells that are influenced by SCs, correctly approximating the residual in these cells carries more importance than other cells.

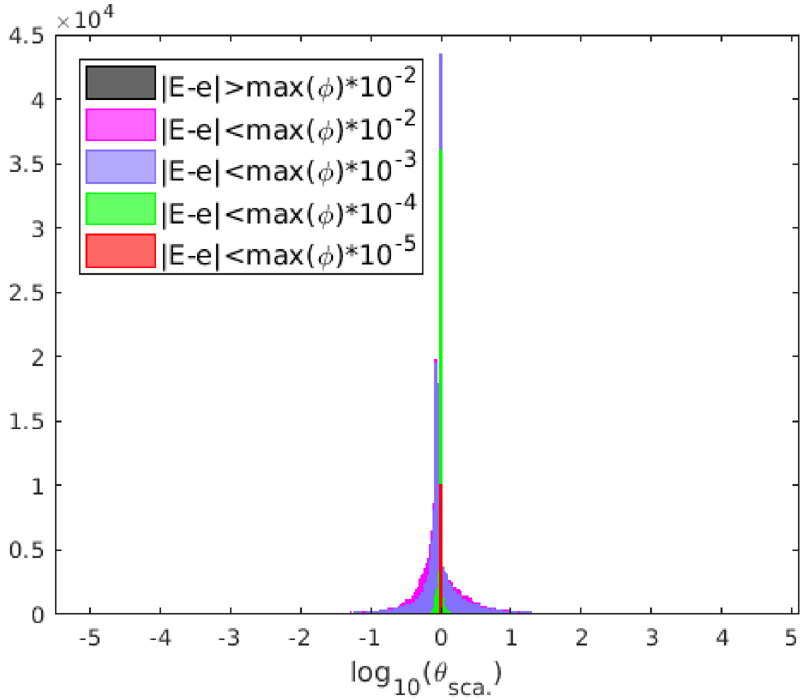

Figure 4.18 $\log_{10}(\theta_{sca.}^{(i,j)})$ Histogram for LeR/TE-AD Estimator, $N_X = N_Y = 512$

By examining the histogram of the scalar effectivity, Figure 4.18, one can reach a conclusion similar to the one reached from the TE-MMS analysis, Figure 4.9. The scalar effectivity appears similar to the angular effectivity, but it has long tails that stretch in either direction many orders of magnitude. However, the vast majority of values are located within one order of magnitude from exact agreement. Overall, these results show the efficacy of a truly *a posteriori* LeR/TE-AD estimate.

Chapter 5

Alternative Estimators

Ultimately, no estimator is expected to produce perfect agreement with the true error. Choosing an error estimator for practical use would be up to a transport code user based on his or her own subjective interests. However, in an attempt to give at least some idea of the residual source estimator's performance, two alternative estimators are compared to the residual source estimator: the Ragusa-Wang (RW) estimator and the Duo-Azmy-Zikatanov (DAZ) estimator and indicator. In a practical sense the estimators used in this work differ slightly from those introduced by their creators in an effort to keep them consistent with the error norms used to represent estimator and error behavior. Hence, after initially introducing the estimators, the "RW-like" and "DAZ-like" estimators will be interchangeably referred to as "Ragusa-Wang" and "DAZ" estimators, respectively.

5.1 Ragusa-Wang Estimator

The "Ragusa-Wang" estimator is a two-mesh estimator developed in the context of error estimation for adaptive mesh refinement (AMR) [7]. In the RW estimator the spatial mesh is uniformly refined to create a problem with four times as many unknowns as the original problem in 2D (two times as many in 1D, eight times as many in 3D) that must be solved in the same manner as the original problem to find the estimate. The solution on the refined mesh, $\psi_{h/2}$, is essentially treated as an approximation of the reference solution. Their estimator is introduced in [7] in the following form:

$$e_{RW}^{(i,j)} = \frac{\int_{\Delta x_i} dx \int_{\Delta y_j} dy \left(\mathcal{I}_h - \mathcal{I}_{h/2}\right)^2}{\int_{\mathcal{D}} dA \, \mathcal{I}_h^2}, \tag{5.1}$$

where $\mathcal{I}$ is any angle-integrated quantity, such as scalar flux or current. Ragusa and Wang include the denominator as a normalization term, since AMR is driven by relative solution error rather than absolute [9]. To keep their estimator consistent with our definition of the error and error norms, it is reframed in the angular sense, Eq. 5.2, and the scalar sense, Eq. 5.3,

$$e^{(i,j)}_{RW,ang.} = \sqrt{\sum_{n=1}^{N} w_n \int_{\Delta x_i} dx \int_{\Delta y_j} dy \left(\psi^{\Lambda}_{h,n}(x,y) - \left[\Pi_h \psi^{\Lambda}_{h/2,n}\right](x,y)\right)^2}, \tag{5.2}$$

and

$$e^{(i,j)}_{RW,sca.} = \sqrt{\int_{\Delta x_i} dx \int_{\Delta y_j} dy \left(\phi^{\Lambda}_{h}(x,y) - \left[\Pi_h \phi^{\Lambda}_{h/2}\right](x,y)\right)^2}, \tag{5.3}$$

respectively. These expressions are identical in form to Eqs. 2.14 and 2.15, and the global RW-like estimator in both forms is defined in an identical manner.

This estimator has been shown to give a superior estimate of the error when compared to other estimators [9, 10], so it provides a good benchmark for the quality of the residual source estimator. Also, like the residual source estimator, the RW estimator requires an additional transport solve. While the additional transport solve is on a uniformly-refined mesh, the solution can be preconditioned with an initial guess formed by prolongation of the h-mesh solution.

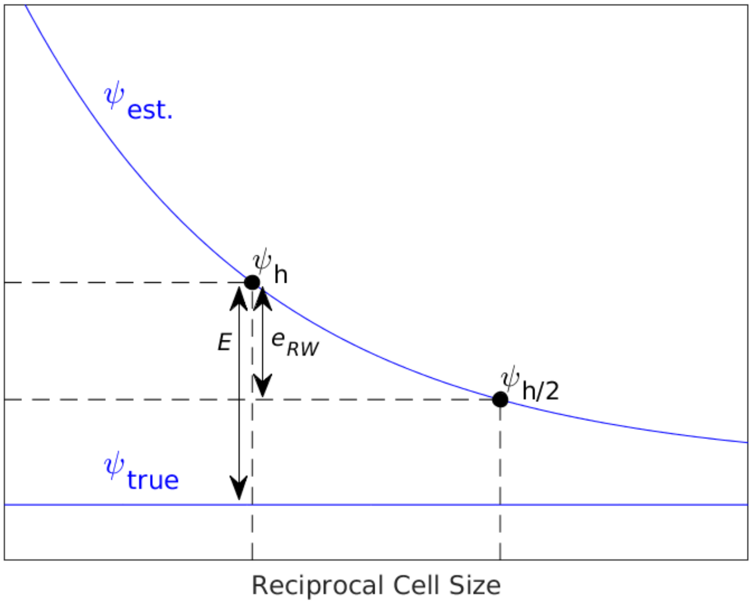

Figure 5.1 Convergence of Estimated Solution vs. True Solution

Previous works ([2, 9, 10]) have shown that the RW estimator will consistently underestimate the true error, and this is because the DGFEM-0 solution will asymptotically approach the true solution, meaning the difference between ψ_h and $\psi_{h/2}$ will always be less than the difference between ψ_h and the true solution, see Figure 5.1. Note that E, the true error, is always greater than e_{RW}, the difference between two solutions [9, 29]. Provided the problem has locally reached the asymptotic regime of solution convergence with respect to mesh size (i.e., $\psi_h^\Lambda(x,y) - \Pi_h^\Lambda \psi_{h/2}^\Lambda(x,y)$) and the order of local convergence is known, this bias is quantifiable. A heuristic analysis shows it to be,

$$\begin{aligned}\frac{\psi_h^\Lambda(x,y) - \Pi_h^\Lambda \psi_{h/2}^\Lambda(x,y)}{\psi_h^\Lambda(x,y) - \Pi_h^\Lambda \psi(x,y)} &= \frac{\left(\psi_h^\Lambda(x,y) - \Pi_h^\Lambda \psi(x,y)\right) - \left(\Pi_h^\Lambda \psi_{h/2}^\Lambda(x,y) - \Pi_h^\Lambda \psi(x,y)\right)}{\psi_h^\Lambda(x,y) - \Pi_h^\Lambda \psi(x,y)} \\ &\approx \frac{Ch^p - Ch^p 2^{-p}}{Ch^p} = 1 - 2^{-p},\end{aligned}$$

as cell thickness approaches zero, where p is the order of local asymptotic convergence. The same process can be applied to the global error estimate as well, where p is instead the order of global asymptotic convergence. It may be possible to use this *a priori* knowledge of the RW estimator bias to apply a "correction factor" of sorts, but the two assumptions required to implement this are quite difficult to achieve in problems that are not as ideal as the ones presented in this work, so the RW estimator is presented as-is, without such correction.

5.2 Duo-Azmy-Zikatanov Estimator and Indicator

The "Duo-Azmy-Zikatanov" estimator is a residual-based estimator developed for AHOT-N that has been shown to bound the global error from above in the L_2 norm [18, 19]. The global estimator is given by,

$$\begin{aligned} e_{DAZ} = \mathcal{C}\Bigg[\sum_{n}^{N} w_n \left(\sum_{i=1}^{N_X} \sum_{j=1}^{N_Y} \hat{h}_{K^{(i,j)}}^{2r} \|\mathcal{R}^{(i,j)}\|_{K^{(i,j)}}^2 \right)^{1/2} \\ + \sum_{n:\vec{\Omega}_n\cdot\hat{n}<0}^{N} w_n \left(\sum_{i=1}^{N_X} \sum_{j=1}^{N_Y} 2\hat{h}_{K^{(i,j)}}^{2r-1} \| |\hat{n}\cdot\vec{\Omega}_n|^{1/2} \left\{ \psi_\Lambda^- - \psi_{\Lambda+l}^+ \right\} \|_{\partial K_-^{(i,j)}} \right)^{1/2} \Bigg], \end{aligned} \tag{5.4}$$

where l is some non-zero positive integer, r is the minimum degree of regularity in the domain (i.e., represents a problem that is H^r), $\hat{h}_{K^{(i,j)}}$ is the diameter of cell $K^{(i,j)}$, and $\mathcal{C}$ is some scaling constant, typically set to 1 [18]. All DAZ estimator and indicator results presented in this work have set $l = 1$. Conceptually, this estimator works by bounding the global error by an estimate of the residual (first term) and an estimate of the high-order terms omitted when transferring information from cell-to-cell during the transport sweep (second term). To approximate the residual and the inter-element jump, the original authors find a higher-order pseudo-solution (HOPS) by doing $N_X \times N_Y$ local, single-cell sweeps with order $\Lambda + l$. The low order solution provides each cell's boundary conditions and the scattering source. In this work the HOPS is found by performing a single full sweep over the mesh with order $\Lambda + l$ using the low order solution to generate the scattering source but keeping the cell incoming boundary flux synchronous. Heuristically applied as a local quantity, the DAZ indicator has the form Eq. 5.5, where $\mathcal{C}$ is a constant independent of mesh size, but dependent on the interpolation in the finite element space, the regularity of the true solution, and the H^1 seminorm of the dual problem and is assumed equal to 1 [19],

$$e^{(i,j)}_{DAZ} = \sum_{n}^{N} w_n \left(\hat{h}^{2r}_{K^{(i,j)}} \left\| \mathcal{R}^{(i,j)} \right\|^2_{K^{(i,j)}} \right)^{1/2} + \sum_{n:\vec{\Omega}_n \cdot \hat{n} < 0}^{N} w_n \left(2\hat{h}^{2r-1}_{K^{(i,j)}} \left\| \left| \hat{n} \cdot \vec{\Omega}_n \right|^{1/2} \left\{ \psi^{-}_{\Lambda} - \psi^{+}_{\Lambda+l} \right\} \right\|_{\partial K^{(i,j)}_{-}} \right)^{1/2} . \quad (5.5)$$

One way in which the DAZ estimator can be viewed is that it is a bound on the error calculated via the Triangle Inequality applied to the residual (represented with an estimate) and an estimate of the information not transmitted by inflow due to truncation of the DGFEM representation. This concept is utilized in a local DAZ-like indicator in the angular sense, Eq. 5.6,

$$e^{(i,j)}_{DAZ,ang.} = \sqrt{\sum_{n}^{N} \hat{h}^{2r}_{K^{(i,j)}} w_n \int_{\Delta x_i} dx \int_{\Delta y_j} dy \, \left(\mathcal{R}^{(i,j)}_n (x,y) \right)^2} + \sqrt{\sum_{n:\vec{\Omega}_n \cdot \hat{n} < 0}^{N} 2\hat{h}^{2r-1}_{K^{(i,j)}} w_n \int_{\partial K^{(i,j)}_{-}} dS \, \left| \hat{n} \cdot \vec{\Omega}_n \right| \left\{ \psi^{-}_{\Lambda,n} - \psi^{+}_{\Lambda+l,n} \right\}^2}, \quad (5.6)$$

where the residual estimate is calculated with a HOPS, calculated in the same manner as the true DAZ estimator. This residual is different than from defined in Eq. 3.3, however, and it is instead approximated as $\mathcal{R}^{(i,j)} = \Pi^{\Lambda+l} \left(\sigma_s \phi^{HOPS}_h + q \right) - \Pi^{\Lambda} \left(\sigma_s \phi_h + q \right)$. The DAZ-like indicator does not have a corresponding scalar estimator due to the jump discontinuities in the flux on the incoming edges that is angularly dependent by definition. In the global sense, the DAZ-like estimator has the form shown in Eq. 5.7,

$$e_{DAZ,ang.} = \sqrt{\sum_{i=1}^{N_X} \sum_{j=1}^{N_Y} \sum_{n}^{N} \hat{h}^{2r}_{K^{(i,j)}} w_n \int_{\Delta x_i} dx \int_{\Delta y_j} dy \, \left(\mathcal{R}^{(i,j)}_n (x,y) \right)^2} + \sqrt{\sum_{i=1}^{N_X} \sum_{j=1}^{N_Y} \sum_{n:\vec{\Omega}_n \cdot \hat{n} < 0}^{N} 2\hat{h}^{2r-1}_{K^{(i,j)}} w_n \int_{\partial K^{(i,j)}_{-}} dS \, \left| \hat{n} \cdot \vec{\Omega}_n \right| \left\{ \psi^{-}_{\Lambda,n} - \psi^{+}_{\Lambda+l,n} \right\}^2} . \quad (5.7)$$

The primary difference between the form of the DAZ estimator and indicator, as presented by Duo, Azmy, and Zikatanov, and the "DAZ-like" estimator and indicators presented here is the ordering of the angular integration and taking the square root. Importantly, the DAZ estimator requires $r \geq 1$ to bound the solution error globally. This means that H^0 problems are not proven to be bounded. While the solution regularity r is an input for the estimator, r will be set to 1 in this work for an H^0 problem for this reason, although this still does not guarantee an error bound. The DAZ estimator and indicator are considered to be similar to the residual source estimator because they are both rooted in estimation of the residual, although the DAZ estimator is cheaper to compute and does not require an extra transport-like solution. Distinction between “estimator” and “indicator” stems from the fact that the estimator has been proven theoretically and empirically to provide a bound on the global error, while no such proof exists for the local error [19].

Chapter 6

Estimators Comparison and Assessment for H^1 Problems

The first set of cases examined are the problems that are in the class H^1. We first qualitatively observe the behavior of the error estimators in selected problems as a case study, and then we quantitatively observe the behavior in terms of global metrics for a wider selection of problems. The problem parameters that are modified throughout the reported comparisons are the optical thickness (via σ_t), which effects the accuracy of the numerical solution and the influence of the SCs, the cell size h via the number of cells $N_X \times N_Y$, which will change the degree to which the numerical solution has asymptotically converged to the true solution and the relative number of cells that are influenced by (intersected by or are downwind from cells intersected by) SCs, and the scattering ratio c, which effects the magnitude of the irregularity in the true solution derivative and the number of source iterations required to reach iterative convergence. The DGFEM order is fixed to 0, and all cases of the residual source estimator utilize the TE-AD residual.

6.1 H^1 Case Study

6.1.1 H^1 Case 1

The first H^1 case to consider has medium optical thickness ($\sigma_t = 1.0$) and a high scattering ratio $c = 0.9$. This is the same case that has been examined up to this point. Initially, the mesh is set to $N_X = N_Y = 32$, as this mesh structure is coarse enough to be in the early stages asymptotic convergence with mesh refinement yet gives an appropriate ratio of cells influenced to cells uninfluenced by SCs.

First we compare of the angular effectivities plotted over the domain for the LeR/TE-AD, RW, and DAZ estimators in Figures 6.1-6.3, respectively. From these plots it can be seen that the distribution of error estimates for all estimators is generally in good agreement with the true error distribution except for deviations along SCs and in "interference"-like regions. In

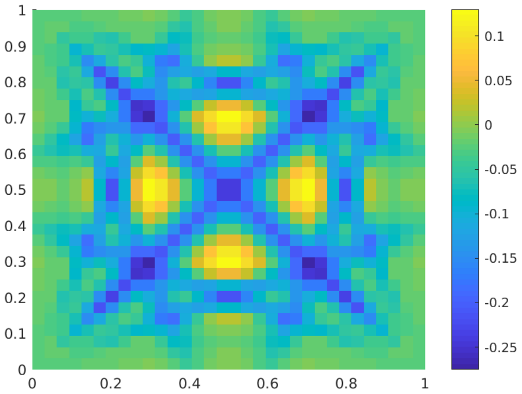

Figure 6.1 $\log_{10}\theta_{ang.}^{(i,j)}$ for LeR/TE-AD Estimator, H^1 Case 1, $N_X = N_Y = 32$

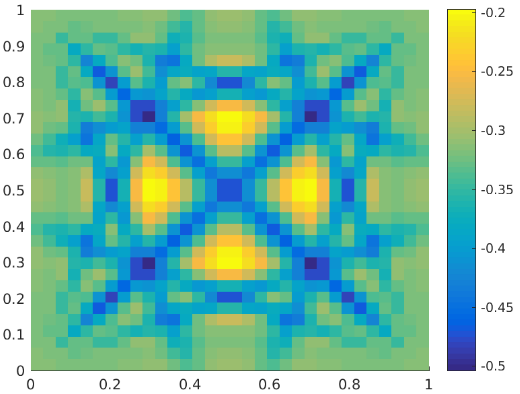

Figure 6.2 $\log_{10}\theta_{ang.}^{(i,j)}$ for RW Estimator, H^1 Case 1, $N_X = N_Y = 32$

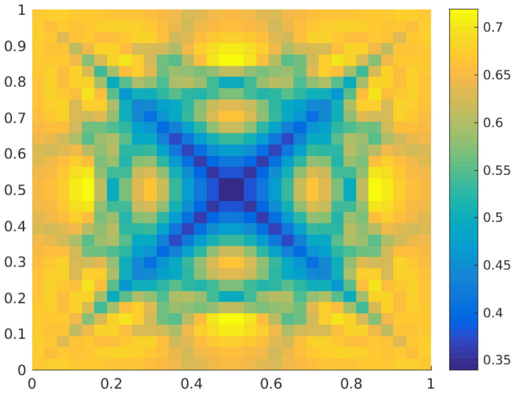

Figure 6.3 $\log_{10}\theta_{ang.}^{(i,j)}$ for DAZ Indicator, H^1 Case 1, $N_X = N_Y = 32$

terms of accuracy, the LeR/TE-AD estimator is the only estimate that sees agreement with the true error, i.e., $\log_{10}\theta_{ang.}^{(i,j)}$ is close to 0. The DAZ indicator is the least accurate estimator, but it achieves a local bound for this case as all the local error estimate values are overestimates.

Next we look at the results plotted in histogram form for these three estimator/indicators, Figures 6.4-6.6, respectively. The LeR/TE-AD estimator is centered about exact agreement, while the RW estimator has the expected level of bias (p for an H^1 problem with DGFEM-0 is 1, giving a predicted bias of $\theta = 0.5$, or $\log_{10}\theta = -0.3$). Nevertheless, the RW estimator gives a good shape function (estimate of the error relative to mean estimated error, i.e., low variance), as its width in $\log_{10}$-scale is 0.3 versus 0.4 for LeR/TE-AD or 0.35 for DAZ. Also, generally, the absolute difference between the estimated and true error is only small where the effectivity is closest to zero. That means no estimators are subject to the potential issue of extremely low true errors magnifying the effectivity.

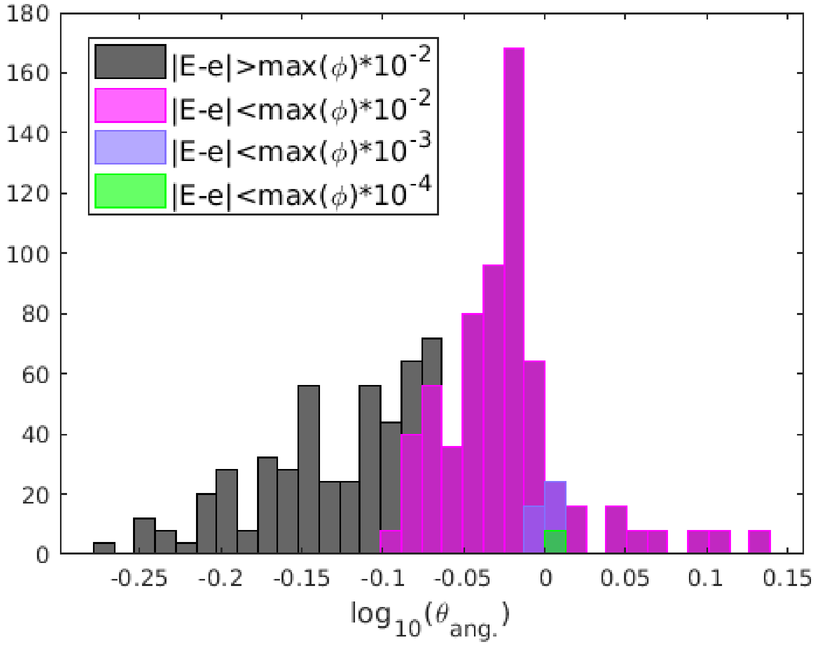

Figure 6.4 $\log_{10}\theta^{(i,j)}_{ang.}$ Histogram for LeR/TE-AD Estimator, H^1 Case 1, $N_X = N_Y = 32$

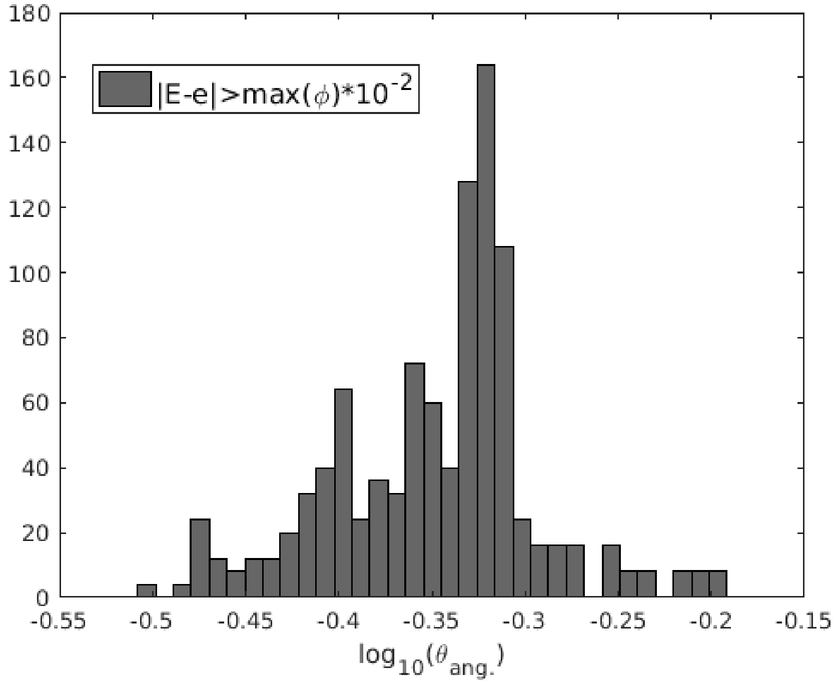

Figure 6.5 $\log_{10}\theta^{(i,j)}_{ang.}$ Histogram for RW Estimator, H^1 Case 1, $N_X = N_Y = 32$

Figures 6.7 and 6.8 show the scalar LeR/TE-AD and RW estimators, respectively, plotted over the domain. Generally the trends of the angular estimators are mirrored in the scalar

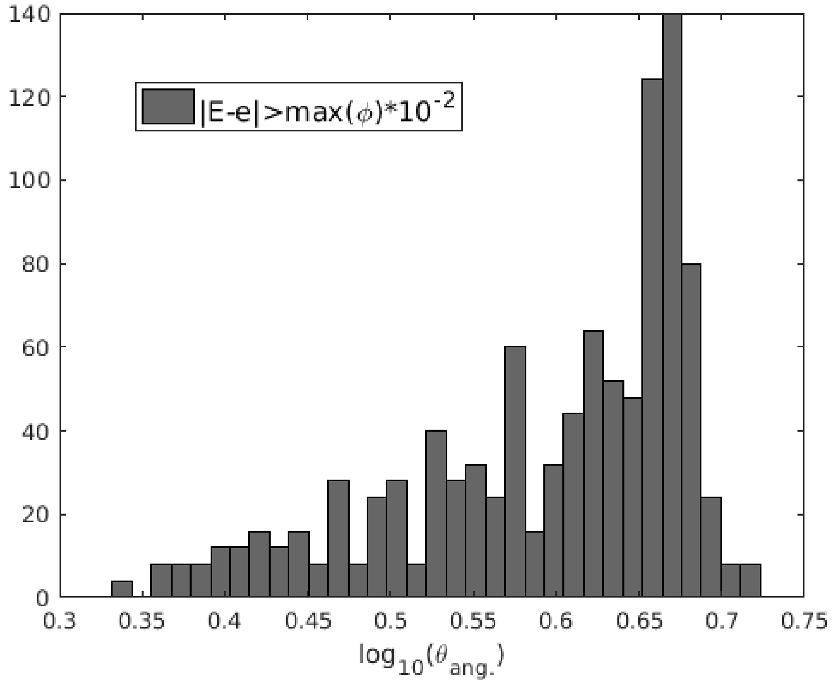

Figure 6.6 $\log_{10} \theta^{(i,j)}_{ang.}$ Histogram for DAZ Indicator, H^1 Case 1, $N_X = N_Y = 32$

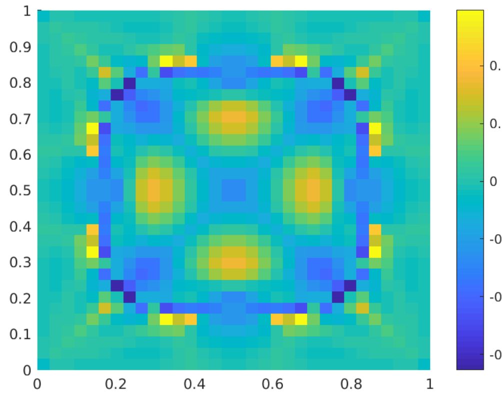

Figure 6.7 $\log_{10} \theta^{(i,j)}_{sca.}$ for LeR/TE-AD Estimator, H^1 Case 1, $N_X = N_Y = 32$

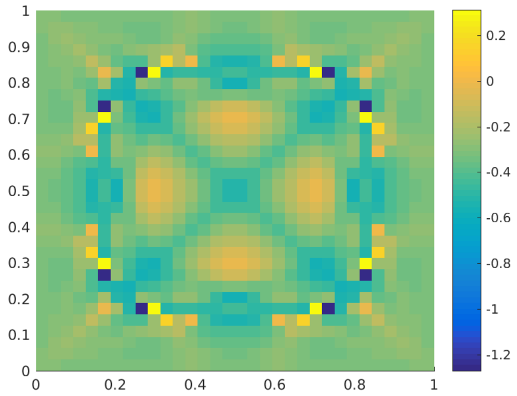

Figure 6.8 $\log_{10} \theta^{(i,j)}_{sca.}$ for RW Estimator, H^1 Case 1, $N_X = N_Y = 32$

estimators, such as under-estimation of the peak in the case of RW. From histograms of the same two estimators, Figures 6.9 and 6.10, respectively, it can be seen that the price paid for a reduction in memory storage requirements in the scalar norms is a worse representation of the error. One potential advantage of the RW estimator is that it does not require modification of existing codes to generate a scalar error estimate. The LeR/TE-AD estimator requires angular quantities to build a residual, and the DAZ estimator needs angular quantities to build a residual and the inter-element jumps, even if a scalar error estimate is desired. However, a

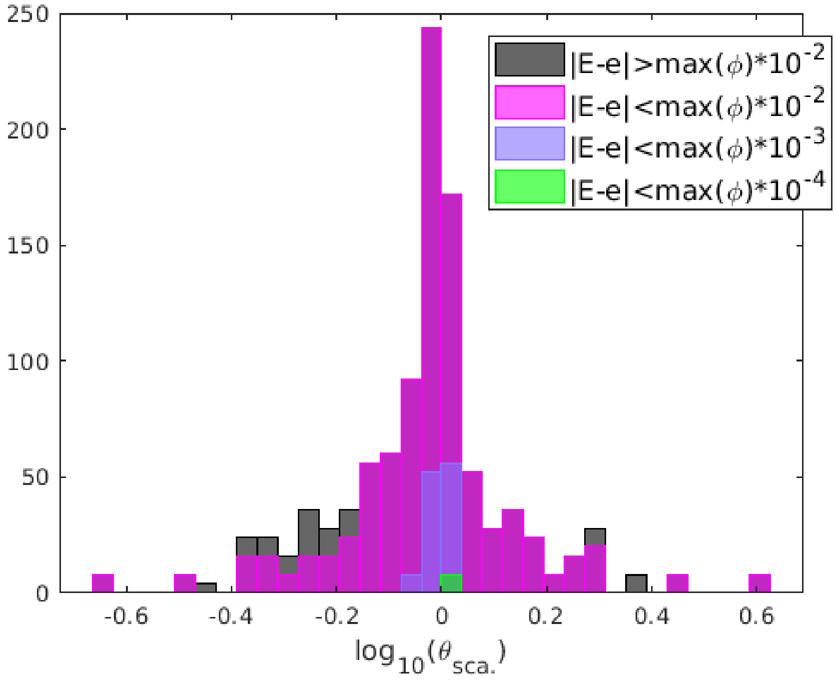

Figure 6.9 $\log_{10}\theta_{sca.}^{(i,j)}$ Histogram for LeR/TE-AD Estimator, H^1 Case 1, $N_X = N_Y = 32$

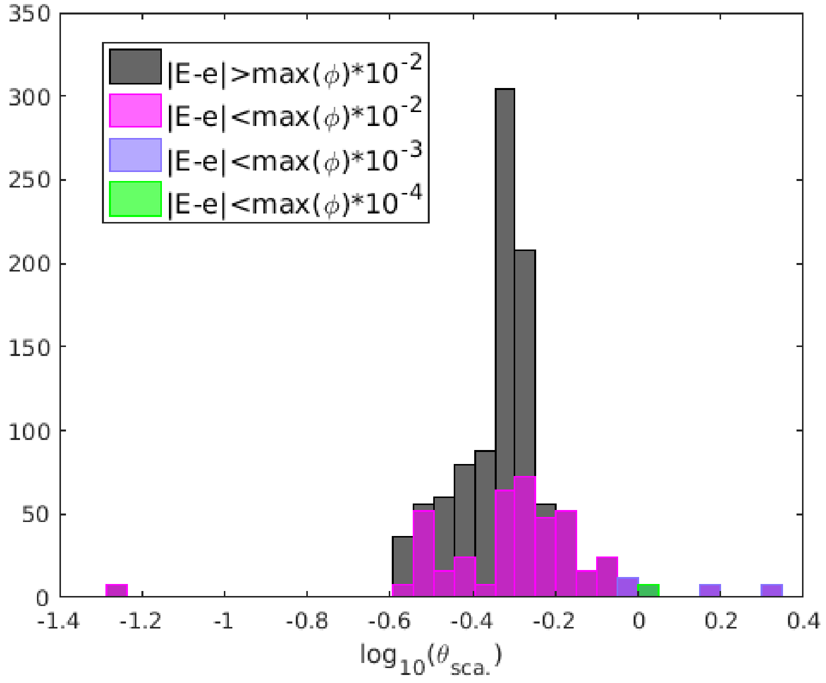

Figure 6.10 $\log_{10}\theta_{sca.}^{(i,j)}$ Histogram for RW Estimator, H^1 Case 1, $N_X = N_Y = 32$

scalar estimator has worse performance when compared to an angular estimator. Because this trend is consistent for all cases, only the angular local behavior will be reported from here on out for other H^1 problems, since this work is primarily interested in error estimator accuracy, which is captured best with angular estimators. However, scalar estimators are still valuable from a user's perspective, as they are easily relatable to error in scalar quantities such as scalar flux and reaction rates.

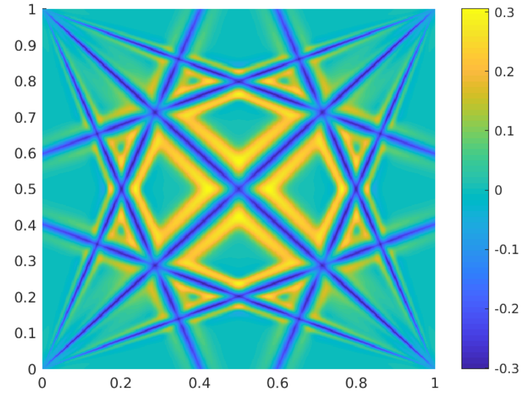

Figure 6.11 $\log_{10}\theta_{ang.}^{(i,j)}$ for LeR/TE-AD Estimator, H^1 Case 1, $N_X = N_Y = 512$

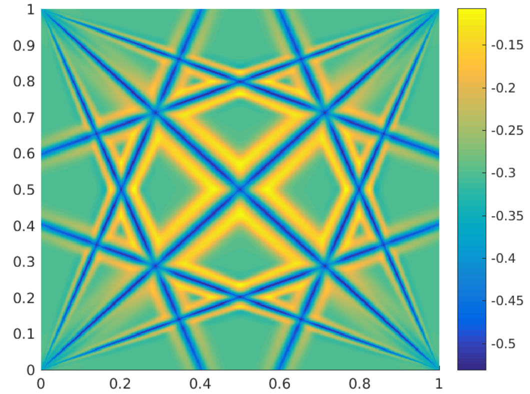

Figure 6.12 $\log_{10}\theta_{ang.}^{(i,j)}$ for RW Estimator, H^1 Case 1, $N_X = N_Y = 512$

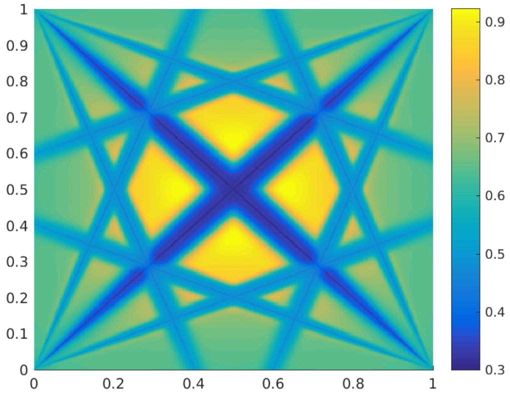

Figure 6.13 $\log_{10}\theta_{ang.}^{(i,j)}$ for DAZ Indicator, H^1 Case 1, $N_X = N_Y = 512$

Next, the same case ($\sigma_t = 1.0$, $c = 0.9$) is refined to $N_X = N_Y = 512$, and the angular effectivities for all three estimators, Figures 6.11-6.13, respectively, are plotted over the domain. The features seen in the coarser mesh case are seen again here, although both estimators have much better shape functions in the "interference-like" region in the center of the domain, likely because numerical spreading of error from the SCs has subsided due to the greater number of cells in these regions.

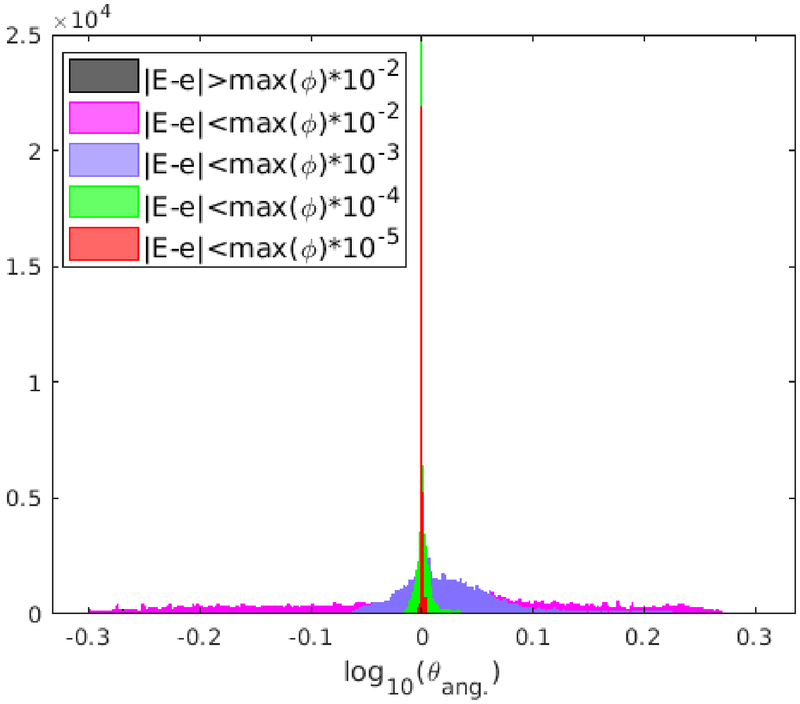

Figure 6.14 $\log_{10}\theta^{(i,j)}_{ang.}$ Histogram for LeR/TE-AD Estimator, H^1 Case 1, $N_X = N_Y = 512$

The histograms are plotted, Figures 6.14-6.16. These plots exemplify the quality of the RW estimator as a shape estimator, as the variance about the peak at the biased value is extremely small. Also note that the RW estimator has a greater peak height than the LeR/TE-AD estimator ($\sim 3\times10^4$ *vs.* $\sim 2.5\times10^4$, respectively) and narrower $\log_{10}$-scale minimum-to-maximum effectivity range (~ 0.4 *vs.* ~ 0.6, respectively) as indicators of a superior shape function. With this problem and mesh, the majority of cells are in the asymptotic convergence regime with respect to cell size. While not good as the RW estimator, the LeR/TE-AD estimator is also excellent as a shape estimator, and it has the added benefit of being centered about exact agreement with the true error. Because it is centered about the exact error, it is also more cautious, which would be more useful from an error analysis standpoint. The DAZ indicator remains locally cautious for this case.

The scalar performance for $N_X = N_Y = 512$ is plotted for the LeR/TE-AD and RW estimators, Figures 6.17 and 6.18, respectively, over the domain. The finer details are diluted by the large orders of magnitude spread by the scalar estimators, but the severe departure from

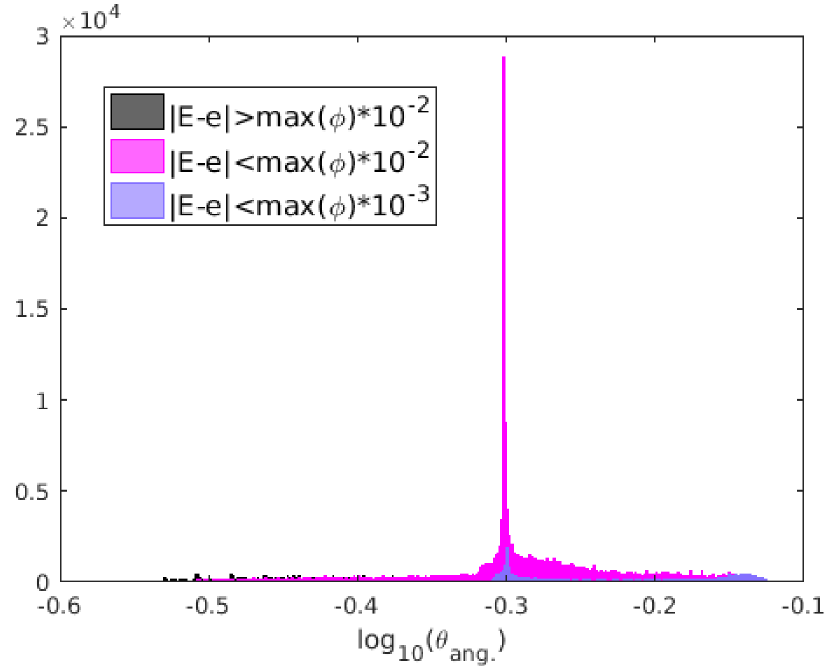

Figure 6.15 $\log_{10}\theta_{ang.}^{(i,j)}$ Histogram for RW Estimator, H^1 Case 1, $N_X = N_Y = 512$

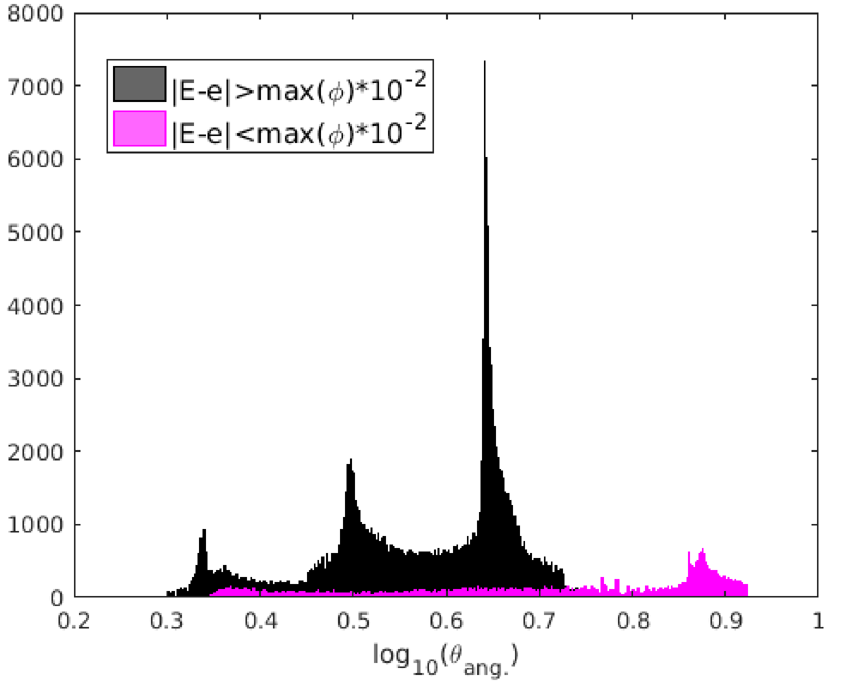

Figure 6.16 $\log_{10}\theta_{ang.}^{(i,j)}$ Histogram for DAZ Indicator, H^1 Case 1, $N_X = N_Y = 512$

near-exact agreement is focused near the SCs.

The scalar estimator histograms are shown in Figures 6.19 and 6.20. We observe that apart

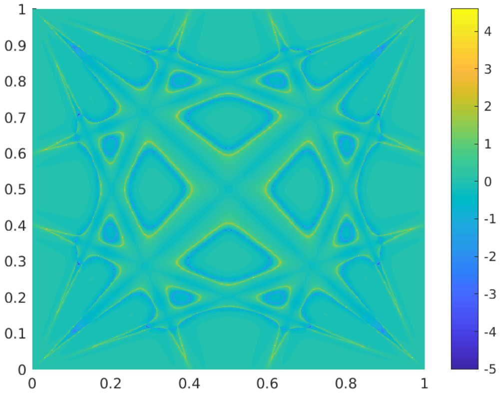

Figure 6.17 $\log_{10} \theta_{sca.}^{(i,j)}$ for LeR/TE-AD Estimator, H^1 Case 1, $N_X = N_Y = 512$

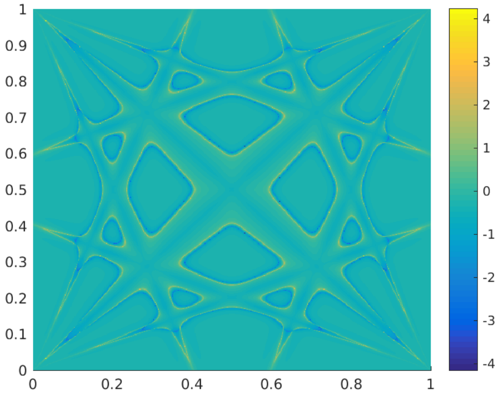

Figure 6.18 $\log_{10} \theta_{sca.}^{(i,j)}$ for RW Estimator, H^1 Case 1, $N_X = N_Y = 512$

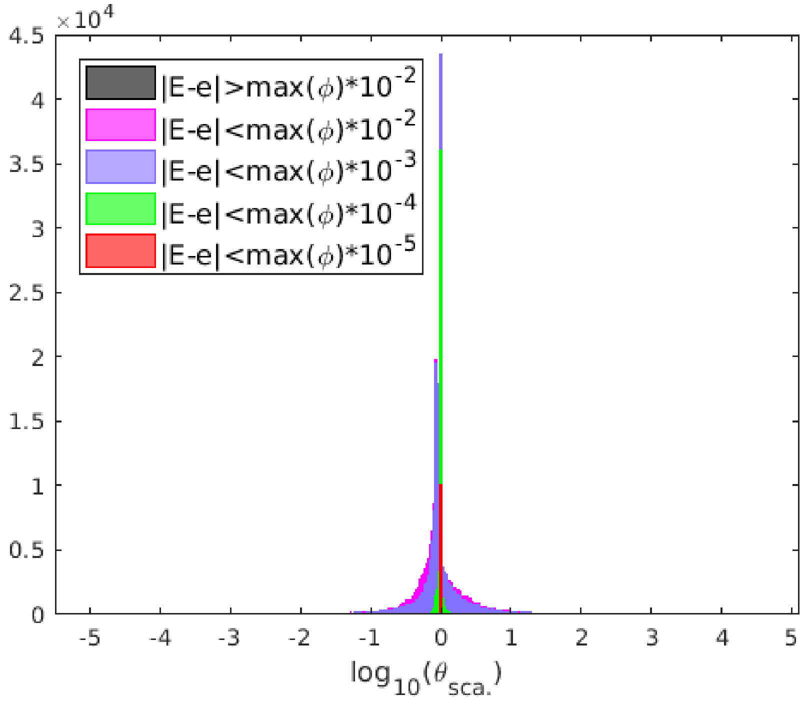

Figure 6.19 $\log_{10} \theta_{sca.}^{(i,j)}$ Histogram for LeR/TE-AD Estimator, H^1 Case 1, $N_X = N_Y = 512$

from the large over and underestimation of comparatively very few cells, the scalar estimators are similar to the angular estimators in accuracy, although the effectivities are not consolidated in as small a range as the angular estimator effectivities (i.e., peak is wider). Again, the LeR/TE-AD estimator is centered at exact agreement, while the RW estimator is biased to underestimate the error.

Now the global error norm with decreasing cell size is examined, as one of the chief reported advantages of the DAZ estimator is providing an upper bound in the global norm [18]. The

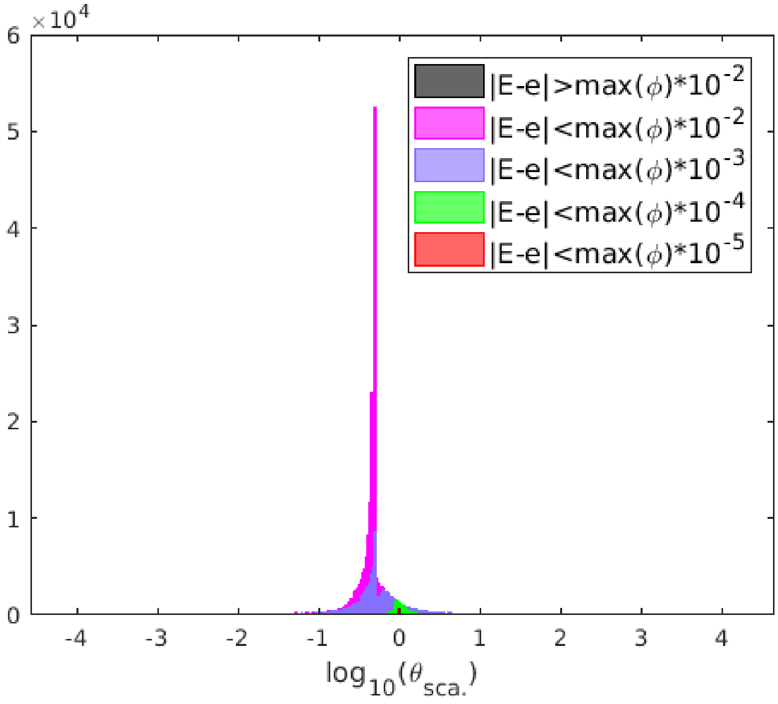

Figure 6.20 $\log_{10}\theta^{(i,j)}_{sca.}$ Histogram for RW Estimator, H^1 Case 1, $N_X = N_Y = 512$

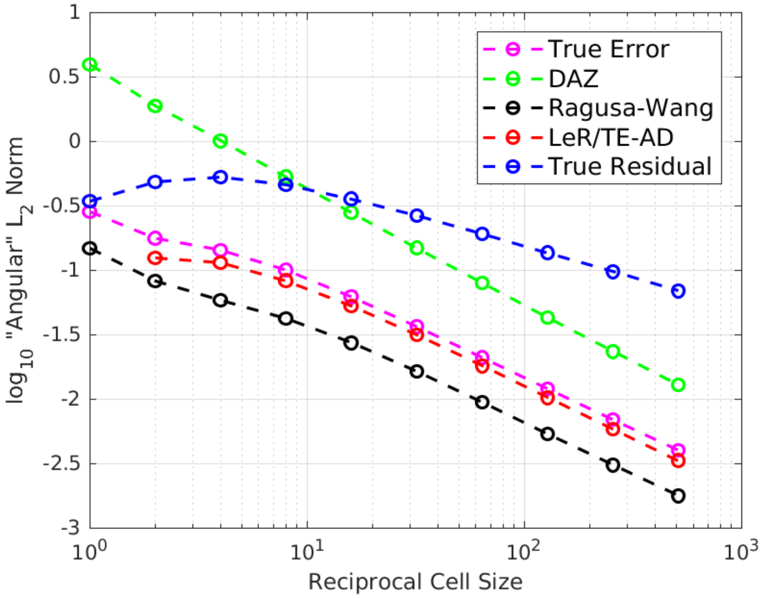

Figure 6.21 Angular Error/Estimator L_2 Norm Convergence for H^1 Case 1

angular error and estimates are plotted in Figure 6.21 while the angular effectivity indices are plotted in Figure 6.22. One can see that the DAZ estimator bounds the true error in this case, in agreement with the theory. The global norm of the RW estimator underestimates with a global

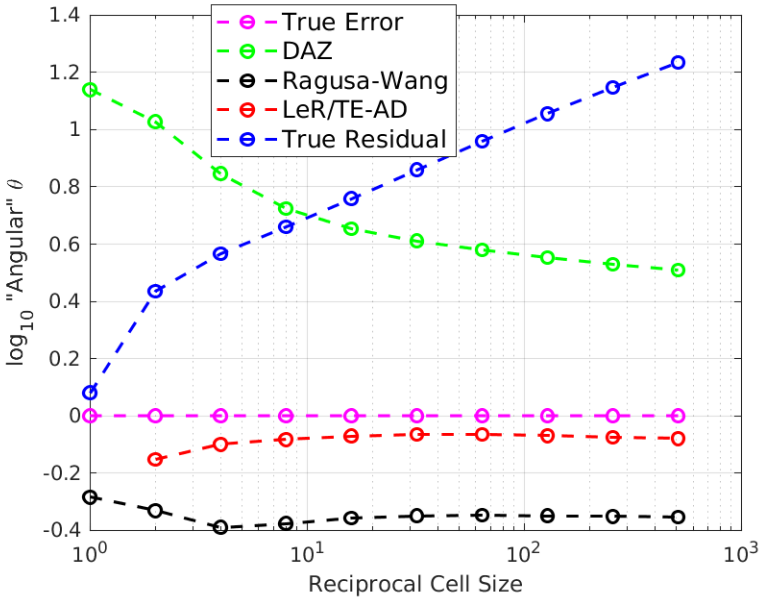

Figure 6.22 Angular Effectivity Convergence for H^1 Case 1

norm close to $\log_{10}\theta_{ang.} = -0.3$. For this case, in terms of global effectivities, the LeR/TE-AD estimator is closest to the true error for all meshes but the trivial $N_X = N_Y = 1$ mesh. The true residual is plotted with the other estimates because we are interested in the possibility of using an approximated residual as a computationally cheap error bound, since it is already calculated on-the-way to an LeR/TE-AD estimate. Intuitively, based on traditional stability arguments for numerical methods, it is believed that the residual should bound the error from above globally. Hence, in Figure 6.22, we confirm that the true residual bounds the true error from above, though the lower convergence order with respect to the true error convergence order is also verified. Since we are interested in using the DAZ estimator as a bound, we extend the mesh refinement of the DAZ plot to smaller mesh sizes, Figure 6.23, and note that even at finer meshes the DAZ estimator bounds the true error from above. While further mesh refinement would be of interest, it is worth noting that, in addition to the computational burden of running even more refined meshes, eventually some error and estimator values would be expected to diminish to the same order as the iteration tolerance, making this a fruitless exercise.

The scalar error and estimates are plotted in Figure 6.24 while the scalar effectivity indices are plotted in Figure 6.25, with similar results to those in Figures 6.21 and 6.22. However, one interesting exception is that the true residual does not bound the true error for $N_X = N_Y = 2$. This would suggest that the angular norm is required for the residual to bound the error. However, after asymptotic convergence with mesh refinement is reached, the scalar norm appears to converge with the same order as the angular norm, Figure 6.21. Like the angular versions, the LeR/TE-AD estimator is most accurate among the three compared estimators, and the RW estimator converges to a value close to $\log_{10}\theta_{sca.} = -0.3$.

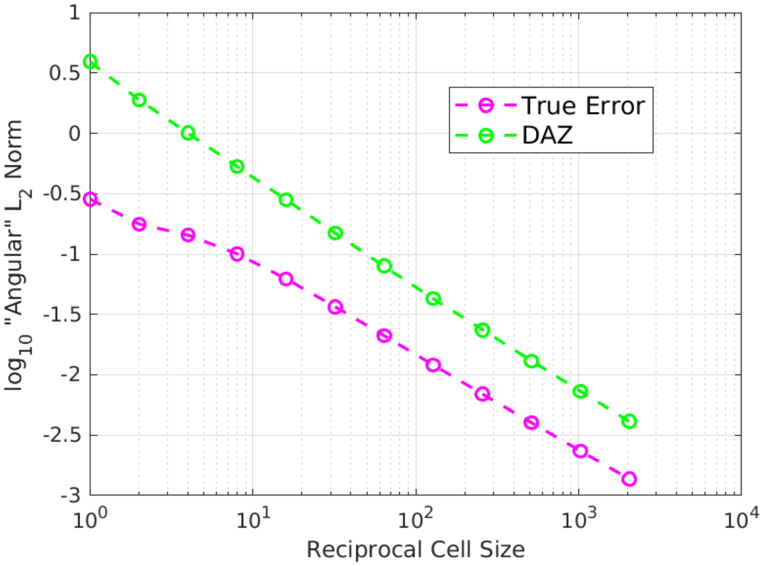

Figure 6.23 Angular Error/DAZ Estimator Global L_2 Norm Convergence for H^1 Case 1

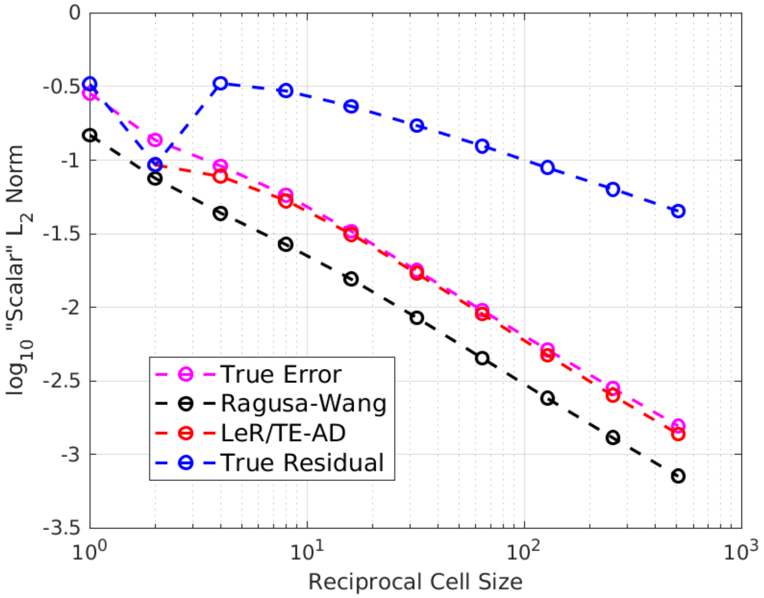

Figure 6.24 Scalar Error/Estimator Convergence for H^1 Case 1

Next, the computational cost for the estimators is plotted for the angular and scalar estimators in Figures 6.26 and 6.27, respectively, with the cost of the discrete transport solution also plotted as a reference. The computation times are calculated in the following ways. The discrete solution time is the net time for the deterministic transport code to execute (read input, solution algorithm, and write output times). The TE-AD residual time is the net time for the residual to be calculated plus the time it takes to calculate the norms of the residual. The

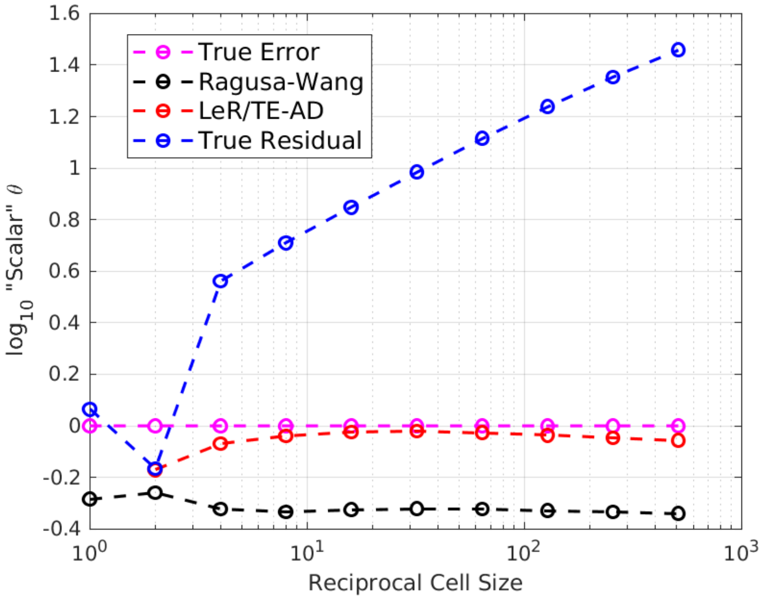

Figure 6.25 Scalar Effectivity Convergence for H^1 Case 1

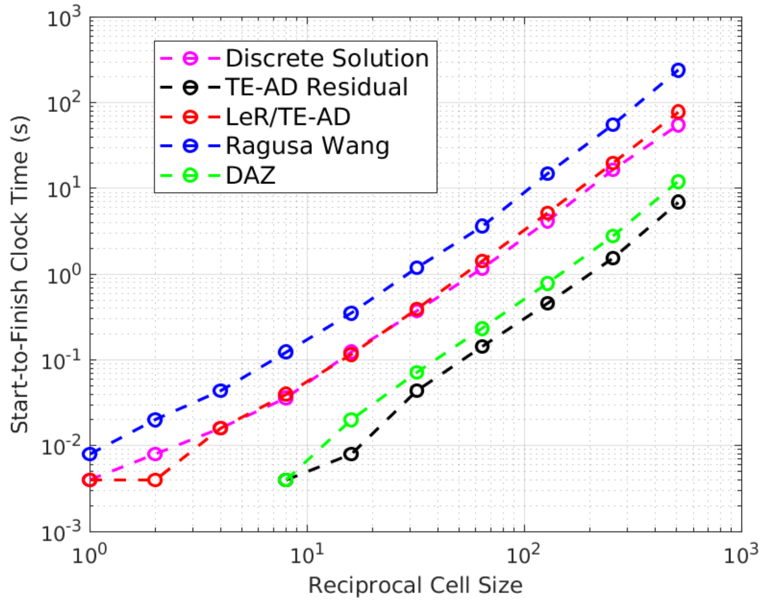

Figure 6.26 Computation Time for Angular Estimators, H^1 Case 1

LeR/TE-AD time is the net time to calculate the residual, run the deterministic transport code to solve for the error, and compress the error into error norms. The RW time is the net time to project the h-mesh solution onto the $h/2$-mesh, run the deterministic transport code to solve for the $h/2$-solution, and calculate the RW estimate in terms of the output norms. The DAZ indicator/estimator is calculated in one process, which is the input of the transport solution,

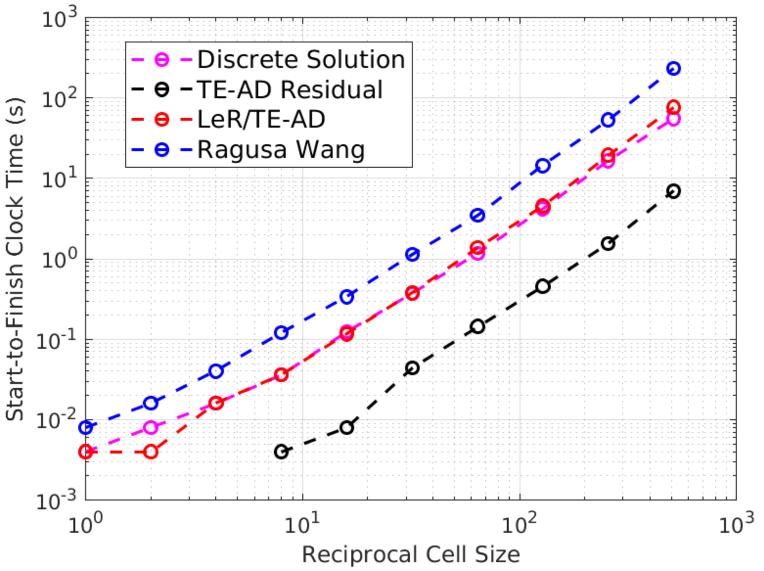

Figure 6.27 Computation Time for Scalar Estimators, H^1 Case 1

the single higher-order sweep, and the calculation and output of the estimate.

One important comparison between the angular and scalar estimators is that there is nearly no computational time difference between the two types of estimators. This is because the time difference between scalar and angular estimators will only be manifest in the post-processing routines which, relative to the cost of solving the transport equation, are small. Thus, the only benefit to using a scalar estimator over an angular estimator, in terms of computational cost, is that the data structure required to calculate a scalar estimator will be smaller, although there are certainly other benefits unrelated to computational cost that have been mentioned previously in Section 2.4. With regards to the relative cost of the estimators versus each other, we notice that, as predicted, the TE-AD residual approximation as an indicator and DAZ indicator/estimator are far cheaper, an order of magnitude or more, than the RW and LeR/TE-AD estimators because they do not require an additional, multi-iteration transport solve. The DAZ indicator/estimator's cost will vary depending on the additional order 'l' added to calculate the HOPS, and its cost should be on the order of the execution time of a single sweep for the low order problem times a factor of $\frac{(\Lambda+l+1)^2}{(\Lambda+1)^2}$ plus the additional time for calculating the estimate based on the HOPS. As expected, the LeR/TE-AD estimator calculation time is similar to that of calculating the original discrete solution, although the additional computation time required to calculate the residual and do the post-processing accounts for the slightly greater time when compared to the discrete solution. The RW estimator is about three times more expensive than the LeR/TE-AD estimator. While the solution time for the $h/2$-mesh solution will be roughly four times longer (minus the time saved by preconditioning with the h-mesh solution) than the solution time on the h-mesh, the input and output times of the code plus the pre- and post-processing times of the error estimation reduces the relative net time for computation to less than four. Because the computation times have a predictable behavior (i.e., linearly scaling with number of cells and number of iterations), computation time results will be omitted for case-by-case problems for the remaining sections. However, note that one can expect transport solution time to dominate and raise the estimator and discrete solution computation times (for estimators that require transport solves) as $c \to 1$, since a high scattering ratio will increase the number of iterations required to achieve convergence.

6.1.2 H^1 Case 2

The next H^1 case has large optical thickness ($\sigma_t = 10.0$) and a high scattering ratio $c = 0.9$. This is a case where the true solution's large gradients may affect the local behavior of the LeR/TE-AD estimator (recall this estimator uses Taylor Expansions as approximations of derivatives). A course $N_X = N_Y = 32$ mesh is applied.

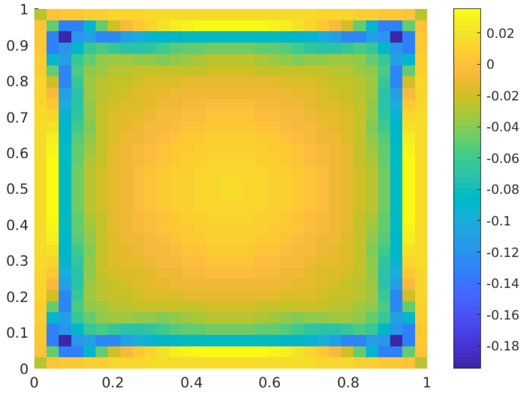

Figure 6.28 $\log_{10} \theta^{(i,j)}_{ang.}$ for LeR/TE-AD Estimator, H^1 Case 2, $N_X = N_Y = 32$

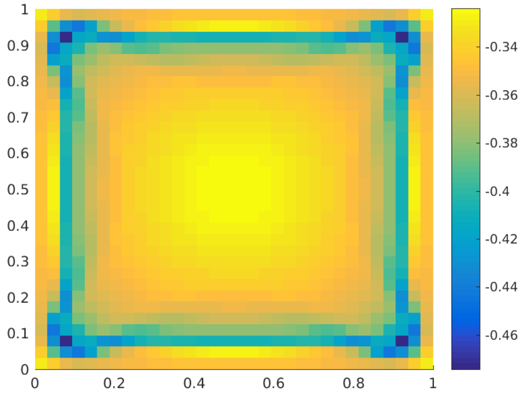

Figure 6.29 $\log_{10} \theta^{(i,j)}_{ang.}$ for RW Estimator, H^1 Case 2, $N_X = N_Y = 32$

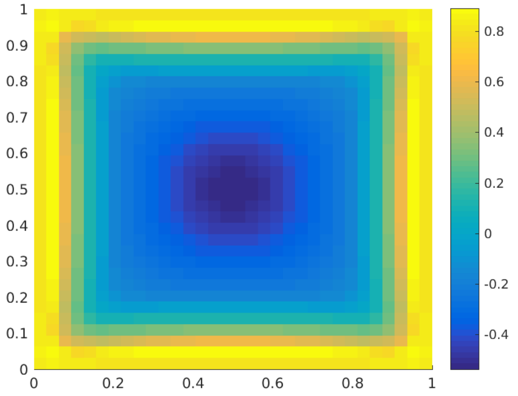

Figure 6.30 $\log_{10} \theta^{(i,j)}_{ang.}$ for DAZ Indicator, H^1 Case 2, $N_X = N_Y = 32$

A comparison of the local angular effectivities plotted is over the domain, Figures 6.28-6.30. In the LeR/TE-AD and RW estimator plots the tell-tale signs of a large optical thickness can be seen, namely poor representation of the error on cells near the boundary. This is due to the inability of DGFEM-0 to accurately approximate derivatives, which makes the RW estimator and TE-AD approximation (thus the LeR/TE-AD estimate) less effective. This behavior is not seen for the DAZ indicator, which progressively underestimates the error in cells closer to the domain center.

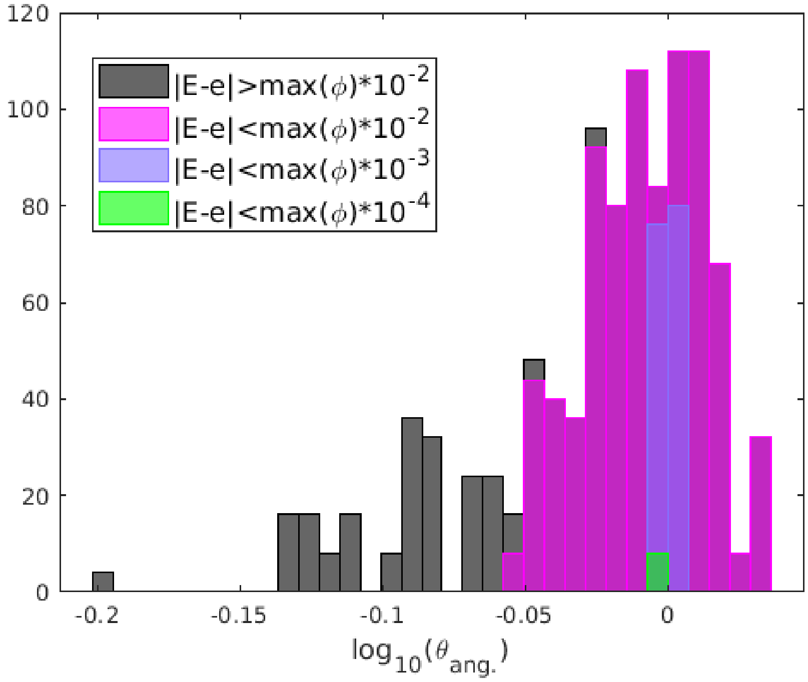

Figure 6.31 $\log_{10}\theta_{ang.}^{(i,j)}$ Histogram for LeR/TE-AD Estimator, H^1 Case 2, $N_X = N_Y = 32$

The histograms for the three estimators, Figures 6.31-6.33, give an understanding of where the effectivities coalesce. The histograms show that the LeR/TE-AD and RW estimators serve excellently as shape estimators for this case with a large number of effectivities being contained within a narrow band, although the RW has the predicted bias towards underestimating the true error. The local DAZ indicator has a very wide bound and is not as locally cautious as the other two estimators in terms of the lowest value of underestimation.

The estimator behavior is plotted in the domain for a fine $N_X = N_Y = 512$ mesh in Figures 6.34-6.36, and the effectivity histograms for this refined mesh are plotted in Figures **??**-6.39. The results on the fine mesh are similar to those on the coarse mesh, Figures 6.28-6.33. The LeR/TE-AD estimator becomes slightly more accurate in terms of the standard deviation of $\log_{10}\theta_{ang.}^{(i,j)}$ as the mesh is refined, although as before it is seen that the minimum-to-maximum width of $\log_{10}\theta_{ang.}^{(i,j)}$ increases as the mesh is refined. In this case the LeR/TE-AD and RW estimators are about equivalent as shape estimates in terms of peak height and maximum-

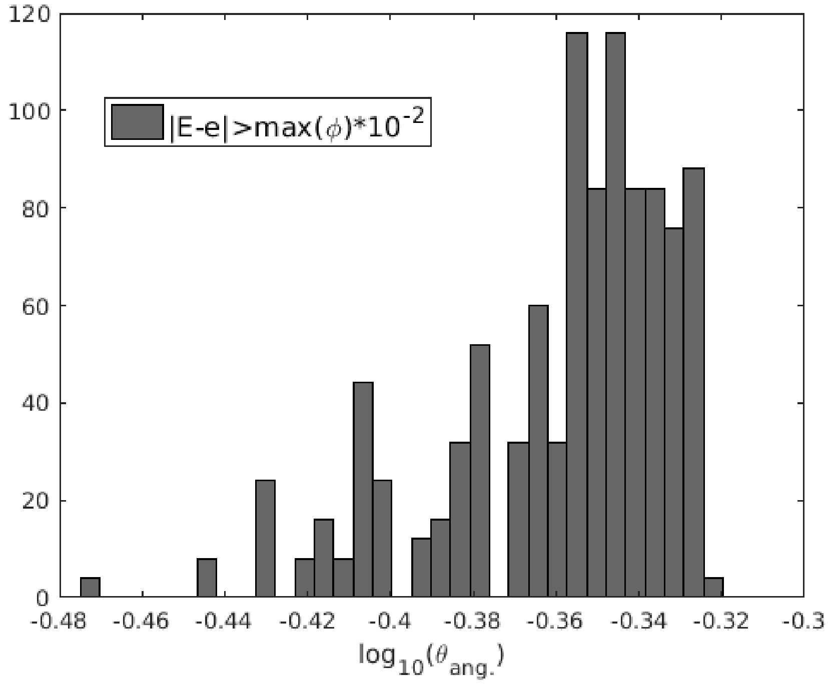

Figure 6.32 $\log_{10} \theta_{ang.}^{(i,j)}$ Histogram for RW Estimator, H^1 Case 2, $N_X = N_Y = 32$

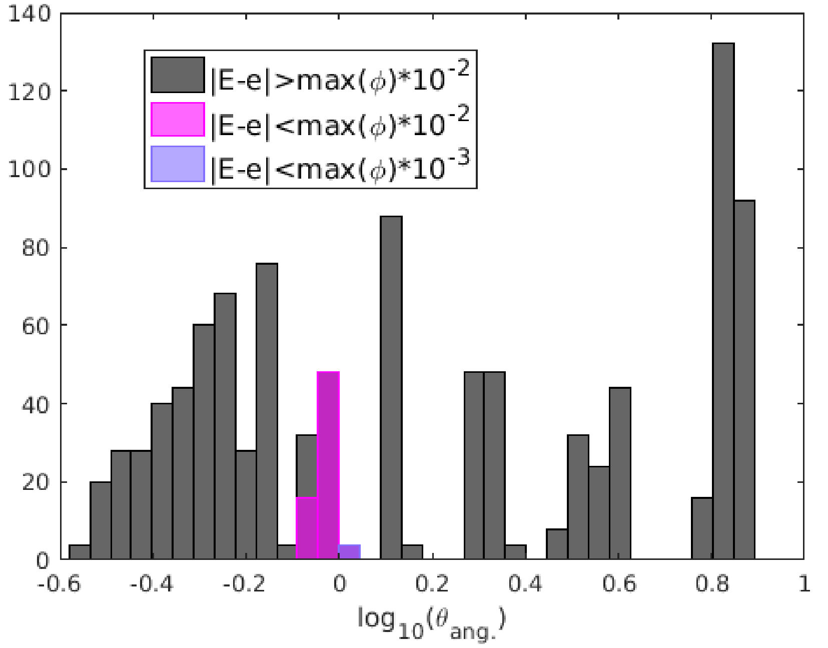

Figure 6.33 $\log_{10} \theta_{ang.}^{(i,j)}$ Histogram for DAZ Indicator, H^1 Case 2, $N_X = N_Y = 32$

to-minimum $\log_{10}$-scale effectivity range, but the LeR/TE-AD estimator has the advantage of being accurate. Note that as the mesh is refined two separate peaks become apparent in the DAZ

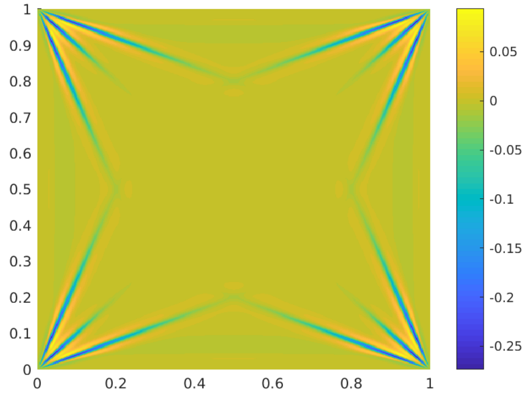

Figure 6.34 $\log_{10}\theta_{ang.}^{(i,j)}$ for LeR/TE-AD Estimator, H^1 Case 2, $N_X = N_Y = 512$

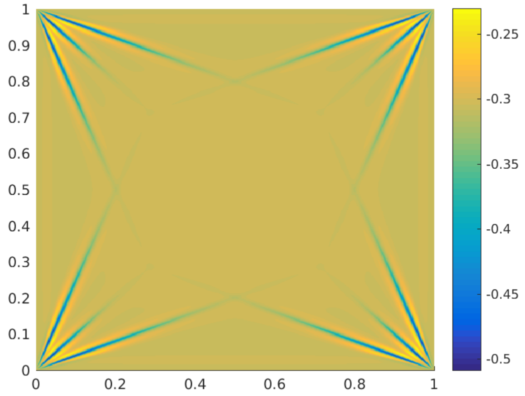

Figure 6.35 $\log_{10}\theta_{ang.}^{(i,j)}$ for RW Estimator, H^1 Case 2, $N_X = N_Y = 512$

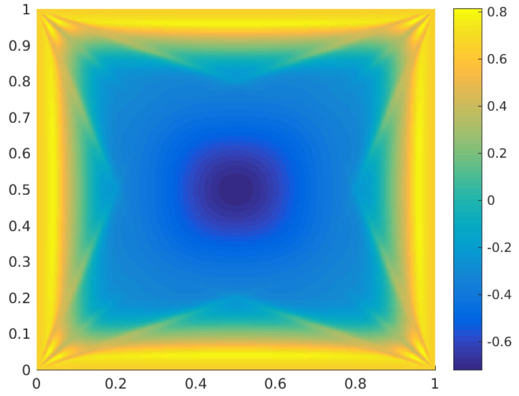

Figure 6.36 $\log_{10}\theta_{ang.}^{(i,j)}$ for DAZ Indicator, H^1 Case 2, $N_X = N_Y = 512$

indicator, Figure 6.39. The underestimation peak appears to be associated with cells inward in the domain, while the overestimation peak is associated with cells near the problem boundary. We note that for a problem with large optical thickness and scattering ratio, the single-sweep HOPS will be a poor representation of a fully converged higher-order solution, though this is not known to be related to the effect seen here.

Figures 6.40 and 6.41 show that the global LeR/TE-AD estimator is more accurate than the RW estimator, although it still is not cautious, unlike the DAZ estimator, which is not cautious locally in this case. Given the possibility of using the predicted bias to "correct" the RW estimator, it can be seen that in this optically thick case, the RW estimator does not reach its $\log_{10}\theta_{ang.} = -0.3$ bias until the mesh is refined to about $N_X = N_Y = 32$, the mesh at which the true solution has approached asymptotic convergence with respect to mesh refinement. It is noted that the residual in the angular norm bounds the true error, while in the scalar norm,

Figure 6.42, it does not, although again this happens only in the $N_X = N_Y = 2$ case.

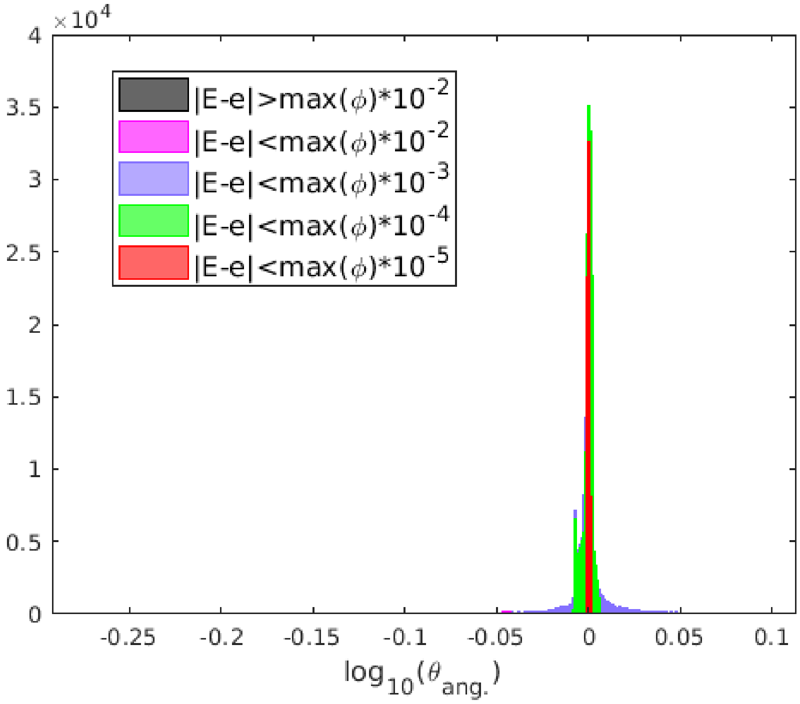

Figure 6.37 $\log_{10} \theta^{(i,j)}_{ang.}$ Histogram for LeR/TE-AD Estimator, H^1 Case 2, $N_X = N_Y = 512$

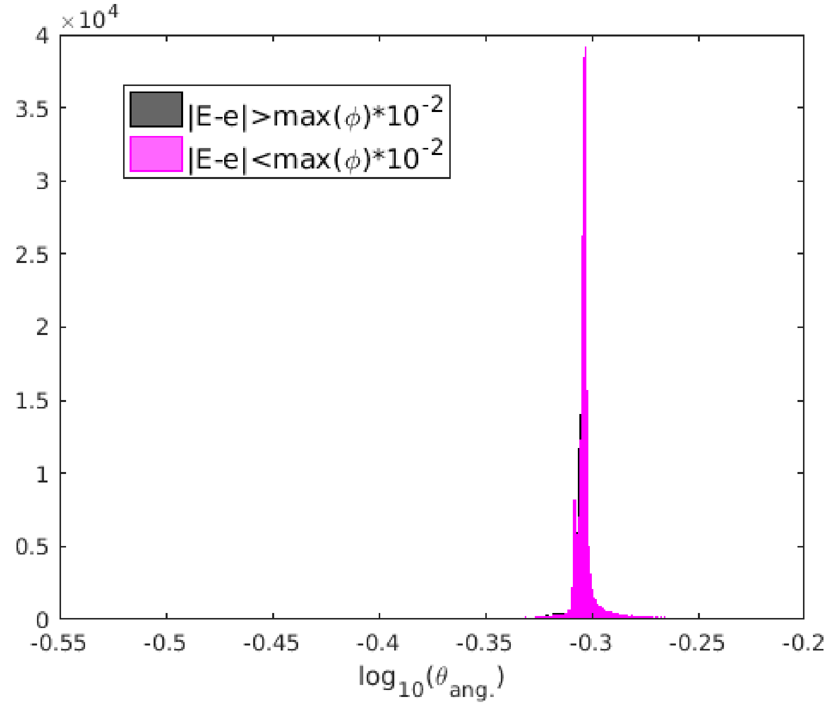

Figure 6.38 $\log_{10}\theta^{(i,j)}_{ang.}$ Histogram for RW Estimator, H^1 Case 2, $N_X = N_Y = 512$

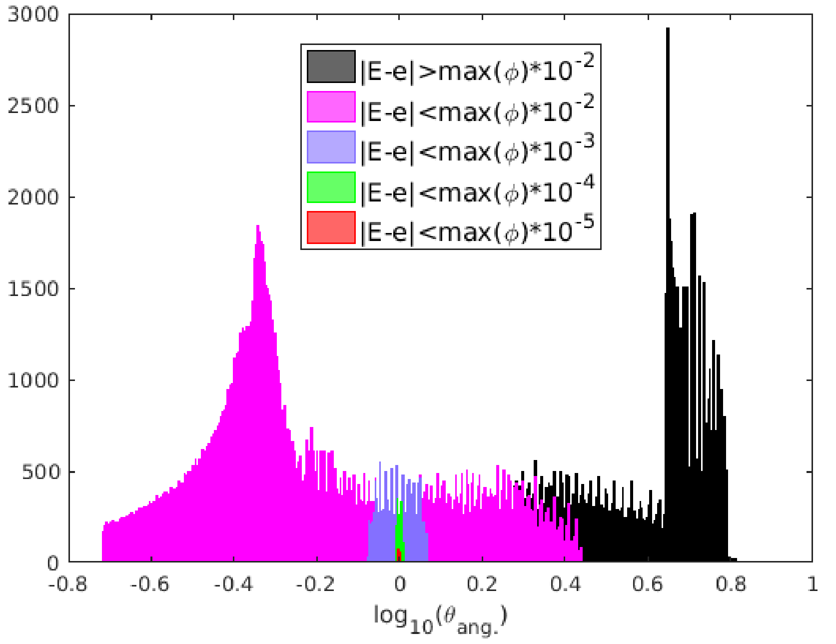

Figure 6.39 $\log_{10}\theta^{(i,j)}_{ang.}$ Histogram for DAZ Indicator, H^1 Case 2, $N_X = N_Y = 512$

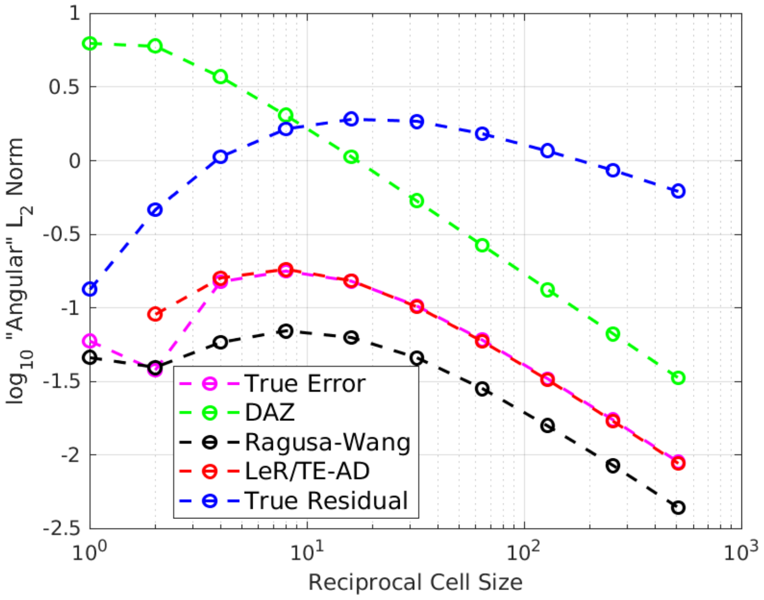

Figure 6.40 Angular Error/Estimator L_2 Norm Convergence for H^1 Case 2

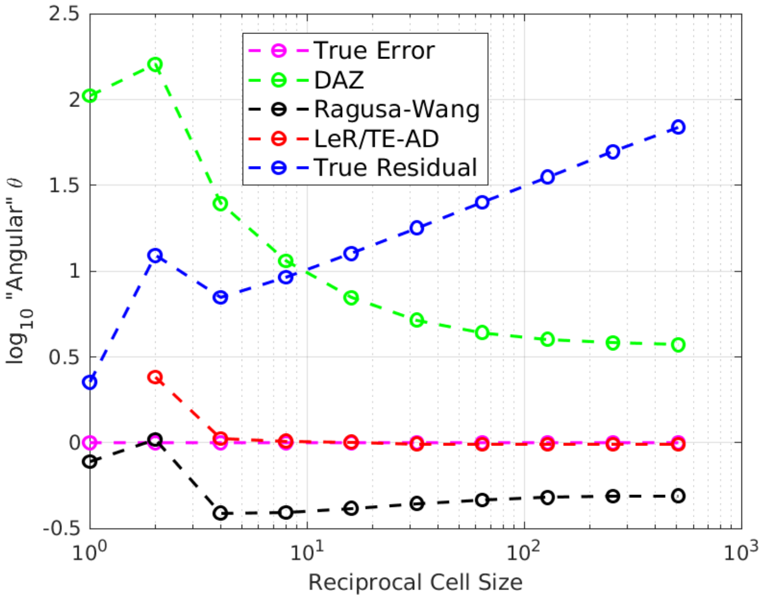

Figure 6.41 Angular Effectivity Convergence for H^1 Case 2

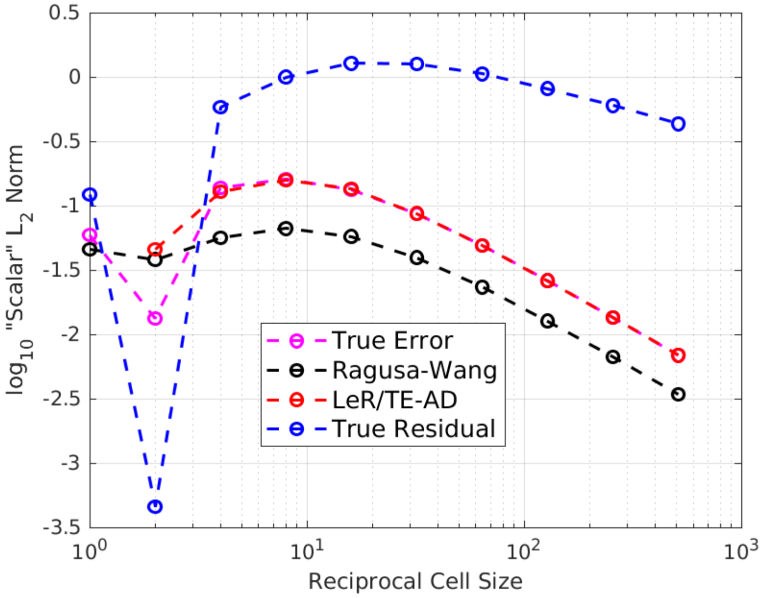

Figure 6.42 Scalar Error/Estimator L_2 Norm Convergence for H^1 Case 2

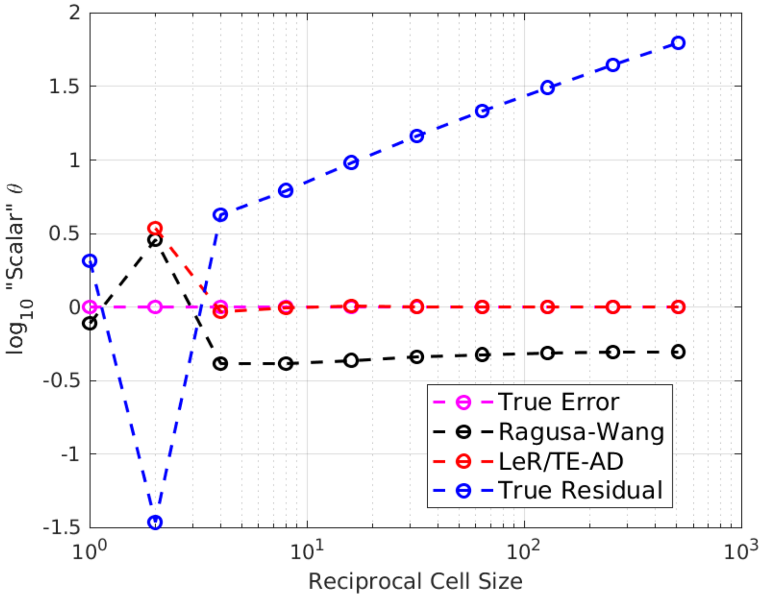

Figure 6.43 Scalar Effectivity Convergence for H^1 Case 2

6.1.3 H^1 Case 3

The last individual H^1 case considered has large optical thickness ($\sigma_t = 10.0$) and a low scattering ratio $c = 0.1$. A course $N_X = N_Y = 32$ mesh is applied to the domain.

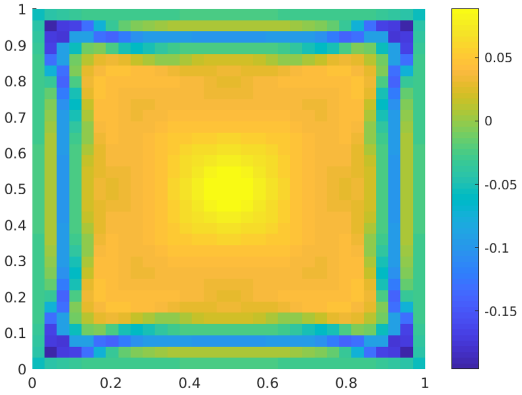

Figure 6.44 $\log_{10} \theta_{ang.}^{(i,j)}$ for LeR/TE-AD Estimator, H^1 Case 3, $N_X = N_Y = 32$

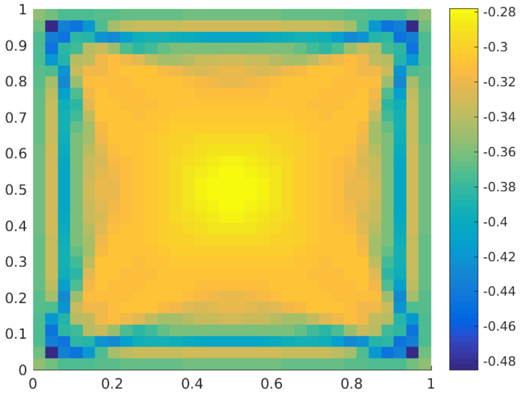

Figure 6.45 $\log_{10} \theta_{ang.}^{(i,j)}$ for RW Estimator, H^1 Case 3, $N_X = N_Y = 32$

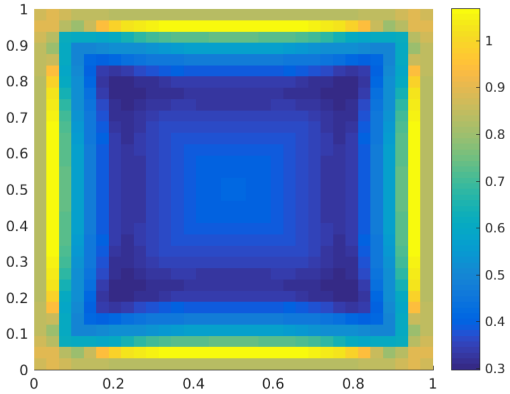

Figure 6.46 $\log_{10} \theta_{ang.}^{(i,j)}$ for DAZ Indicator, H^1 Case 3, $N_X = N_Y = 32$

We compare the angular effectivities plotted over the domain, Figures 6.44-6.46. Despite the large optical thickness, the RW and LeR/TE-AD estimators maintain their expected behavior, namely well-defined peaks that underestimate the true error norms in the case of RW but are accurate in the case of LeR/TE-AD. We do note that in Figure 6.44 the LeR/TE-AD estimator has more overestimated values than in the other two H^1 cases, Figures 6.1 and 6.28, though the exact cause of this is not known. In the section that follows it will be seen that for H^1 problems the LeR/TE-AD estimator generally becomes more cautious as optical thickness increases, although the scattering ratio also has a minimal effect. This is most likely a result of a small true error from an accurate DGFEM-0 solution due to the low gradients in the true solution. Effectivity values for the LeR/TE-AD estimator are contained in a small width about the exact error.

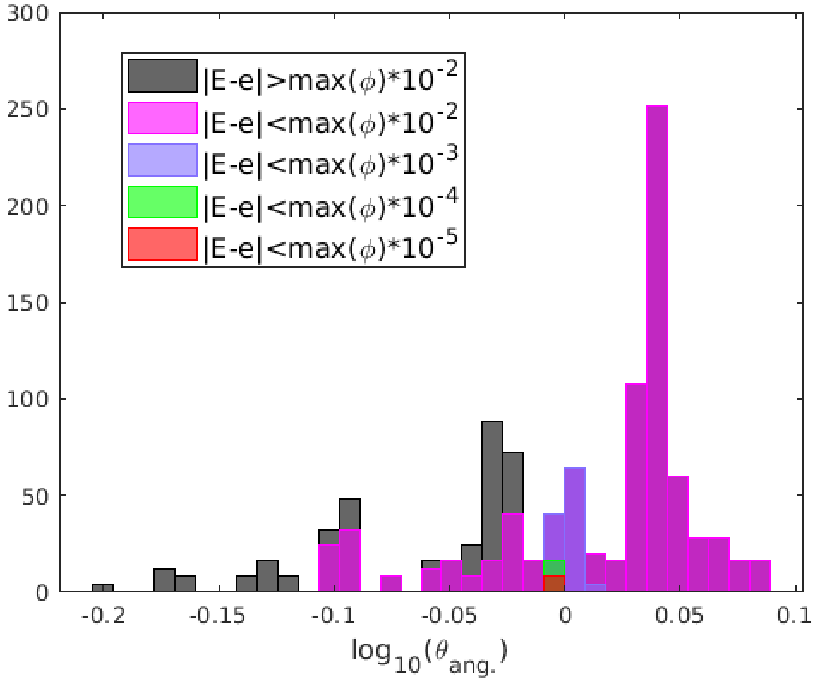

Figure 6.47 $\log_{10}\theta^{(i,j)}_{ang.}$ Histogram for LeR/TE-AD Estimator, H^1 Case 3, $N_X = N_Y = 32$

The histograms for the same cases, Figures 6.47-6.49, support the favorability of the LeR/TE-AD estimator for this case and show that the majority of effectivities are located around a very tight band about the perfect agreement value of $\log_{10}\theta^{(i,j)}_{ang.} = 0$.

The fine mesh domain plots and histograms, Figures 6.50-6.55, are similar to the previously shown results. The majority of effectivities for the LeR/TE-AD estimator are contained within $\left|\log_{10}\theta^{(i,j)}_{ang.}\right| \leq 0.05$, which corresponds to less than 13% deviation from the true error, although it can be seen that many of these values are contained within an even tighter bound. The RW estimator is contained in a tight band as well, but it remains victim to the predicted bias. The DAZ indicator is locally cautious, and it gives a large range of effectivities compared to the other two estimators.

Global effectivity convergence plots, Figures 6.56-6.59, are consistent with the behavior demonstrated in the previous two cases, namely that LeR/TE-AD is most accurate, RW has a predictable underestimation bias, and DAZ bounds from above. However, it is noted that the

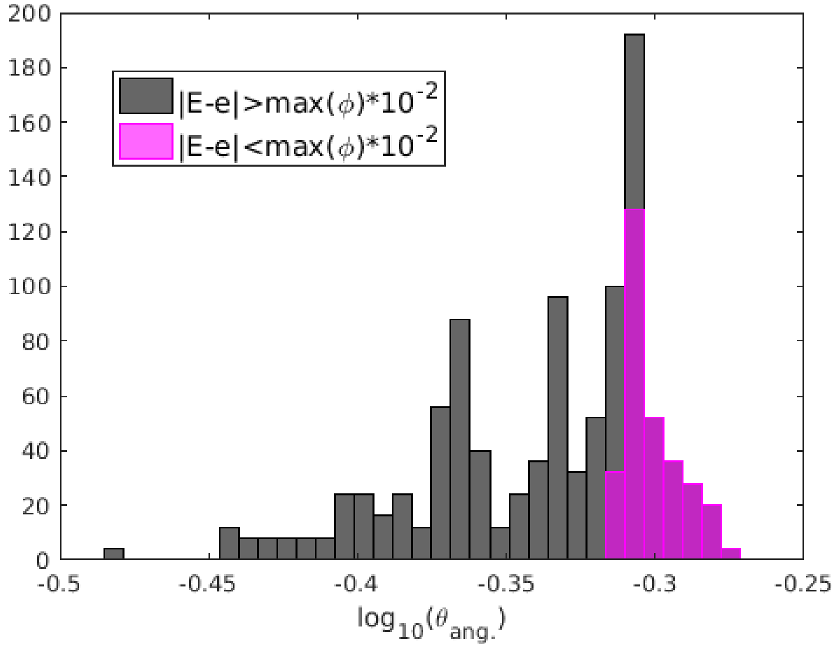

Figure 6.48 $\log_{10}\theta_{ang.}^{(i,j)}$ Histogram for RW Estimator, H^1 Case 3, $N_X = N_Y = 32$

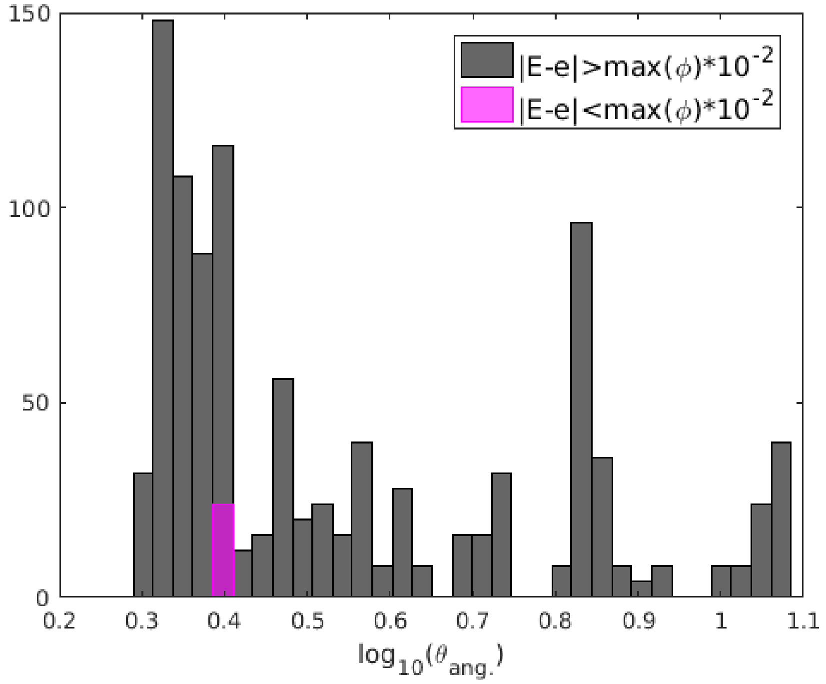

Figure 6.49 $\log_{10}\theta_{ang.}^{(i,j)}$ Histogram for DAZ Indicator, H^1 Case 3, $N_X = N_Y = 32$

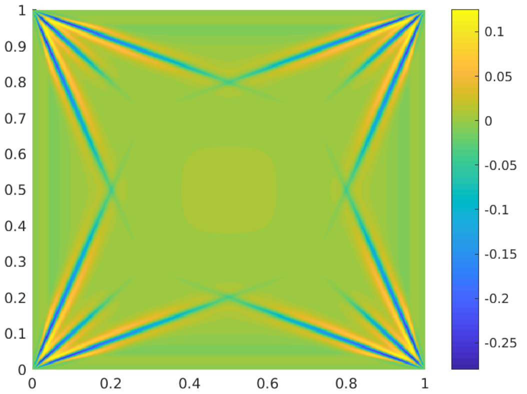

Figure 6.50 $\log_{10} \theta_{ang.}^{(i,j)}$ for LeR/TE-AD Estimator, H^1 Case 3, $N_X = N_Y = 512$

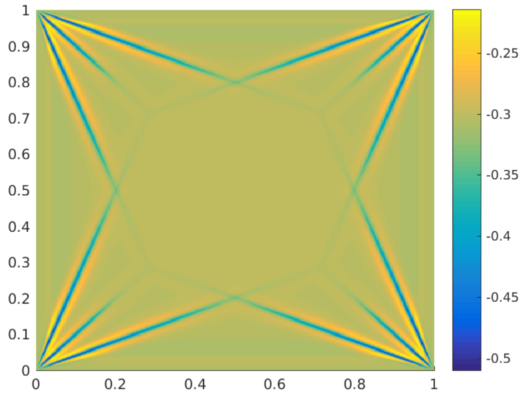

Figure 6.51 $\log_{10} \theta_{ang.}^{(i,j)}$ for RW Estimator, H^1 Case 3, $N_X = N_Y = 512$

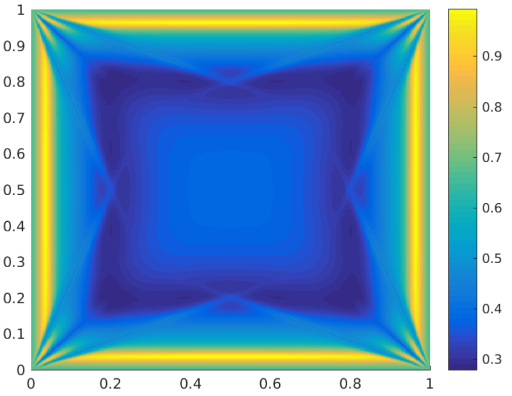

Figure 6.52 $\log_{10} \theta_{ang.}^{(i,j)}$ for DAZ Indicator, H^1 Case 3, $N_X = N_Y = 512$

LeR/TE-AD estimator is far more accurate than in the previous cases. This is likely because the high scattering ratio and large optical thickness mitigate the effects of the SCs more than in either of the two previous cases.

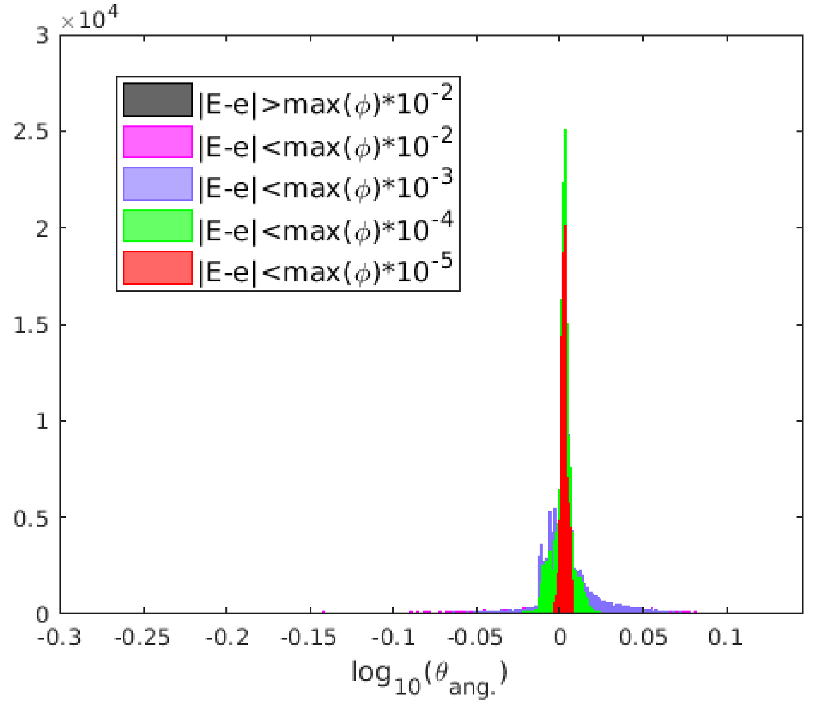

Figure 6.53 $\log_{10}\theta_{ang.}^{(i,j)}$ Histogram for LeR/TE-AD Estimator, H^1 Case 3, $N_X = N_Y = 512$

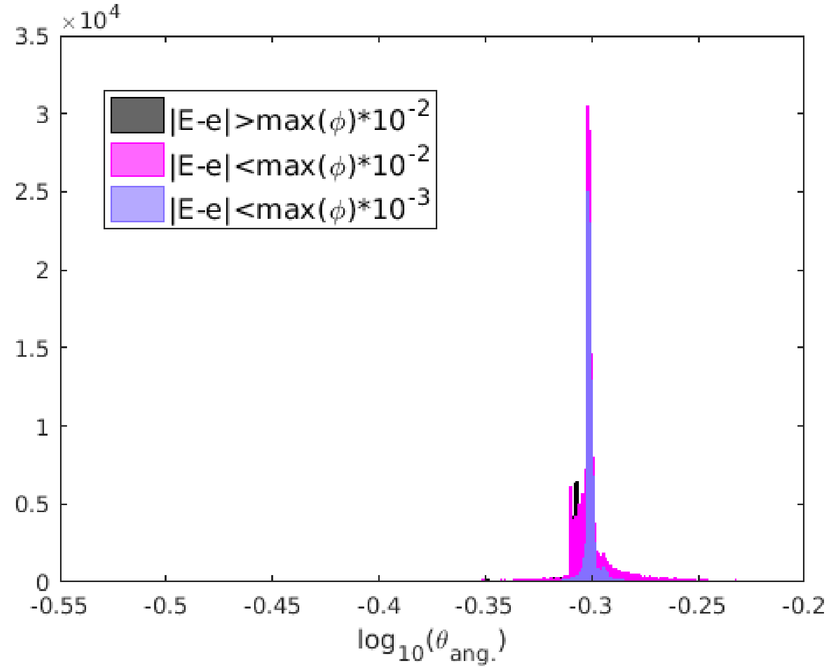

Figure 6.54 $\log_{10}\theta_{ang.}^{(i,j)}$ Histogram for RW Estimator, H^1 Case 3, $N_X = N_Y = 512$

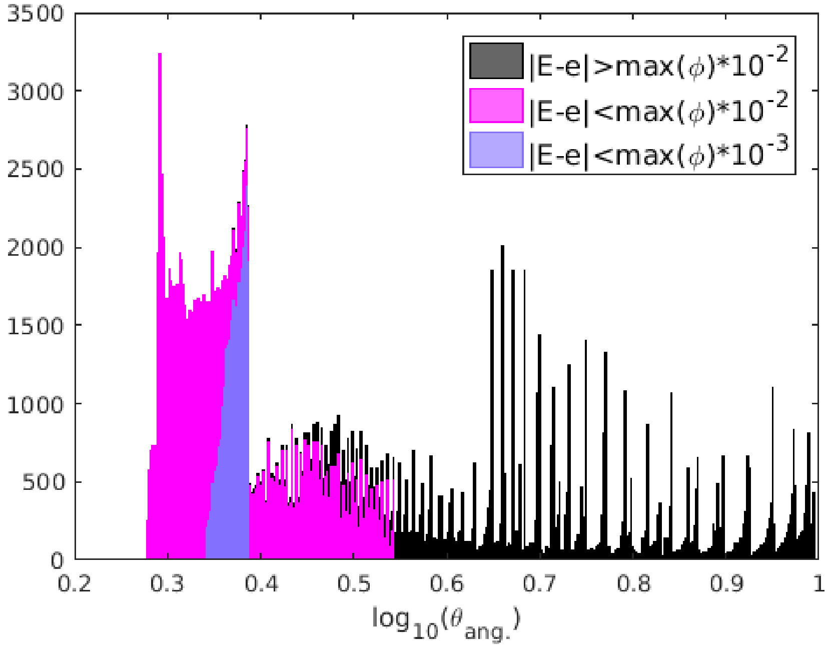

Figure 6.55 $\log_{10}\theta^{(i,j)}_{ang.}$ Histogram for DAZ Indicator, H^1 Case 3, $N_X = N_Y = 512$

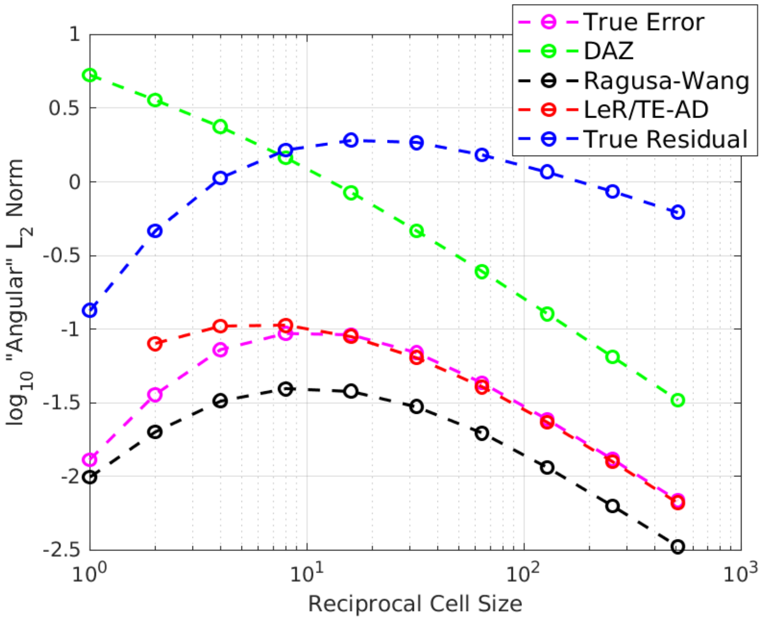

Figure 6.56 Angular Error/Estimator L_2 Norm Convergence for H^1 Case 3

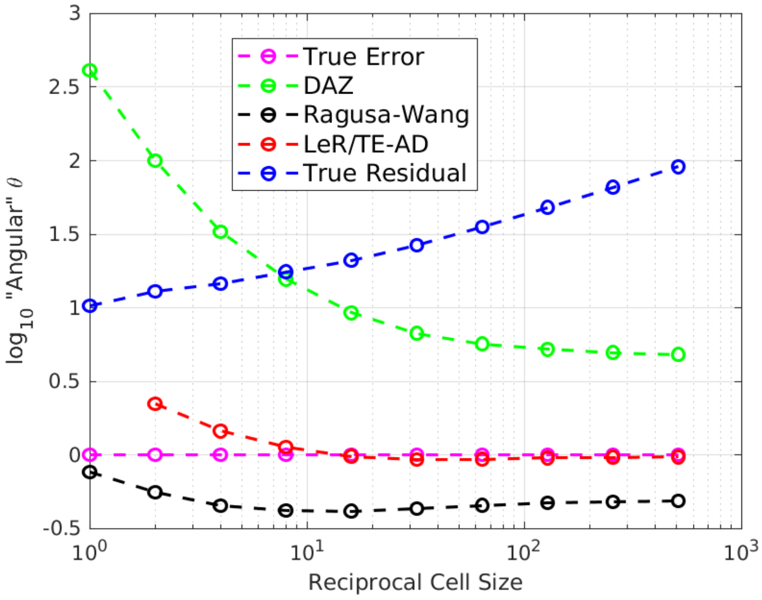

Figure 6.57 Angular Effectivity Convergence for H^1 Case 3

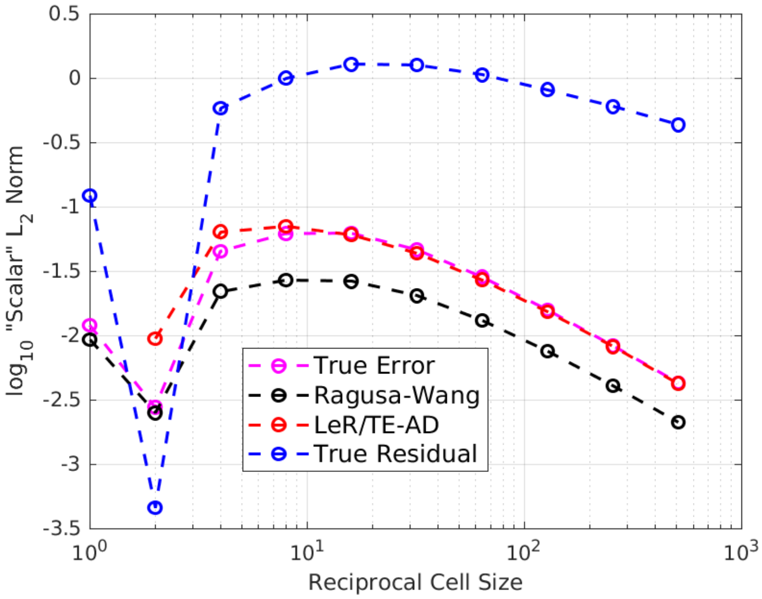

Figure 6.58 Scalar Error/Estimator L_2 Norm Convergence for H^1 Case 3

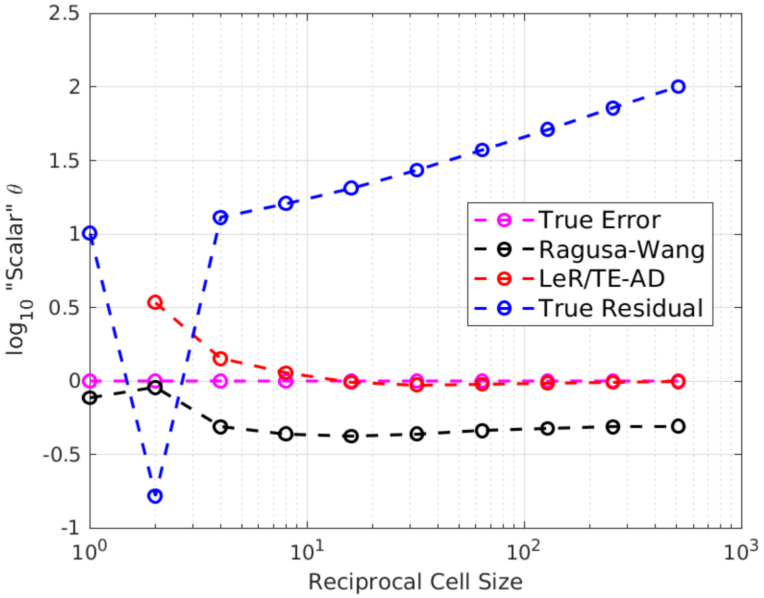

Figure 6.59 Scalar Effectivity Convergence for H^1 Case 3

6.2 H^1 General Behavior

Next we observe the trends of some global quantities with changing problem parameters. It is difficult to choose a single quantity that will convey sufficient information about the estimators' performance, so four global quantities will be observed: the global norm, the fraction of local estimates that are cautious (i.e., $\theta_{ang.}^{(i,j)} \geq 1$), the fraction of local estimates within a specified range about the value of $\theta_{ang.}^{(i,j)} = 1$, indicating exact agreement between the estimated and true errors, and the standard deviation of $\log_{10} \theta_{ang.}^{(i,j)}$, which should indicate the estimator's usefulness as an error shape estimator. The DAZ, RW, and LeR/TE-AD estimators are considered along with the TE-AD residual approximation, due to its potential as an error bound calculated along the way to a LeR/TE-AD estimate. First, these quantities are plotted versus computation time with varying mesh size for the same problem parameters as H^1 Case 1. This is done to convey the efficiency of the estimator/indicators with respect to computation time.

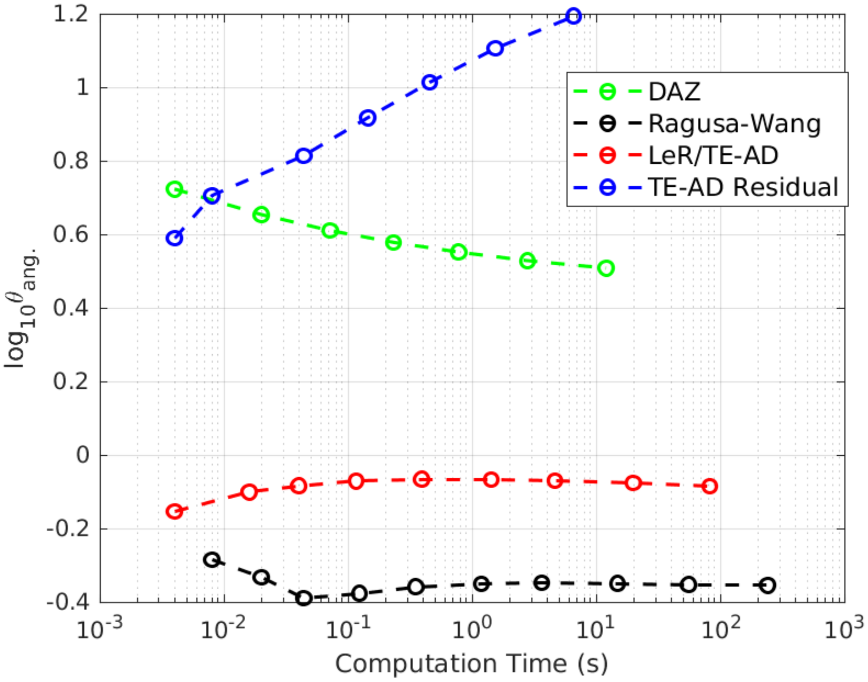

Figure 6.60 Global Angular Effectivity vs. computation time

Figure 6.60 shows the global angular effectivities versus computation time. The values that have computational times shorter than the computer's clock precision are not plotted. The results here are similar to Figure 6.22. No estimator gives a more accurate global estimate than the LeR/TE-AD estimator for the computational cost. However, the DAZ estimator is about an order of magnitude cheaper than the LeR/TE-AD and RW estimators and gives an bound on the global error. The residual approximation is cheapest to compute, but the different convergence order hurts its prospect as a global error estimate or error bound, except in the most cautious sense. This fact is evident from its trend of increasing overestimation with mesh refinement, in contrast to the DAZ estimator whose upper bound tightens closer to the true error with mesh refinement.

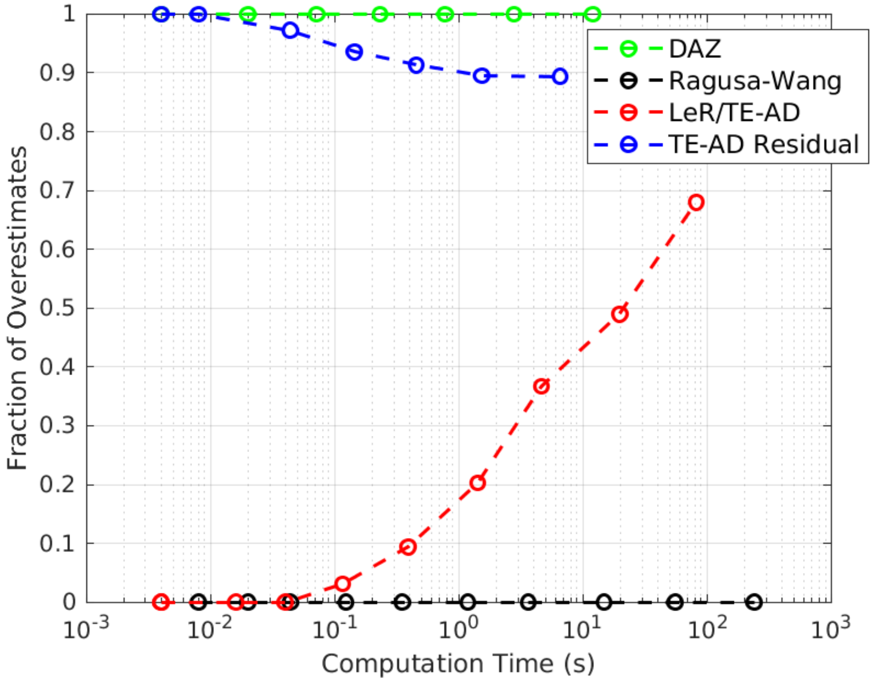

Figure 6.61 Fraction of cells with $\theta_{ang.}^{(i,j)} - 1 \geq 0$ vs. computation time

Figure 6.61 shows the fraction of estimates that overestimate (cautious), hence bound from above, the true error. The RW estimator exhibits no local cautiousness because it precisely underestimates the true error, as shown previously. The LeR/TE-AD estimator evidently becomes more cautious as the mesh is refined for this case, although the performance of the DAZ indicator is far more efficient in terms of computational cost if a locally cautious estimate of the error is desired. The residual for this case is cheapest of all, and it bounds about 90% or more of all cells' local error.

Figure 6.62 shows the fraction of cells that have local estimates within 10%, 25%, or 50% of the true error. The DAZ results and some RW results are not plotted because they are zero for all meshes. For this problem the DAZ indicator is not very accurate, so no values are contained in the plot. Figures 6.6 and 6.16 corroborate this, as for this case, the DAZ indicator has a floor of about $\theta_{ang.}^{(i,j)} \geq 2$ (200% of the true error). The RW estimator's bias towards underestimation is evident, as it is not accurate unless the 50% bound is considered. The 50%

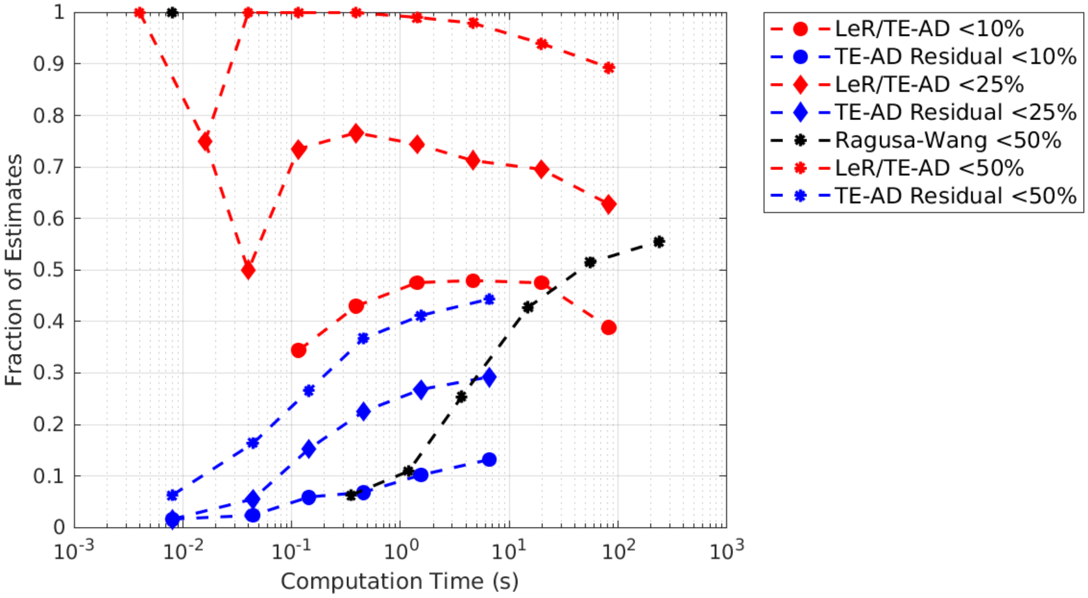

Figure 6.62 Fraction of cells within some bound vs. computation time

bound is accurate because the predicted bias of the RW estimator will be at $\theta_{ang.}^{(i,j)} = 0.5$, which means the effectivities will coalesce at the lower end of the 50% bound. The LeR/TE-AD estimator is quite accurate, and while its accuracy appears to decrease as the mesh is refined, this is mostly because the error is decreasing to the point that the estimator is not able to accurately estimate it. Put another way, the solution is converging asymptotically, but the error estimate is not because of the inherent failings of the TE-AD residual approximation. Perhaps surprisingly, the TE-AD residual registers on this plot.

Figure 6.63 shows the standard deviation of each estimator, an indication of its ability as a shape estimator regardless of how well it predicts the magnitude of the error in each cell of the mesh. While the distribution of $\log_{10} \theta_{ang.}^{(i,j)}$ is not a probabilistic one, the magnitude of an estimator/indicator's standard deviation can be related to that estimator/indicator's utility as a shape estimator. Consider the local RW estimator for the H^1 Case 1, $N_X = N_Y = 512$, Figure 6.15, compared to the local LeR/TE-AD estimator for the same case, Figure 6.14. Judging by the figures, the RW estimator could be considered a better shape estimate because the maximum-to-minimum $\log_{10}$-scale width of the spread of its angular effectivities is smaller, and the height of its peak is taller. It should therefore have a smaller standard deviation. The corresponding values on Figure 6.63 (largest computation times for each estimator correspond to the $N_X = N_Y = 512$ mesh) show the RW estimator has a smaller standard deviation by over a factor of three compared to the next best estimator/indicator, LeR/TE-AD. In general, aside from small mesh sizes when the solution is not yet asymptotically converging with mesh refinement, the RW estimator is the best shape function for a given execution time regardless of mesh size. Note that as the estimators approach asymptotic convergence with mesh refinement

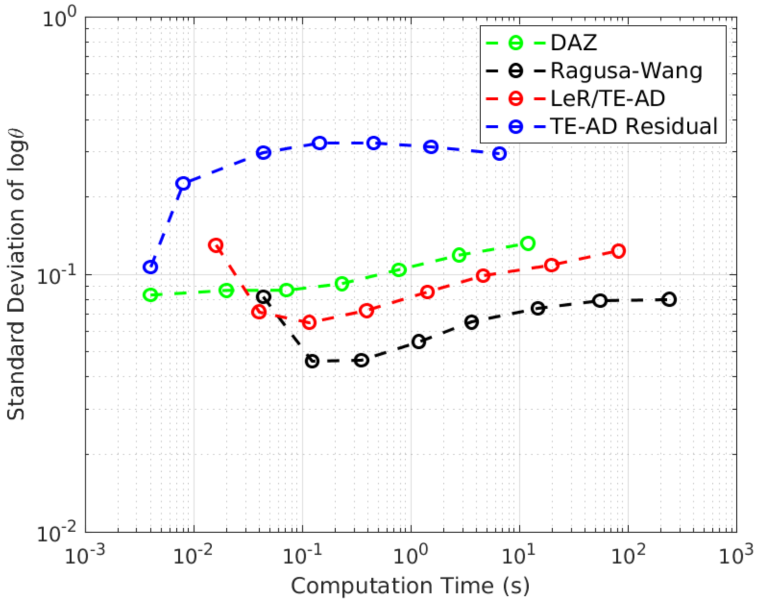

Figure 6.63 Standard deviation of $\log_{10}\theta_{ang.}^{(i,j)}$ vs. computation time

the estimator/indicators' standard deviations counter-intuitively *increase* because the outlier effectivity "tails" get further away from the peak.

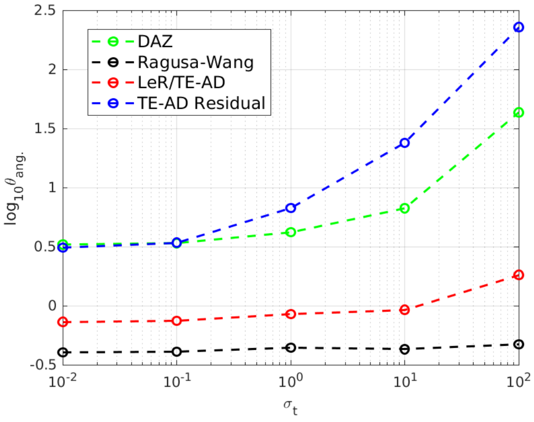

Figure 6.64 Global Angular Effectivity vs. σ_t, $c = 0.1$, $N_X = N_Y = 32$, H^1

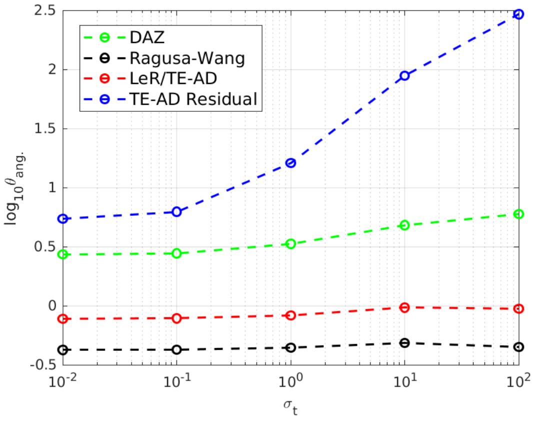

Figure 6.65 Global Angular Effectivity vs. σ_t, $c = 0.1$, $N_X = N_Y = 512$, H^1

The same set of angular quantities are observed in Figures 6.64-6.69, which show the global angular effectivity with varying optical thickness for scattering ratios of $c = 0.1$, $c = 0.5$, and $c = 0.9$ and for $N_X = N_Y = 32$ and $N_X = N_Y = 512$. Generally, the global effectivity of the

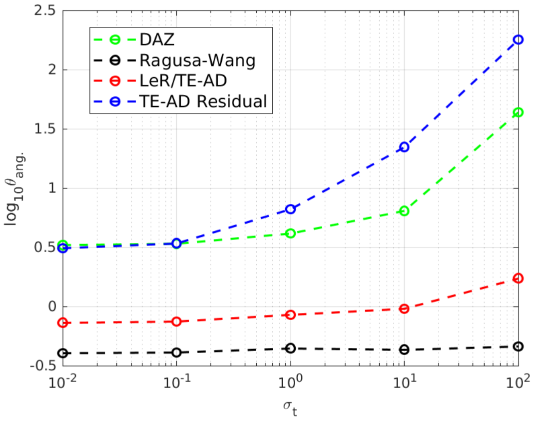

Figure 6.66 Global Angular Effectivity vs. σ_t, $c = 0.5$, $N_X = N_Y = 32$, H^1

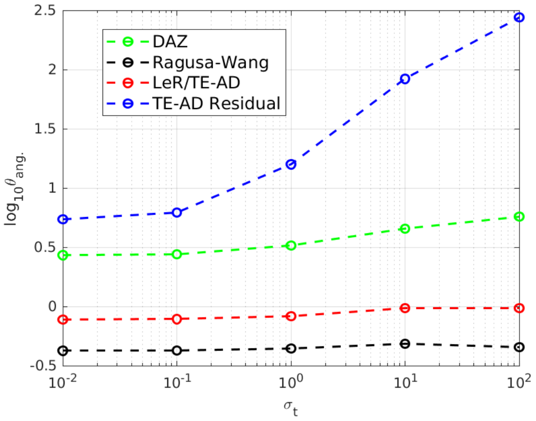

Figure 6.67 Global Angular Effectivity vs. σ_t, $c = 0.5$, $N_X = N_Y = 512$, H^1

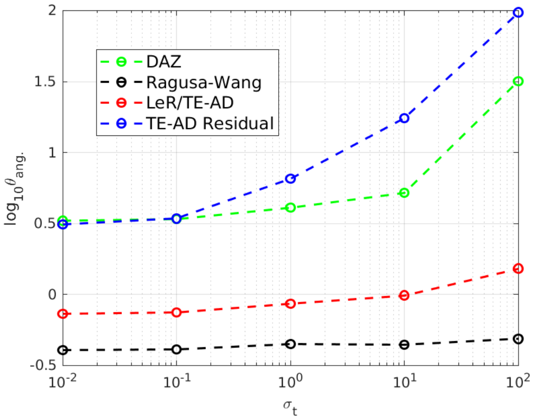

Figure 6.68 Global Angular Effectivity vs. σ_t, $c = 0.9$, $N_X = N_Y = 32$, H^1

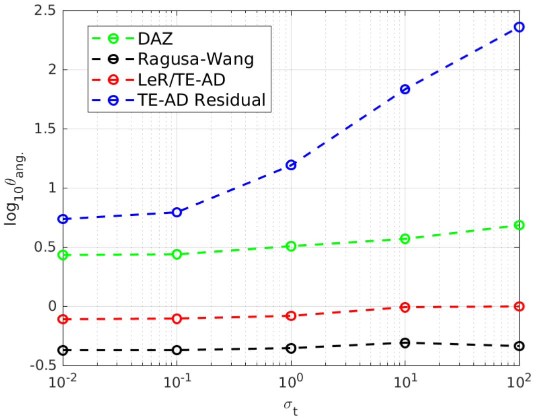

Figure 6.69 Global Angular Effectivity vs. σ_t, $c = 0.9$, $N_X = N_Y = 512$, H^1

LeR/TE-AD estimator and RW estimator are invariant to changes in scattering ratio and optical thickness. In the fine mesh case when the discrete solution has reached asymptotic convergence with respect to mesh refinement, the RW estimator is located about the predicted bias of $\log_{10}\theta_{ang.}^{(i,j)} = -0.3$, and the LeR/TE-AD estimator, which is the most accurate, is consistently between $\log_{10}\theta_{ang.}^{(i,j)} = -0.2$ and $\log_{10}\theta_{ang.}^{(i,j)} = 0$, suggesting that there could also be a predictable bias for the LeR/TE-AD estimator. The DAZ estimator and the TE-AD residual, when used as an indicator, are sensitive to optical thickness and scattering ratio. The Duo estimator is expected to be sensitive to the scattering ratio because the scattering ratio is related to the accuracy of an additional high-order sweep when compared to a fully converged high-order problem. Using the residual approximation as a mathematical bound is instructive, although it has been shown that the residual has a different order of convergence than the error, so it should not be used as an indicator of the error with mesh refinement.

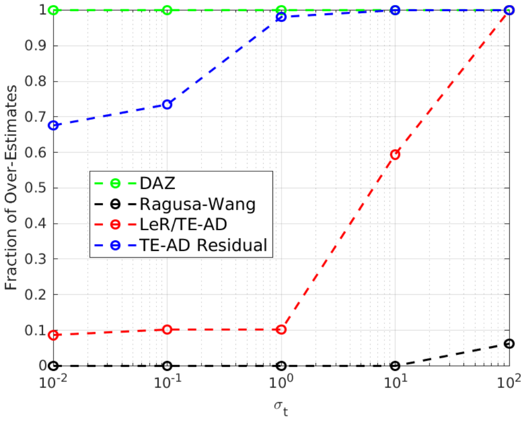

Figure 6.70 Fraction of cells with $\theta^{(i,j)}_{ang.} - 1 \geq 0$ vs. σ_t, $c = 0.1$, $N_X = N_Y = 32$, H^1

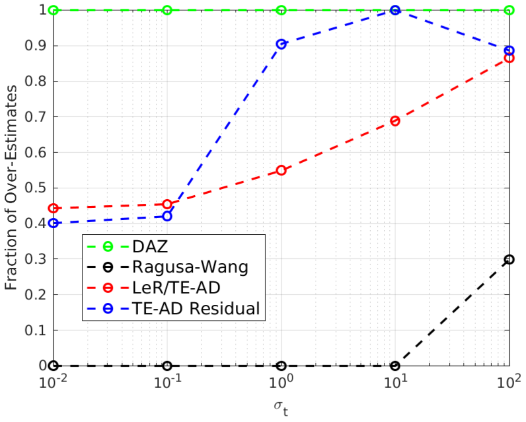

Figure 6.71 Fraction of cells with $\theta^{(i,j)}_{ang.} - 1 \geq 0$ vs. σ_t, $c = 0.1$, $N_X = N_Y = 512$, H^1

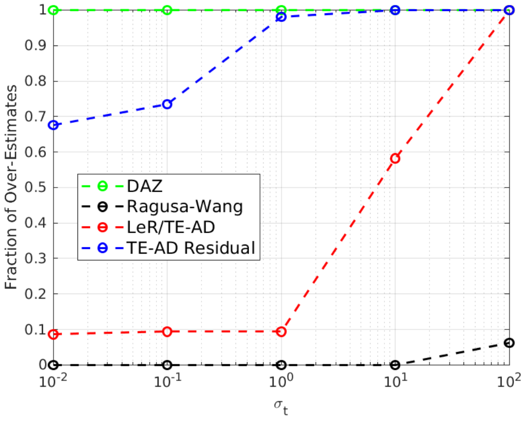

Figure 6.72 Fraction of cells with $\theta^{(i,j)}_{ang.} - 1 \geq 0$ vs. σ_t, $c = 0.5$, $N_X = N_Y = 32$, H^1

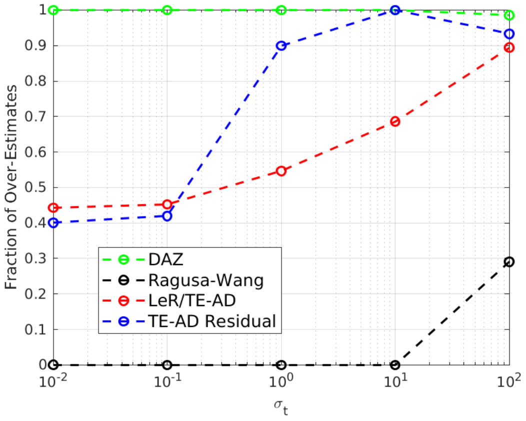

Figure 6.73 Fraction of cells with $\theta^{(i,j)}_{ang.} - 1 \geq 0$ vs. σ_t, $c = 0.5$, $N_X = N_Y = 512$, H^1

The fraction of local estimates that overestimate is observed next, Figures 6.70-6.75. As would be expected from the global effectivity, the RW estimator is not locally cautious. Because it is a good shape estimator and has bias to underestimate, most if not all local estimates will underestimate the true error. The LeR/TE-AD estimator is minimally cautious in a local sense for the coarse mesh cases when low-to-medium optical thicknesses are considered. As the optical

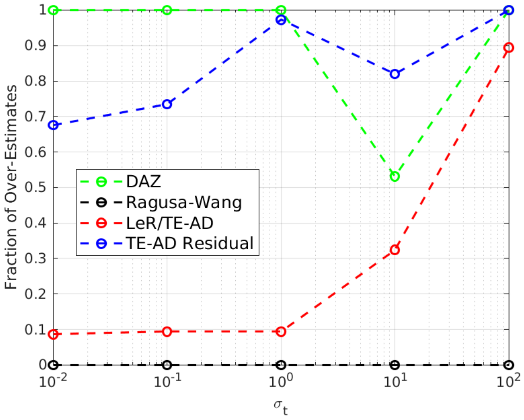

Figure 6.74 Fraction of cells with $\theta_{ang.}^{(i,j)} - 1 \geq 0$ vs. σ_t, $c = 0.9$, $N_X = N_Y = 32$, H^1

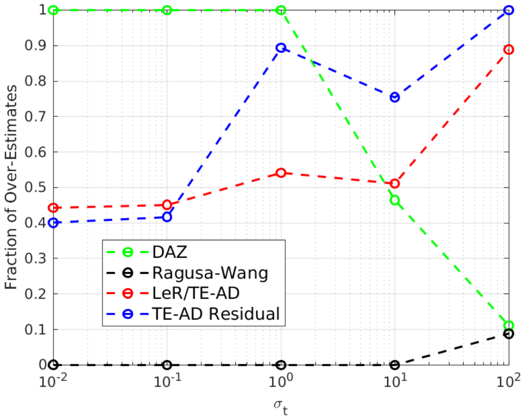

Figure 6.75 Fraction of cells with $\theta_{ang.}^{(i,j)} - 1 \geq 0$ vs. σ_t, $c = 0.9$, $N_X = N_Y = 512$, H^1

thickness increases and the mesh is refined, the LeR/TE-AD estimator becomes more cautious. The DAZ indicator locally bounds the error for most cases considered, although at larger optical thicknesses it underestimates some errors, especially so when the scattering ratio is large. When the local residual approximation is considered as an error indicator, it tends to be rather locally cautious, especially at higher optical thicknesses.

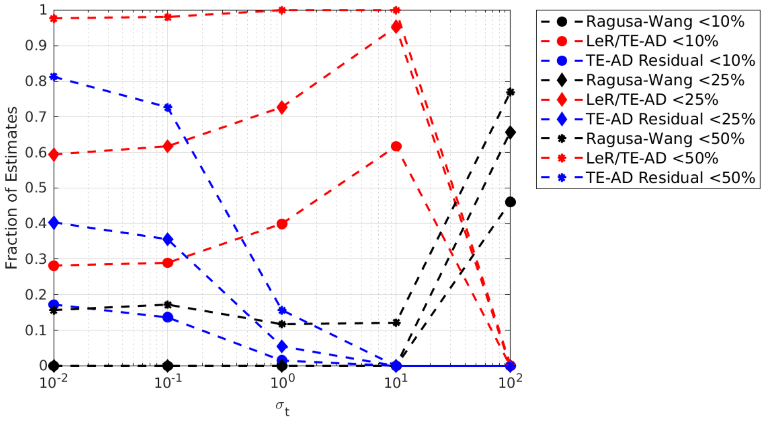

Figure 6.76 Fraction of cells with $|\theta_{ang.}^{(i,j)} - 1| \leq$ specified bounds vs. σ_t, $c = 0.1$, $N_X = N_Y = 32$, H^1

The fractions of local estimates that are within some bound interval are observed next, Figures 6.76-6.81. The LeR/TE-AD estimator is by far the most accurate estimator by all three measures with the exception of cases with very large optical thickness. It is most accurate for low-to-large optical thicknesses on both coarse and fine meshes, with 90% of cells having error

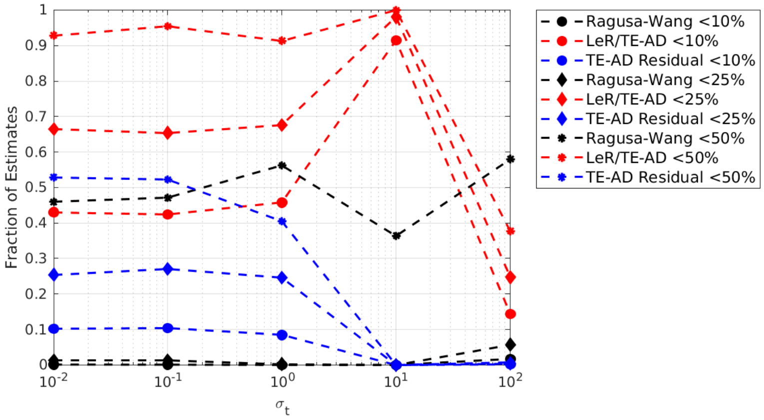

Figure 6.77 Fraction of cells with $|\theta_{ang.}^{(i,j)} - 1| \le$ specified bounds vs. σ_t, $c = 0.1$, $N_X = N_Y = 512$, H^1

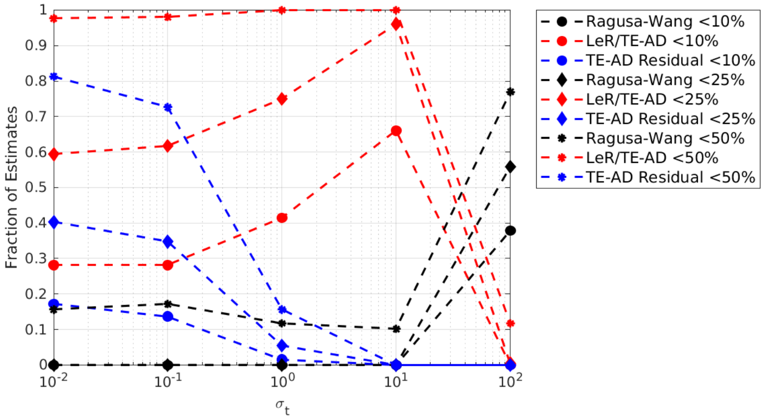

Figure 6.78 Fraction of cells with $|\theta_{ang.}^{(i,j)} - 1| \le$ specified bounds vs. σ_t, $c = 0.5$, $N_X = N_Y = 32$, H^1

estimates with 50% or better accuracy relative to the true error. The LeR/TE-AD estimator gets progressively more accurate as the optical thickness is increased until it reaches very large optical thickness (somewhere between $\sigma_t = 10.0$ and $\sigma_t = 100.0$), where this trend is reversed. Similar to Figure 6.62, the RW estimator is generally inaccurate unless the 50% bound is considered, due to the asymptotic bias analyzed earlier. For very large optical thickness and $N_X = N_Y = 32$ mesh, the RW estimator is accurate because the problem has not reached asymptotic convergence with respect to cell size; therefore, the bias has not set in. These plots suggest the local DAZ indicator cannot be expected to provide a good estimate of the error, as the cases that give any amount of agreement are undoubtedly outliers. The residual approximation gives a surprisingly good estimate of the error for cases with low-to-medium optical thickness; however, the utility of using the residual approximation as an estimate for the error is suspect. First, the residual approximation should not be equal to the error in any

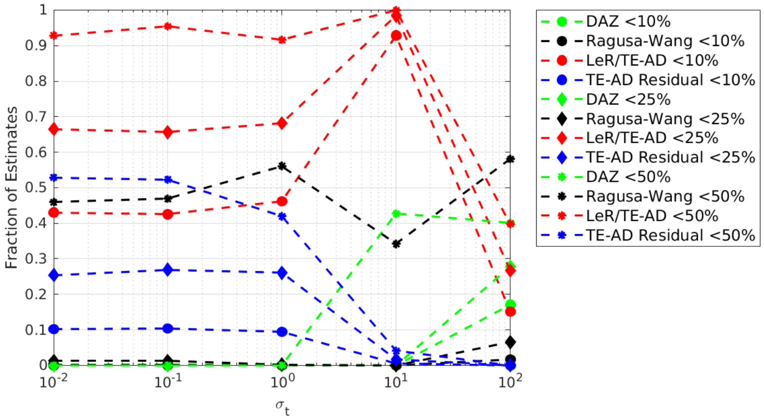

Figure 6.79 Fraction of cells with $|\theta_{ang.}^{(i,j)} - 1| \leq$ specified bounds vs. σ_t, $c = 0.5$, $N_X = N_Y = 512$, H^1

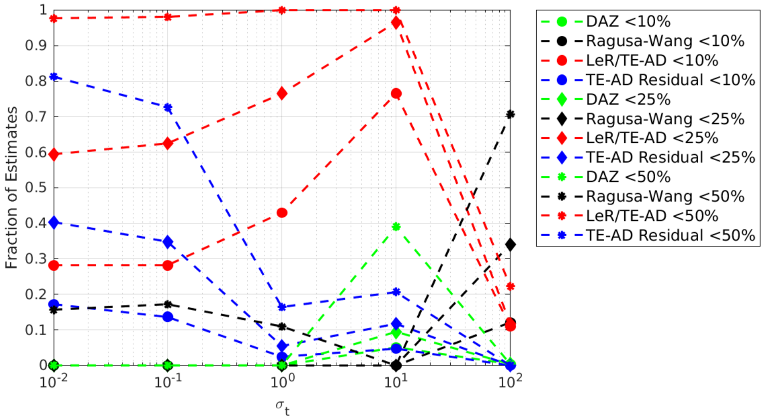

Figure 6.80 Fraction of cells with $|\theta_{ang.}^{(i,j)} - 1| \leq$ specified bounds vs. σ_t, $c = 0.9$, $N_X = N_Y = 32$, H^1

sense, so at best it could be an error indicator. Second, it has been shown that the true residual converges to a constant in cells adjacent to the global incoming boundary and on the SCs for H^1 problems paired with DGFEM-0, unlike the true error, so a hypothetical perfect approximation of the residual used as an error indicator would incorrectly suggest no decrease in error as the mesh was refined for these regions.

The standard deviation of the $\log_{10} \theta_{ang.}^{(i,j)}$ distribution is plotted as an indication of each estimator's quality as a shape estimator in the indicated problem parameter regime shown in Figures 6.82-6.87. As expected, the RW estimator has the best shaping function, especially for large optical thickness, although it and the LeR/TE-AD estimator suffer at very large optical thickness ($\sigma_t = 100.0$), likely because the true error is very low for these problems, and this is not well captured by the estimator/indicators. Although the RW estimator is robust as a shape estimator for these cases, something that must be considered is that these idealized

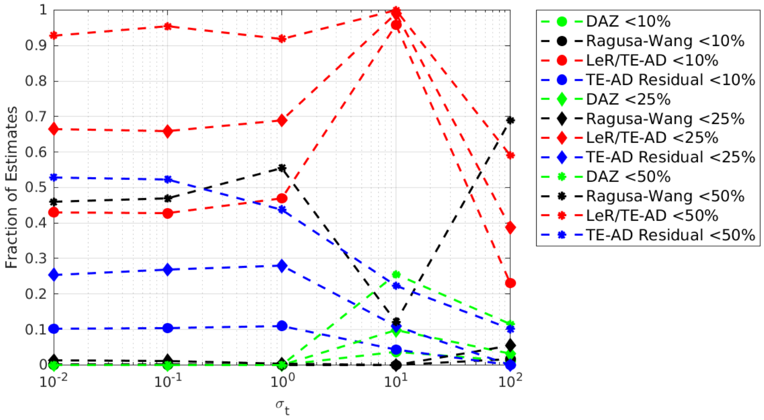

Figure 6.81 Fraction of cells with $|\theta_{ang.}^{(i,j)} - 1| \leq$ specified bounds vs. σ_t, $c = 0.9$, $N_X = N_Y = 512$, H^1

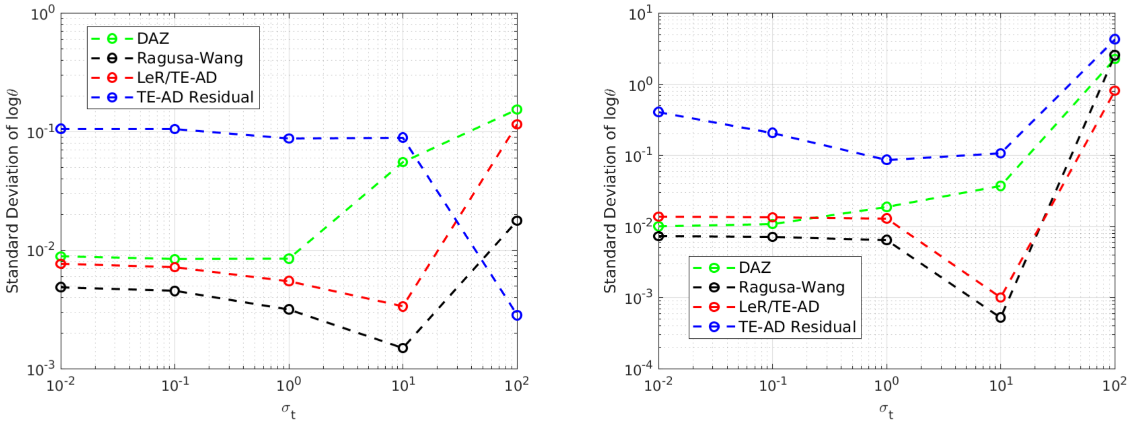

Figure 6.82 Standard deviation of $\log_{10} \theta_{ang.}^{(i,j)}$ vs. σ_t, $c = 0.1$, $N_X = N_Y = 32$, H^1

Figure 6.83 Standard deviation of $\log_{10} \theta_{ang.}^{(i,j)}$ vs. σ_t, $c = 0.1$, $N_X = N_Y = 512$, H^1

homogeneous problems are generally uniform, thus all cells reach local asymptotic convergence with respect to decreasing mesh size simultaneously and at the same asymptotic order. In a heterogeneous problem it may take a very fine mesh for all cells to reach local asymptotic convergence everywhere in the domain. The LeR/TE-AD estimator, while not as robust as the RW estimator, is generally good when compared to the other estimates. The DAZ indicator is very good as a shape estimate at low-to-medium optical thicknesses, but it worsens as the scattering ratio and optical thickness are increased, both of which will decrease the accuracy of the HOPS relative to a fully converged sweep. The residual approximation is a poor shape estimator, as its standard deviation is an order of magnitude or more larger than the LeR/TE-AD estimator for most problems.

Finally, the computation time for each estimate (not including the original discrete transport solution time) is plotted in Figures 6.88-6.93. As expected, the residual approximation and DAZ

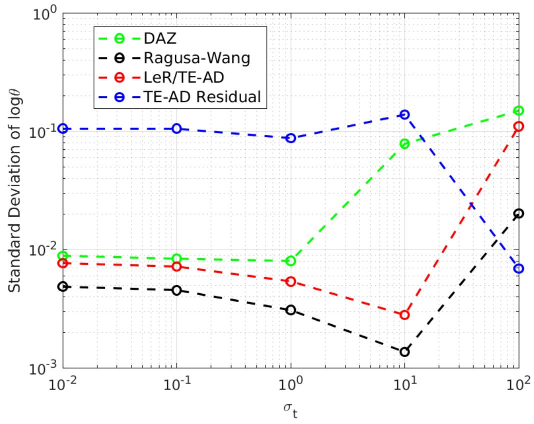

Figure 6.84 Standard deviation of $\log_{10}\theta^{(i,j)}_{ang.}$ vs. σ_t, $c = 0.5$, $N_X = N_Y = 32$, H^1

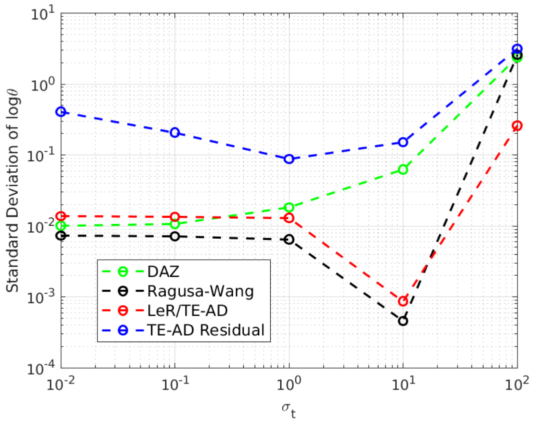

Figure 6.85 Standard deviation of $\log_{10}\theta^{(i,j)}_{ang.}$ vs. σ_t, $c = 0.5$, $N_X = N_Y = 512$, H^1

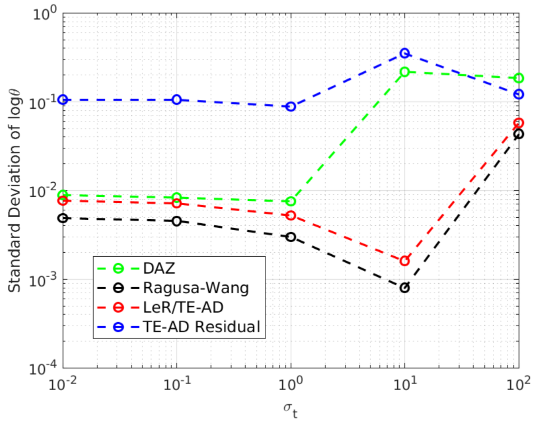

Figure 6.86 Standard deviation of $\log_{10}\theta^{(i,j)}_{ang.}$ vs. σ_t, $c = 0.9$, $N_X = N_Y = 32$, H^1

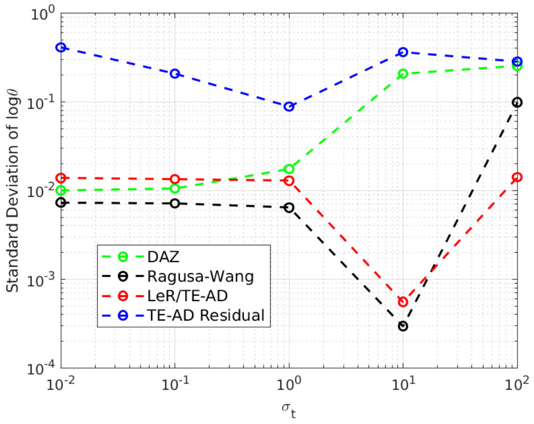

Figure 6.87 Standard deviation of $\log_{10}\theta^{(i,j)}_{ang.}$ vs. σ_t, $c = 0.9$, $N_X = N_Y = 512$, H^1

estimator computation times are mostly invariant to changes in scattering ratio and optical thickness, because these variables should have no influence on the computation time of these quantities. The LeR/TE-AD and RW estimators are mostly invariant to changes in scattering ratio and optical thickness for low-to-medium optical thicknesses. The computation time shoots up at larger optical thicknesses, with a larger jump corresponding to higher scattering ratio. In general, the computational cost of the RW estimator is approximately 2-3 times that of the LeR/TE-AD estimator, although one would expect this multiplier to trend to 4 in 2d, i.e., the ratio of computational cells in the applicable uniform halving of the per-dimension size of all cells, as the iterations required to reach convergence trends towards infinity. All estimates have computation times that scale linearly with total number of cells in the mesh.

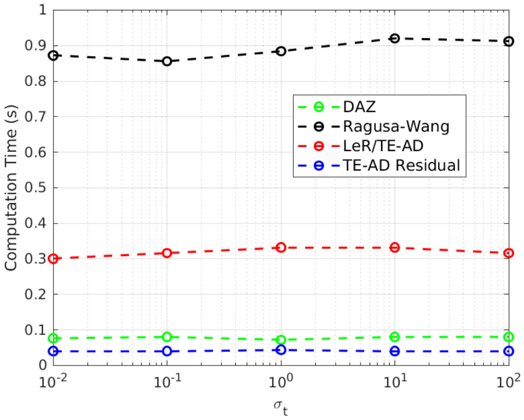

Figure 6.88 Computation time vs. σ_t, $c = 0.1$, $N_X = N_Y = 32$, H^1

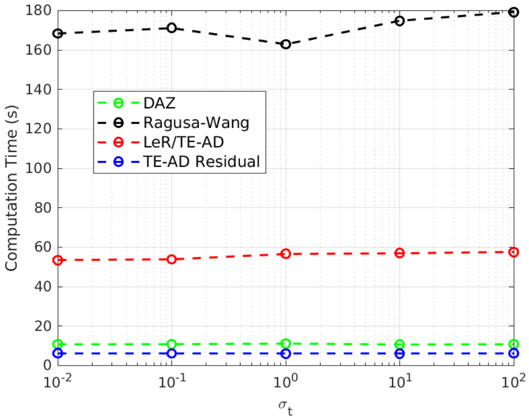

Figure 6.89 Computation time vs. σ_t, $c = 0.1$, $N_X = N_Y = 512$, H^1

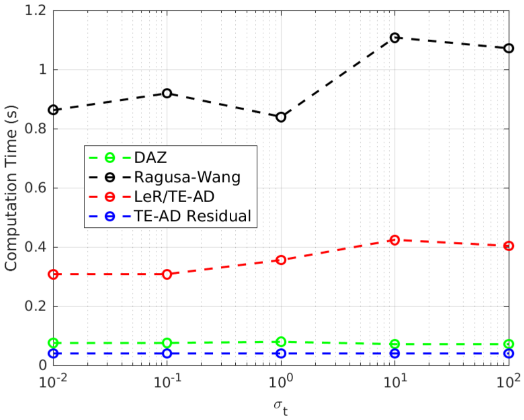

Figure 6.90 Computation time vs. σ_t, $c = 0.5$, $N_X = N_Y = 32$, H^1

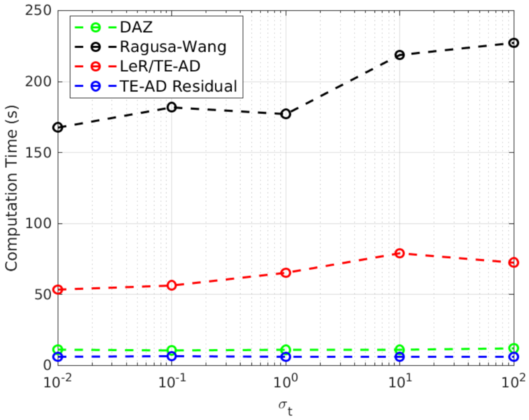

Figure 6.91 Computation time vs. σ_t, $c = 0.5$, $N_X = N_Y = 512$, H^1

6.3 H^1 Conclusions

Overall, several impressions can be taken from the preceding figures for H^1 problems. As a global error estimate, the residual source estimator with the TE-AD residual is the most accurate, although it is not globally cautious. With respect to changing optical thickness and scattering ratio, the behaviors of the global effectivity of the LeR/TE-AD and RW estimators are relatively insensitive. The DAZ estimator is globally cautious for all H^1 cases, in agreement with the theory, and it becomes more cautious and less accurate as the optical thickness and scattering ratio are increased, as this will increase the iterative error of the HOPS. The TE-AD residual approximation has promise as an on-the-fly error bound in conjunction with the LeR/TE-AD estimator, although it has a different convergence order with respect to mesh refinement than the true error. As a local estimator, the LeR/TE-AD estimator is consistently more cautious than the RW estimator due to the inherent underestimation bias in the RW estimator. The DAZ

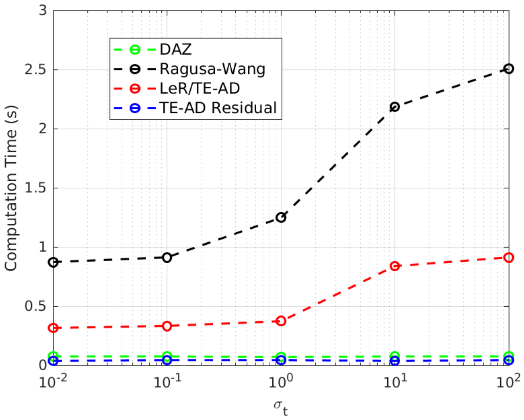

Figure 6.92 Computation time vs. σ_t, $c = 0.9$, $N_X = N_Y = 32$, H^1

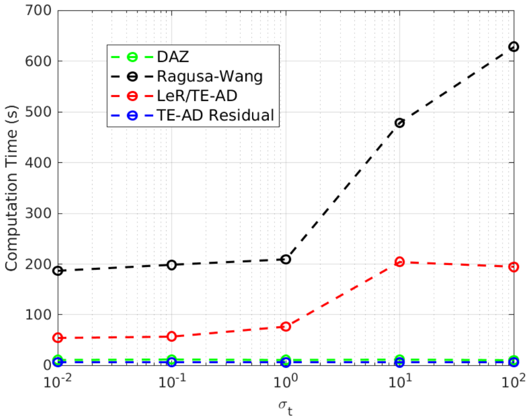

Figure 6.93 Computation time vs. σ_t, $c = 0.9$, $N_X = N_Y = 512$, H^1

indicator locally overestimates the error for low-to-medium optical thicknesses, although this is not guaranteed by theory, but is not as reliable otherwise. The TE-AD residual approximation is a cautious estimate of the error for a majority of local errors and is more reliably cautious at larger optical thicknesses. As a local error estimate, the LeR/TE-AD estimator is far superior to all other estimates in nearly every case in terms of accuracy. The RW estimator suffers from a bias known *a priori* once all the cells enter the asmyptotic regime, although predicting the value of this bias and when it takes effect (i.e., when the domain is locally asymptotic with respect to mesh refinement) would require multiple fine mesh calculations and be potentially impractical in real-life problems. The DAZ indicator is not accurate by the metrics presented in this work, and while the TE-AD residual approximation is surprisingly accurate when used as an error estimate, it has serious shortcomings which have been outlined earlier. By using the standard deviation of the $\log_{10} \theta_{ang.}$ distribution as an indication of the quality as a shape estimator, the RW estimator is shown to be unquestionably the best shape estimator for these cases. The LeR/TE-AD estimator performs well as a shape estimator at low-to-high optical thicknesses, and the DAZ indicator performs well at low-to-medium optical thicknesses. The TE-AD residual approximation has a very large standard deviation, which is probably because the local residual on the boundary and the SCs converges to a constant while the local true error on these cells converges to zero with mesh refinement. The estimators have predictable behavior in terms of their relative computation time, and one can expect the computation time of the estimators that require additional transport solves to follow the same computation time trends as the initial discrete transport solution.

Chapter 7

Estimators Comparison and Assessment for H^0 Problems

The next set of cases examined are the problems that are H^0. Like the H^1 cases, the problem parameters that are modified are the optical thickness (via σ_t), the cell size h via the number of cells $N_X \times N_Y$, and the scattering ratio c. The DGFEM order is fixed to 0, and all cases of the residual source utilize the TE-AD residual. Recall that for H^0 cases the solution itself is discontinuous along the SCs.

7.1 H^0 Case Study

7.1.1 H^0 Case 1

The first H^0 case considered at has medium optical thickness ($\sigma_t = 1.0$) and a high scattering ratio $c = 0.9$. A coarse $N_X = N_Y = 32$ is applied to the domain. These problem parameters are identical to those used in Case 1 of the H^1 test configuration.

First the angular effectivities are plotted over the domain for the LeR/TE-AD, RW, and DAZ estimator/indicators, Figures 7.1-7.3, respectively. Note that unlike H^1 problems, which have reflective and rotational symmetry, H^0 problems have reflective symmetry, but not rotational symmetry, due to the different boundary conditions on the North/South faces from the West/East faces.

The histograms for the same estimators/indicators, Figures 7.4-7.6, show many similarities to the H^1 case; the noteworthy features that exist in the H^1 problem also exist in the H^0 problem. For example, both RW and LeR/TE-AD estimators have distinct peaks. The LeR/TE-AD estimator peak is very close to exact agreement, and the RW estimator peak has the same underestimation bias. The bias is identical to the H^1 cases because, while the global error should converge with mesh refinement at a different rate than the H^1 problem, the local convergence of cells unaffected by SCs will be identical. The LeR/TE-AD estimator is more cautious than the RW estimator. The local DAZ indicator has similar trends for this case as it did in the

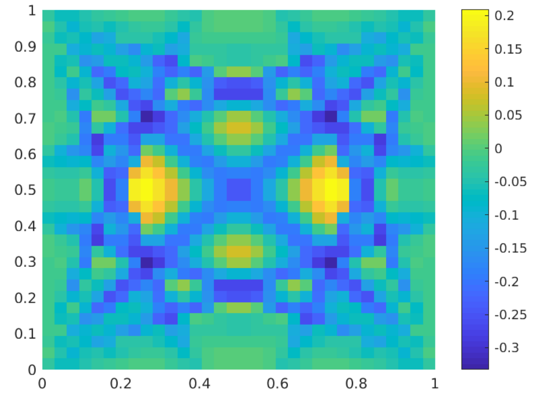

Figure 7.1 $\log_{10}\theta_{ang.}^{(i,j)}$ for LeR/TE-AD Estimator, H^0 Case 1, $N_X = N_Y = 32$

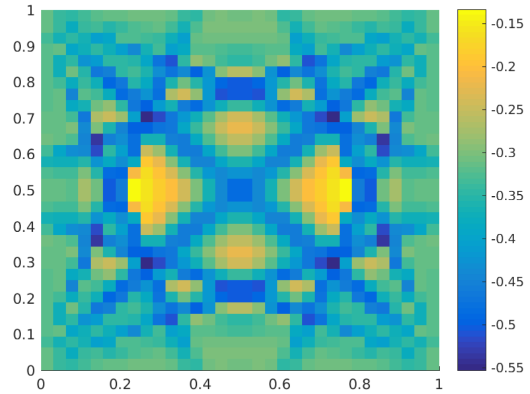

Figure 7.2 $\log_{10}\theta_{ang.}^{(i,j)}$ for RW Estimator, H^0 Case 1, $N_X = N_Y = 32$

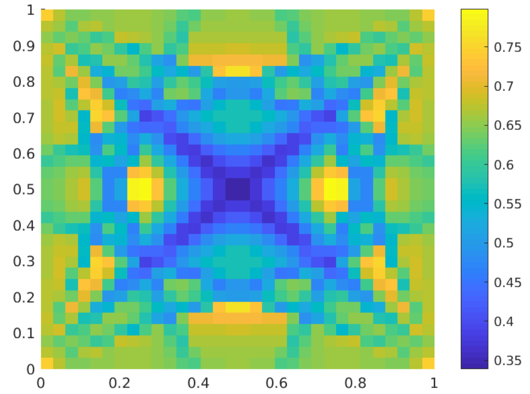

Figure 7.3 $\log_{10}\theta_{ang.}^{(i,j)}$ for DAZ Indicator, H^0 Case 1, $N_X = N_Y = 32$

H^1 case, as the effectivites are concentrated about the same value peak and bounds, and it is locally cautious.

The scalar versions of the LeR/TE-AD estimator and RW estimator are presented in Figures 7.7 and 7.8. The histograms for the scalar estimators are shown in Figures 7.9 and 7.10. Once again, the scalar versions are less accurate than the angular versions but have similar features, such as distinct peaks.

The same problem configuration is considered with a fine $N_X = N_Y = 512$ applied, with angular effectivities plotted over the domain and tallied into histograms, Figures 7.11-7.16. Once again, both LeR/TE-AD and RW estimators have deviation from the value at which the distribution of effectivities peak at and around SCs. Regarding the LeR/TE-AD estimator, the distribution of effectivities is much more spread out. Recall that for H^1 Case 1, the minimum and maximum of non-outlier $\log_{10}\theta_{ang.}^{(i,j)}$ values were near -0.3 and 0.3, respectively (Figure 6.14),

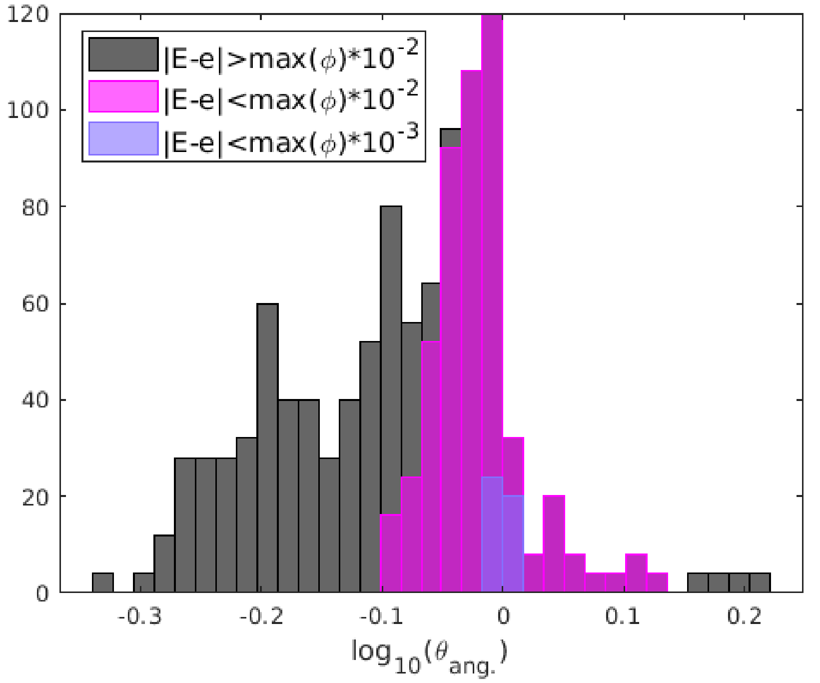

Figure 7.4 $\log_{10}\theta_{ang.}^{(i,j)}$ Histogram for LeR/TE-AD Estimator, H^0 Case 1, $N_X = N_Y = 32$

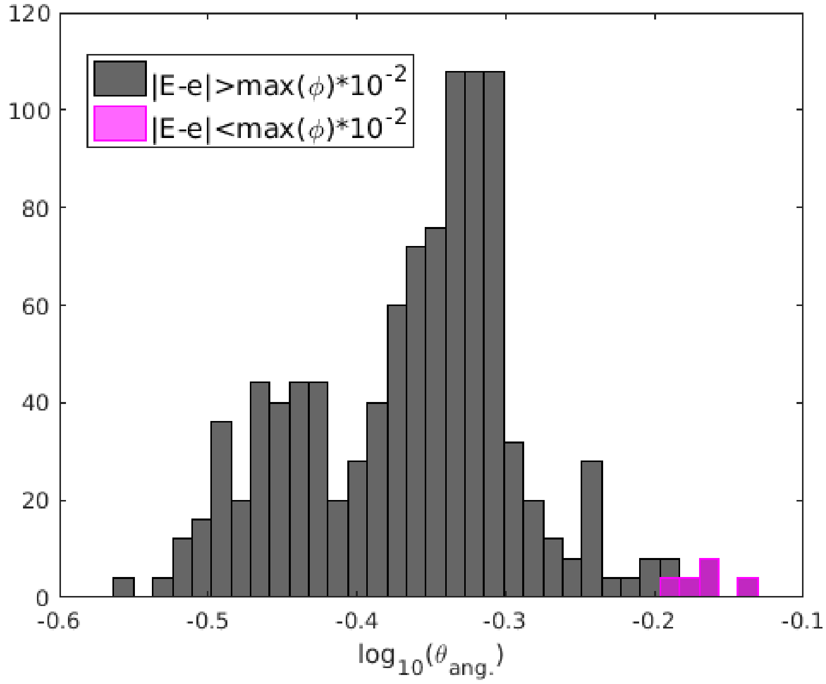

Figure 7.5 $\log_{10}\theta_{ang.}^{(i,j)}$ Histogram for RW Estimator, H^0 Case 1, $N_X = N_Y = 32$

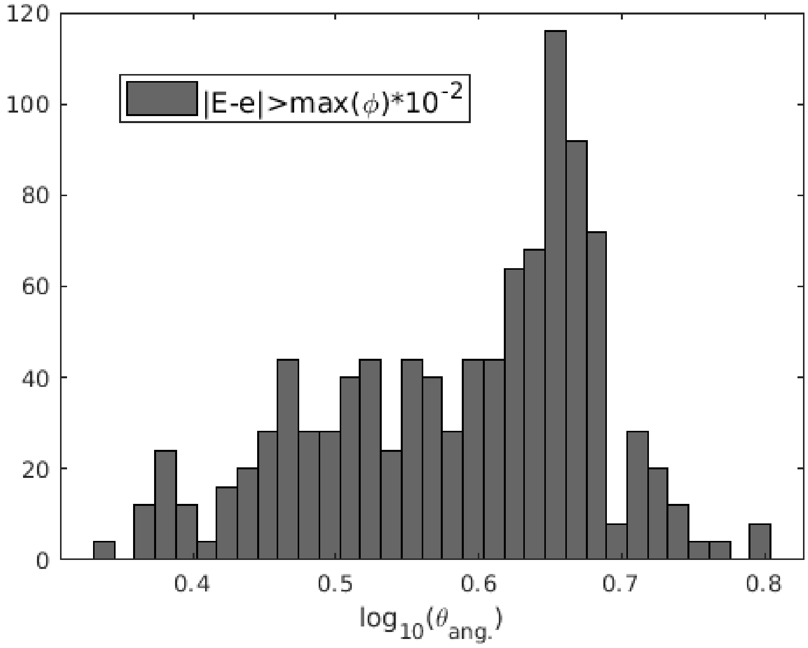

Figure 7.6 $\log_{10}\theta_{ang.}^{(i,j)}$ Histogram for DAZ Indicator, H^0 Case 1, $N_X = N_Y = 32$

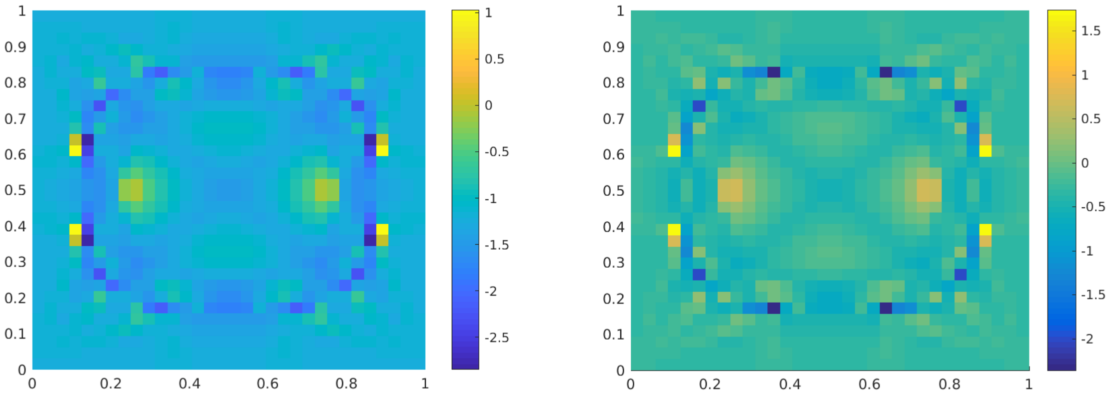

Figure 7.7 $\log_{10}\theta_{sca.}^{(i,j)}$ for LeR/TE-AD Estimator, H^0 Case 1, $N_X = N_Y = 32$

Figure 7.8 $\log_{10}\theta_{sca.}^{(i,j)}$ for RW Estimator, H^0 Case 1, $N_X = N_Y = 32$

whereas the minimum and maximum for H^0 Case 1 are near -0.8 and 0.4, respectively. The SCs are much more influential in the H^0 case *vis-a-vis* the H^1 case. This is because the true residual on cells that neighbor the SCs increases with mesh refinement, and the TE-AD residual approximation is unable to capture this trend. This means that the TE-AD residual approximation in these cells will get worse as the mesh is refined. While these cells make up a relatively small fraction of the total cells in the mesh, the inability to capture this extremely large source term in Eq. 3.4 (relative to the magnitude of the residual elsewhere in the domain) correctly for the error's transport-like problem results in a worse error estimate for H^0 cases. The discontinuity

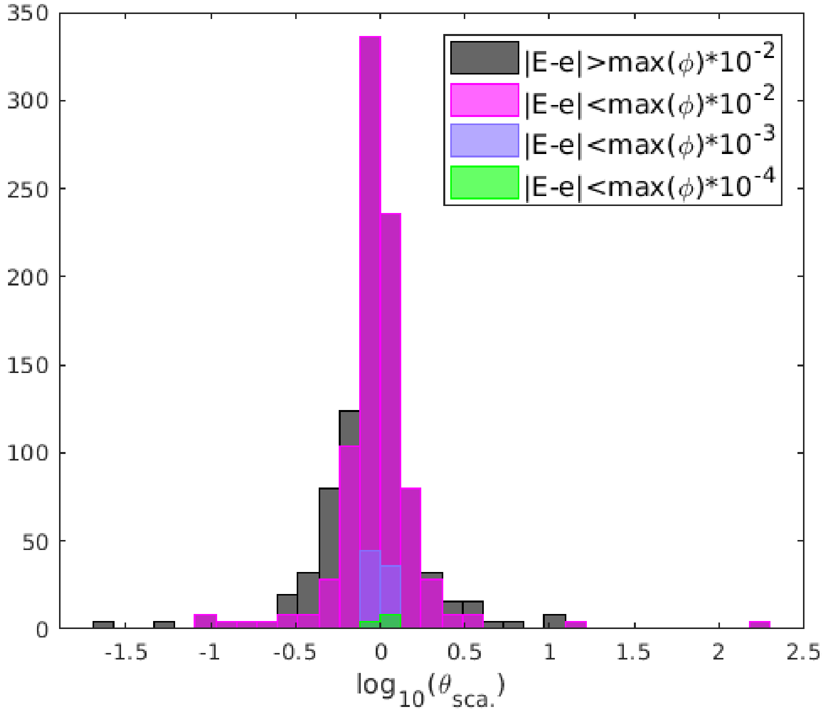

Figure 7.9 $\log_{10} \theta_{sca.}^{(i,j)}$ Histogram for LeR/TE-AD Estimator, H^0 Case 1, $N_X = N_Y = 32$

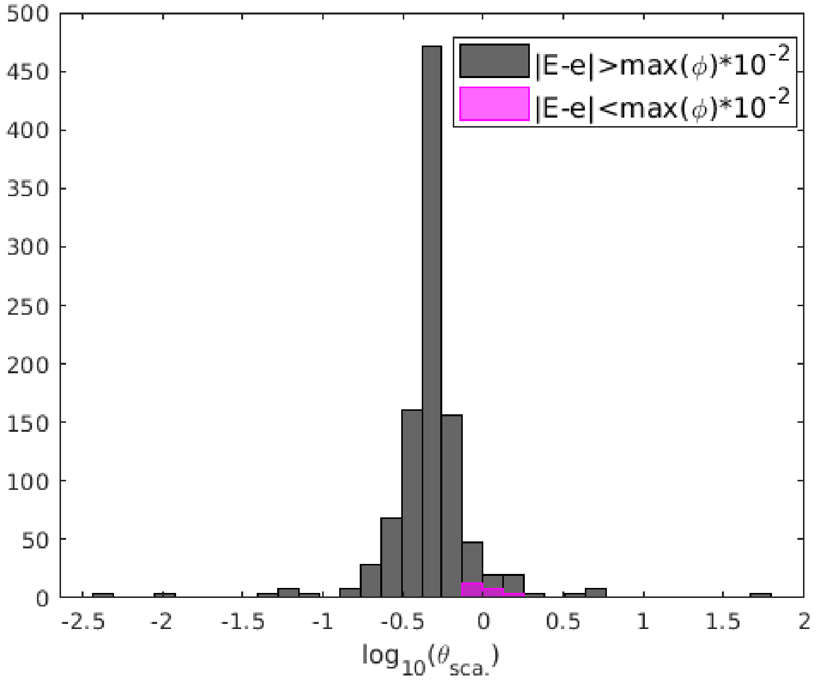

Figure 7.10 $\log_{10} \theta_{sca.}^{(i,j)}$ Histogram for RW Estimator, H^0 Case 1, $N_X = N_Y = 32$

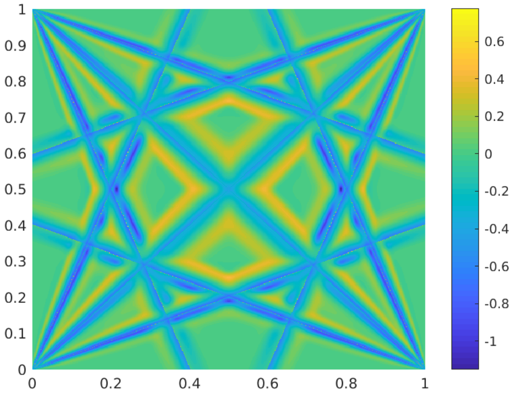

Figure 7.11 $\log_{10}\theta^{(i,j)}_{ang.}$ for LeR/TE-AD Estimator, H^0 Case 1, $N_X = N_Y = 512$

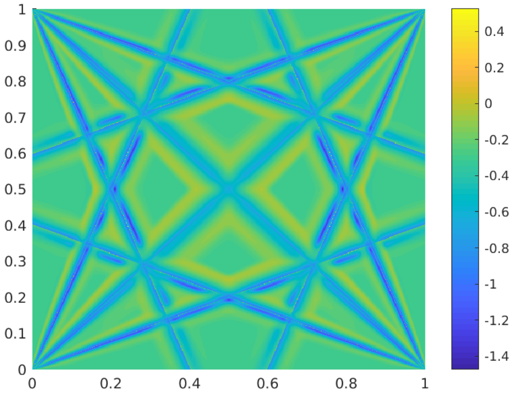

Figure 7.12 $\log_{10}\theta^{(i,j)}_{ang.}$ for RW Estimator, H^0 Case 1, $N_X = N_Y = 512$

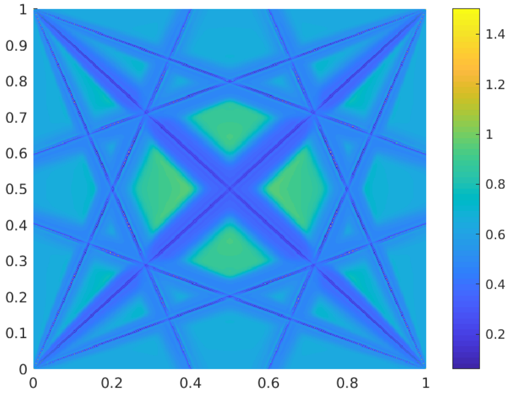

Figure 7.13 $\log_{10}\theta^{(i,j)}_{ang.}$ for DAZ Indicator, H^0 Case 1, $N_X = N_Y = 512$

in the solution itself is also significant, as this will further break the Taylor-Expansion approximations used to approximate derivatives and the residual. Finally, the lower continuity order of the true solution will cause the DGFEM-0 solution to be poorer, leading to worse *a posteriori* approximation of derivatives.

The scalar effectivities for the refined mesh are plotted over the domain and tallied in histogram form, Figures 7.17-7.20. Once again, both scalar estimates are less accurate than their angular counterparts, and, like the fine-mesh H^1 cases, they have extremely inaccurate outliers and larger over- and under-estimation tails.

Figures 7.21-7.22, show the global convergence with mesh refinement of the true error and estimator angular effectivity for this problem configuration, while Figures 7.23-7.24 show the convergence of the scalar effectivity. One noteworthy feature of the convergence plots is that the approximated residual actually *increases* with decreasing mesh size. This is actually in

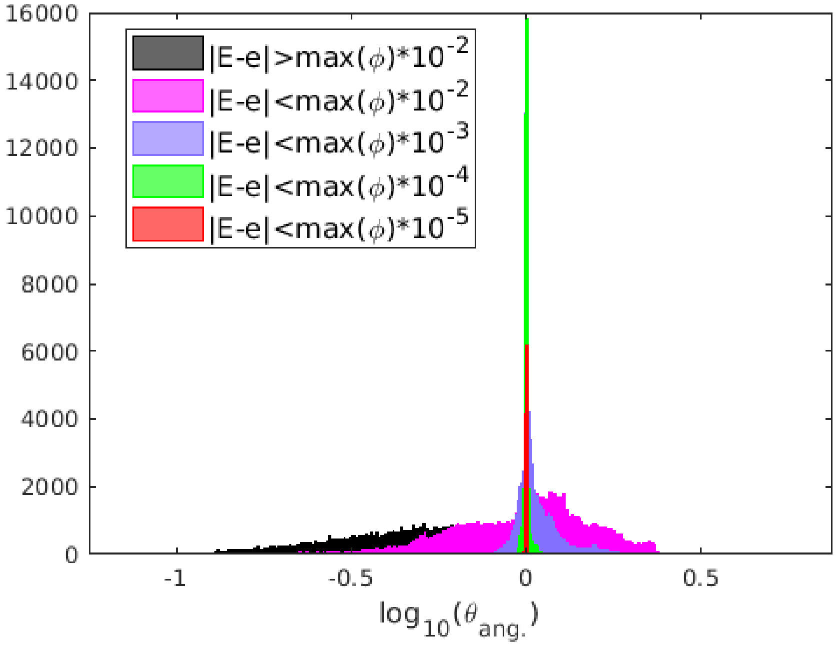

Figure 7.14 $\log_{10}\theta_{ang.}^{(i,j)}$ Histogram for LeR/TE-AD Estimator, H^0 Case 1, $N_X = N_Y = 512$

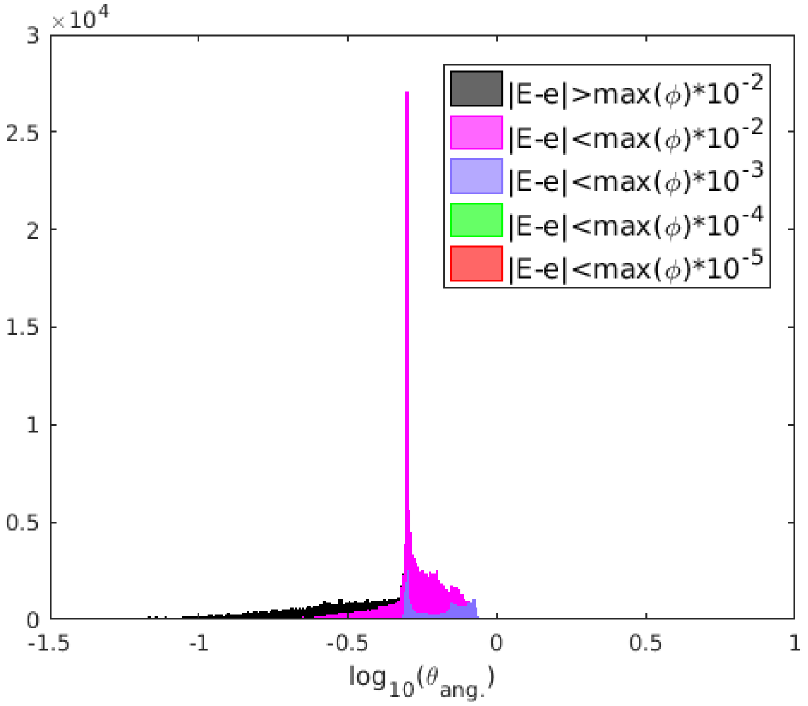

Figure 7.15 $\log_{10}\theta_{ang.}^{(i,j)}$ Histogram for RW Estimator, H^0 Case 1, $N_X = N_Y = 512$

agreement with the behavior of the true residual, and it happens in H^0 cases because the local residual in cells that are directly downwind of SCs increase with $\mathcal{O}(h^{-1})$ due to the discontinuity

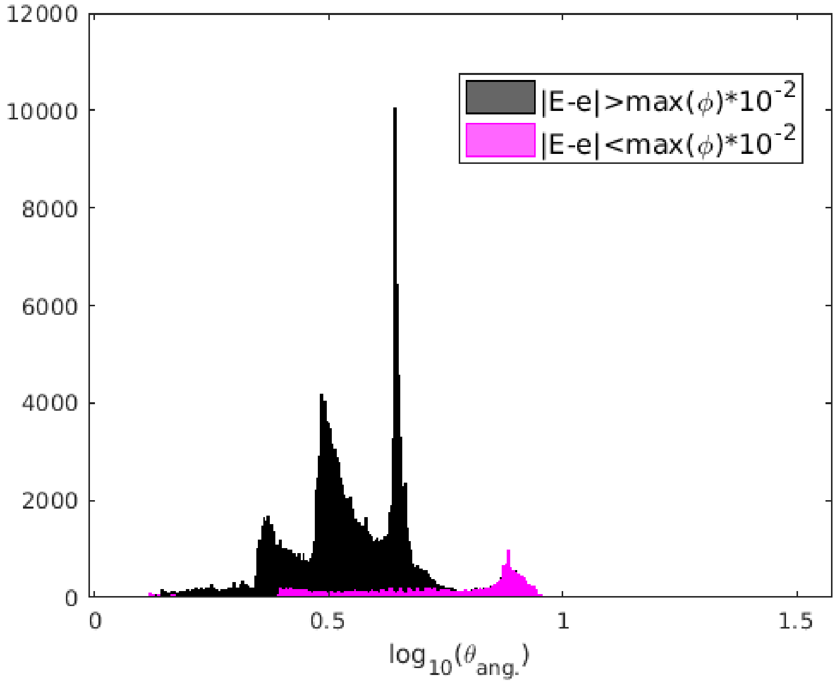

Figure 7.16 $\log_{10}\theta^{(i,j)}_{ang.}$ Histogram for DAZ Indicator, H^0 Case 1, $N_X = N_Y = 512$

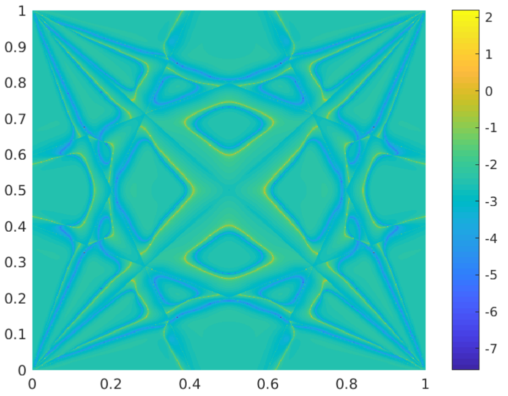

Figure 7.17 $\log_{10}\theta^{(i,j)}_{sca.}$ for LeR/TE-AD Estimator, H^0 Case 1, $N_X = N_Y = 512$

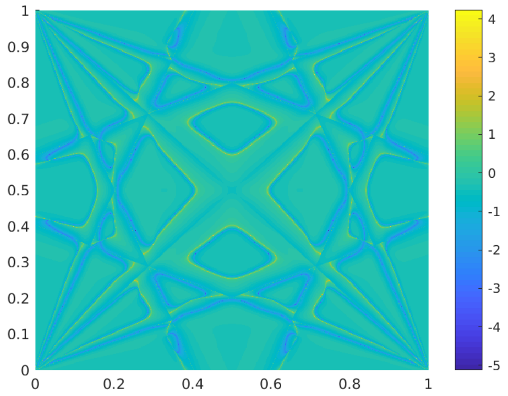

Figure 7.18 $\log_{10}\theta^{(i,j)}_{sca.}$ for RW Estimator, H^0 Case 1, $N_X = N_Y = 512$

in the true solution along the SCs. A similar analysis to that done in Section 3.3 for H^1 cases can be done to show that the leading order of convergence of the residual will be $\mathcal{O}(h^{-1/2})$ as the mesh size is decreased. At fine meshes the global LeR/TE-AD and RW estimators trend slightly away from the true error, which was not seen in any H^1 case. Figure 7.21 shows that this is because the true error convergence order decreases slightly after it has apparently reached asymptotic convergence. For this case, the global DAZ estimator bounds the true error, although the theory does not guarantee this for H^0 problems [19].

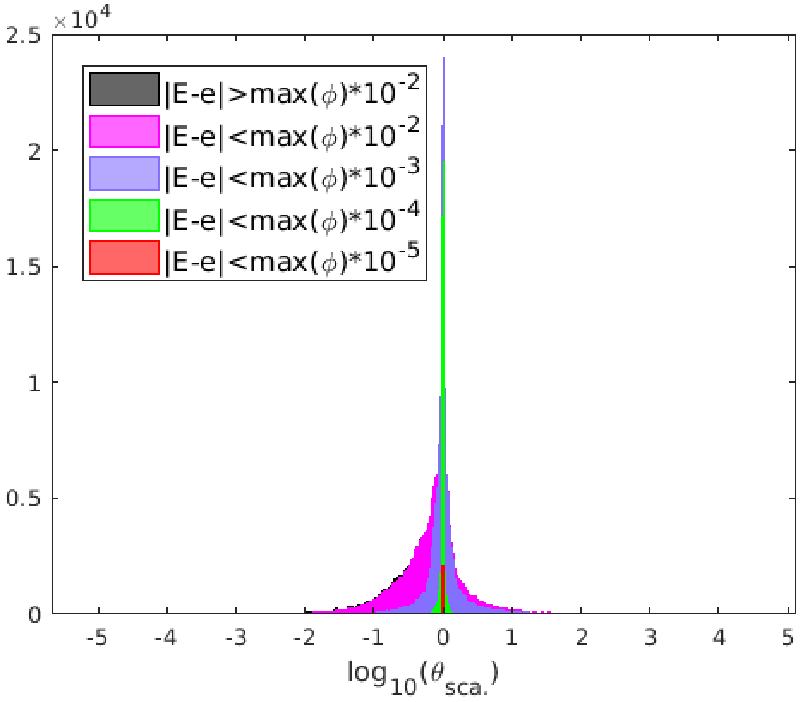

Figure 7.19 $\log_{10}\theta_{sca.}^{(i,j)}$ Histogram for LeR/TE-AD Estimator, H^0 Case 1, $N_X = N_Y = 512$

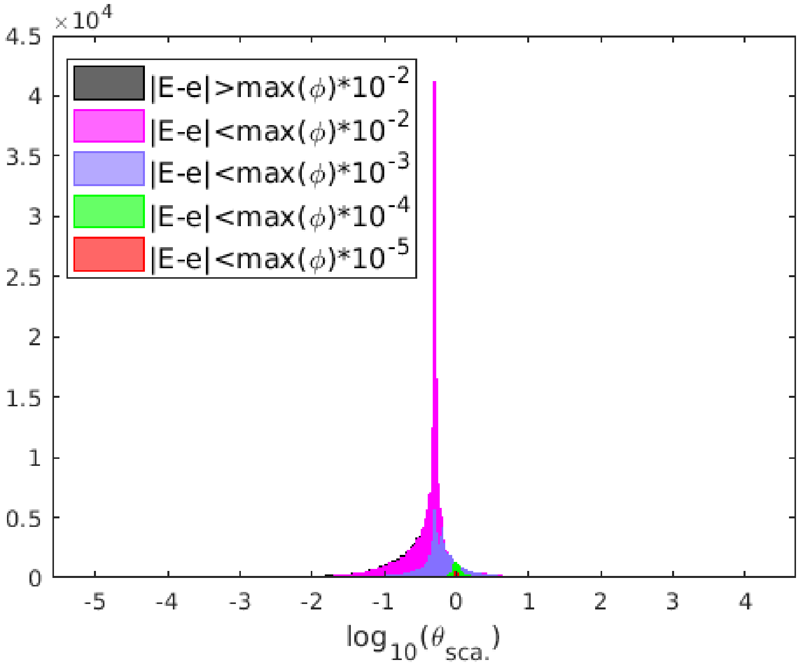

Figure 7.20 $\log_{10}\theta_{sca.}^{(i,j)}$ Histogram for RW Estimator, H^0 Case 1, $N_X = N_Y = 512$

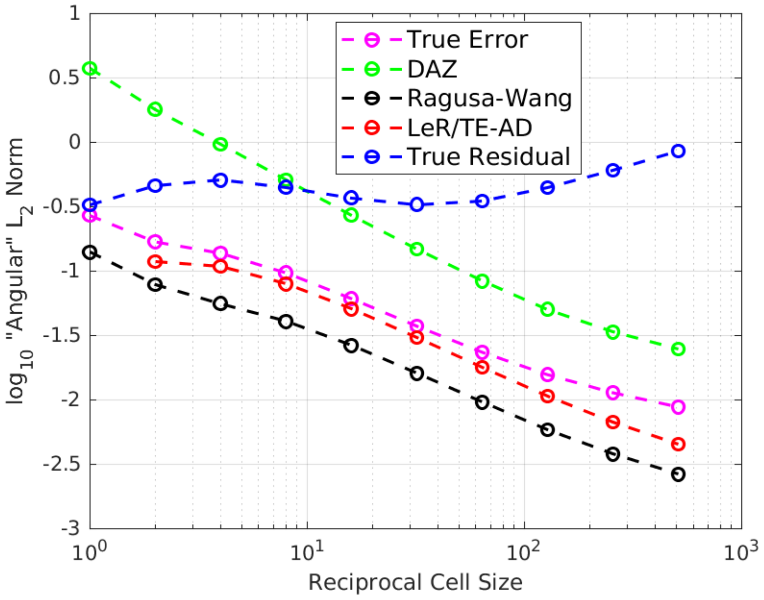

Figure 7.21 Angular Error/Estimator L_2 Norm Convergence for H^0 Case 1

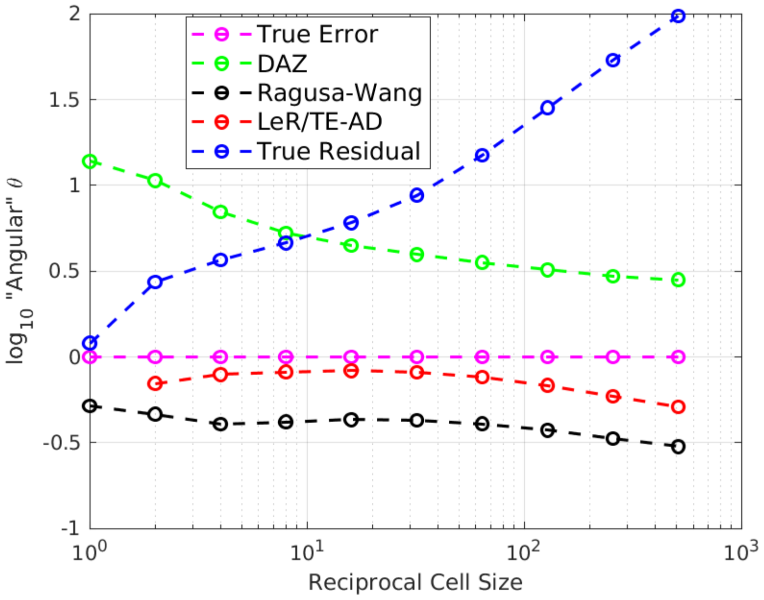

Figure 7.22 Angular Effectivity Convergence for H^0 Case 1

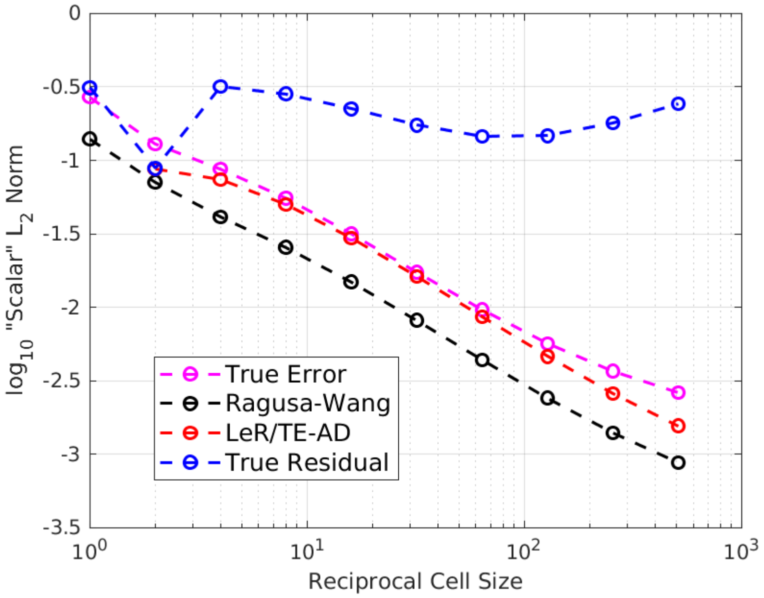

Figure 7.23 Scalar Error/Estimator L_2 Norm Convergence for H^0 Case 1

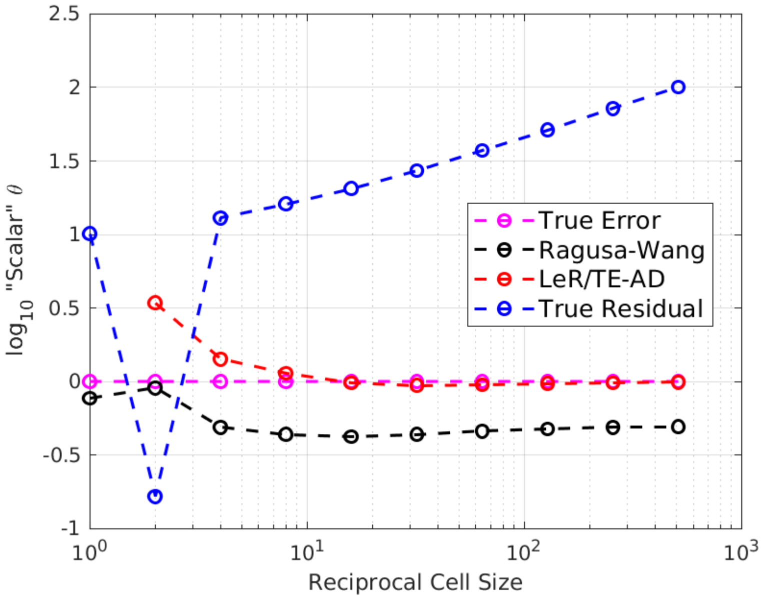

Figure 7.24 Scalar Effectivity Convergence for H^0 Case 1

7.2 H^0 General Behavior

As in the H^1 cases, certain global quality indicators are plotted here with varying problem parameters.

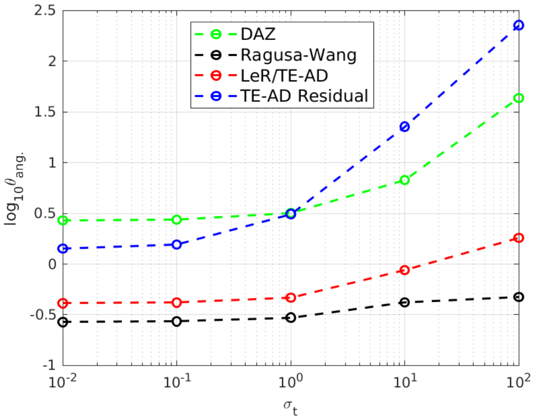

Figure 7.25 Global Angular Effectivity vs. σ_t, $c = 0.1$, $N_X = N_Y = 32$, H^0

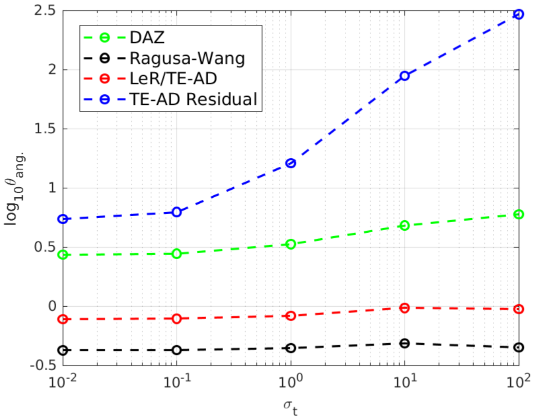

Figure 7.26 Global Angular Effectivity vs. σ_t, $c = 0.1$, $N_X = N_Y = 512$, H^0

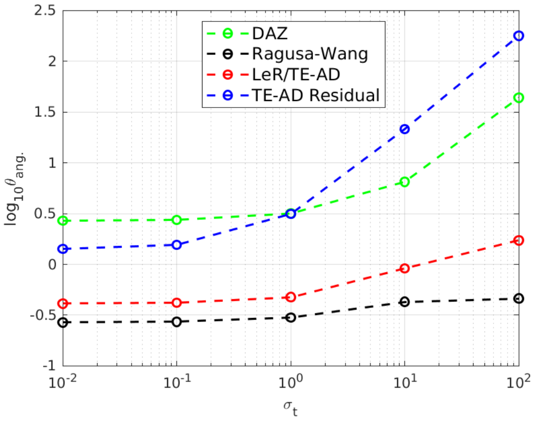

Figure 7.27 Global Angular Effectivity vs. σ_t, $c = 0.5$, $N_X = N_Y = 32$, H^0

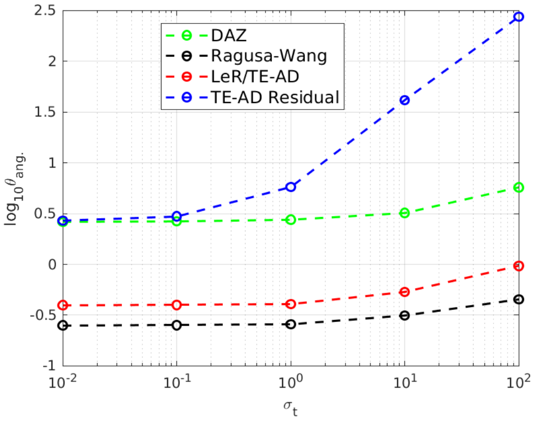

Figure 7.28 Global Angular Effectivity vs. σ_t, $c = 0.5$, $N_X = N_Y = 512$, H^0

Figures 7.25-7.30 show the global angular effectivity with varying optical thickness for scattering ratios of $c = 0.1$, $c = 0.5$, and $c = 0.9$ and for $N_X = N_Y = 32$ and $N_X = N_Y = 512$. As a global error estimate, the LeR/TE-AD estimator is once again the most accurate. Unlike

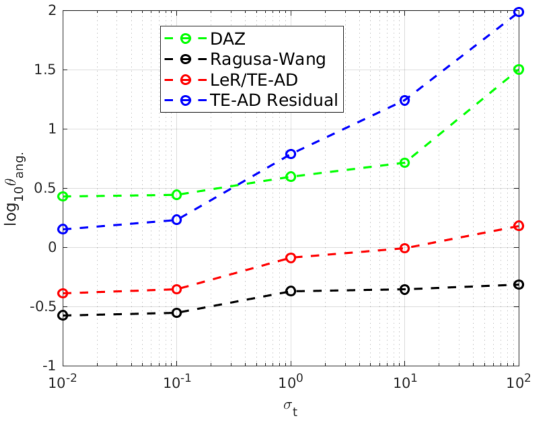

Figure 7.29 Global Angular Effectivity vs. σ_t, $c = 0.9$, $N_X = N_Y = 32$, H^0

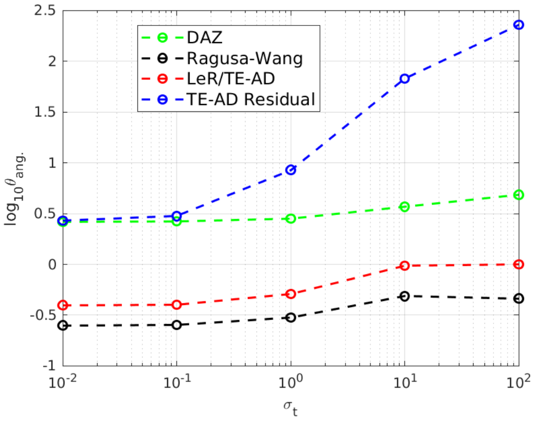

Figure 7.30 Global Angular Effectivity vs. σ_t, $c = 0.9$, $N_X = N_Y = 512$, H^0

the H^1 cases, the RW estimator has varying degrees of underestimation bias depending on the problem parameters for the H^0 problem set. The convergence order of the global L_2 error norm for DGFEM-0 for a problem with a discontinuous solution is $p = 0.5$, which corresponds to a predicted underestimation bias of $\log_{10}\theta_{ang.} = -0.53$. This is observed in problems where the SCs are more influential, such as low-to-medium optical thickness and low-to-medium scattering ratio. However, when the SC effects are mitigated (optically thick and large scattering ratio), the numerical solution evidently behaves like an H^1 problem, and the global order of convergence is closer to $p = 1$, thus the associated underestimation bias $\log_{10}\theta_{ang.} = -0.3$. However, in cases where the RW estimator exhibits the predicted H^0 bias in the global estimate, the local estimator does not peak at this value. Instead it peaks close to perfect agreement, as will be seen when accuracy metrics are plotted later. For these cases the global DAZ indicator bounds the global error.

Figures 7.31-7.36 show the fraction of local estimates that are cautious. All estimators, with the exception of DAZ, are relatively insensitive to changes in scattering ratio. All estimators except DAZ generally become more cautious as the optical thickness is increased and the mesh is refined. The LeR/TE-AD estimator has about 50% of its estimates cautious on the fine mesh, which is expected, since the estimator is centered about exact estimation. Like in the H^1 cases, the RW estimator is not locally cautious because of the intrinsic bias.

Figures 7.37-7.42 show the fraction of local effectivities that are within some specified bound. The accuracy results for the H^0 cases are noticeably different for low-to-medium optical thicknesses than in the H^1 cases, Figures 6.76-6.81. The RW estimator performs superior to the LeR/TE-AD estimator for most of the metrics at low-to-medium scattering ratios and low-to-medium optical thicknesses. The reason for this is two-fold. First, the RW estimator's accuracy in H^0 problems with prominent SC effects is more superior than when the SCs are prominent (though precision and global accuracy are inferior). Second, in problems that have low

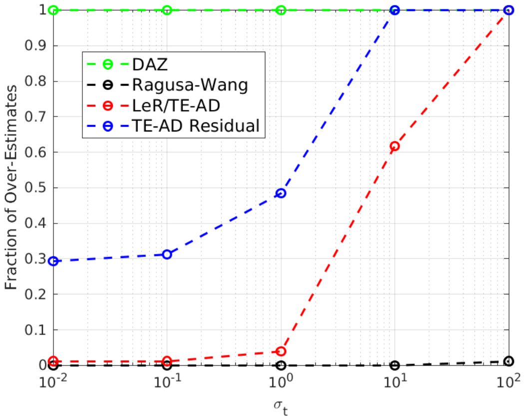

Figure 7.31 Fraction of cells with $\theta_{ang.}^{(i,j)} - 1 \geq 0$ vs. σ_t, $c = 0.1$, $N_X = N_Y = 32$, H^0

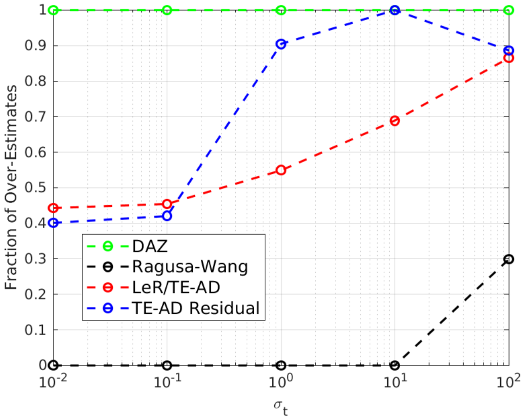

Figure 7.32 Fraction of cells with $\theta_{ang.}^{(i,j)} - 1 \geq 0$ vs. σ_t, $c = 0.1$, $N_X = N_Y = 512$, H^0

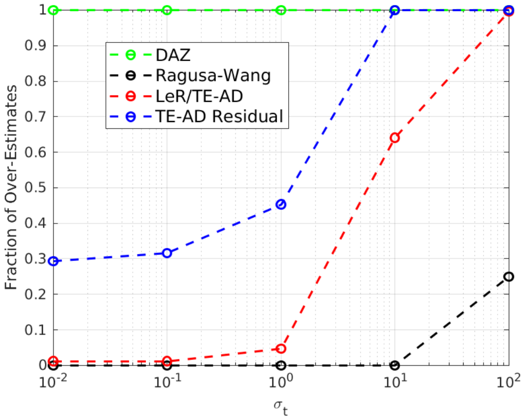

Figure 7.33 Fraction of cells with $\theta_{ang.}^{(i,j)} - 1 \geq 0$ vs. σ_t, $c = 0.5$, $N_X = N_Y = 32$, H^0

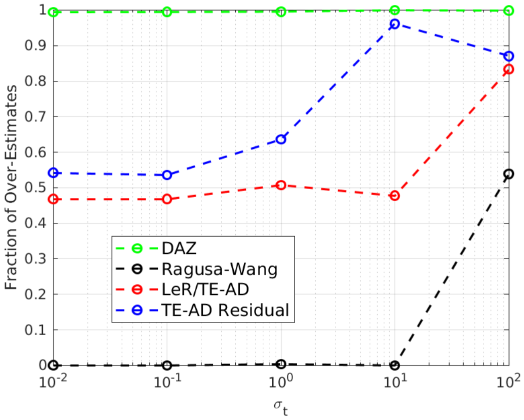

Figure 7.34 Fraction of cells with $\theta_{ang.}^{(i,j)} - 1 \geq 0$ vs. σ_t, $c = 0.5$, $N_X = N_Y = 512$, H^0

scattering ratios and optical thicknesses, the magnitude on the discontinuity in the true solution will be larger and associated SC effects worse, thus resulting in a poorer TE-AD residual approximation and associated LeR/TE-AD estimate.

Figures 7.43-7.48 show the standard deviation as an indication of each estimator/indicator's quality as a shape estimate. Once again there is a stark contrast between the H^0 plots and H^1 plots, Figures 6.82-6.87, namely the DAZ indicator is a better shape estimate for low-to-medium optical thicknesses than the RW and LeR/TE-AD estimators. In comparison to the H^1 plots, it appears that for low-to-medium optical thicknesses the RW and LeR/TE-AD estimators have much larger standard deviations, while the DAZ indicator is relatively unaffected by the change in the true solution's continuity order. At a higher scattering ratio the LeR/TE-AD and RW estimators have comparable standard deviations at most optical thicknesses.

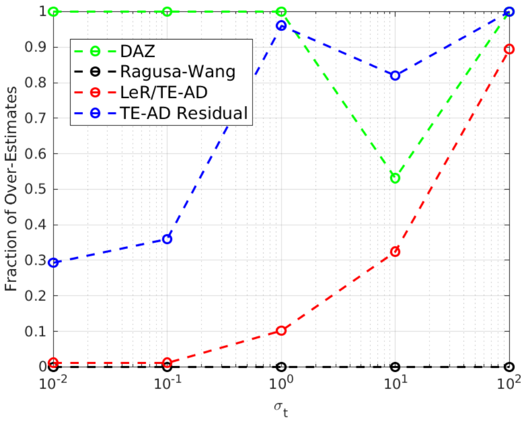

Figure 7.35 Fraction of cells with $\theta_{ang.}^{(i,j)} - 1 \geq 0$ vs. σ_t, $c = 0.9$, $N_X = N_Y = 32$, H^0

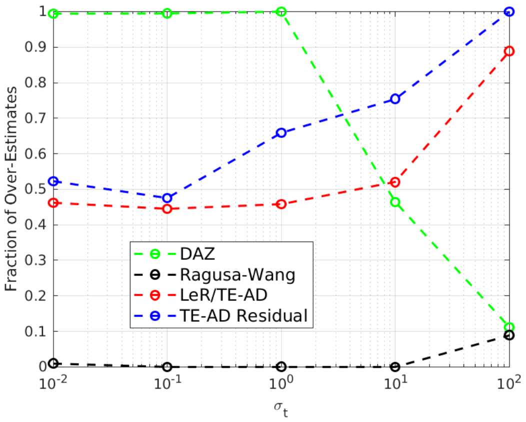

Figure 7.36 Fraction of cells with $\theta_{ang.}^{(i,j)} - 1 \geq 0$ vs. σ_t, $c = 0.9$, $N_X = N_Y = 512$, H^0

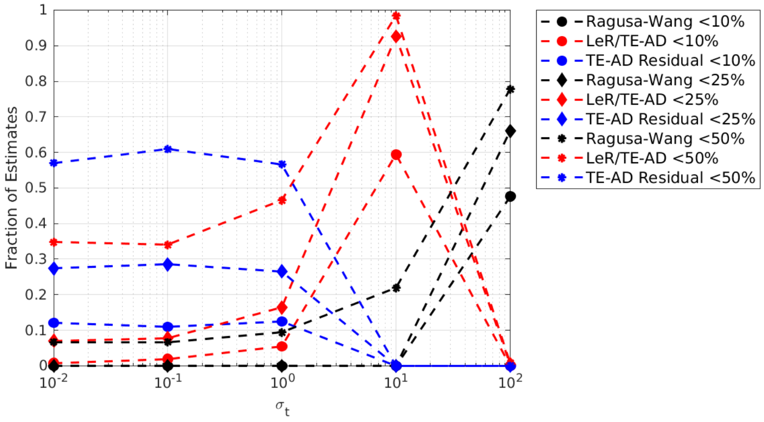

Figure 7.37 Fraction of cells with $|\theta_{ang.}^{(i,j)} - 1| \leq$ specified bounds vs. σ_t, $c = 0.1$, $N_X = N_Y = 32$, H^0

Figures 7.49-7.54 show the post-solution computation time. The relative computation times are mostly invariant with change in the continuity order. Ultimately, like the H^1 cases, the estimates that require additional transport solves will have computation times that mimic the computation time for the numerical solution. Therefore, one would expect the continuity order to affect the estimator computation time only insofar as it affects the computation time of the discrete variable transport solution.

7.3 H^0 Conclusions

Overall, the results for the H^0 cases are not entirely different than the H^1 cases. Like the H^1 cases the global LeR/TE-AD estimator is the most accurate of all the estimators, although it is not cautious. The RW global estimator is not cautious either, although it is not as likely

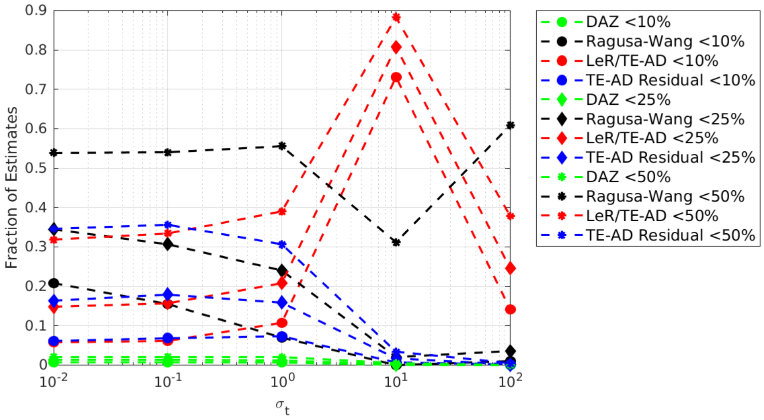

Figure 7.38 Fraction of cells with $|\theta_{ang.}^{(i,j)} - 1| \leq$ specified bounds vs. σ_t, $c = 0.1$, $N_X = N_Y = 512$, H^0

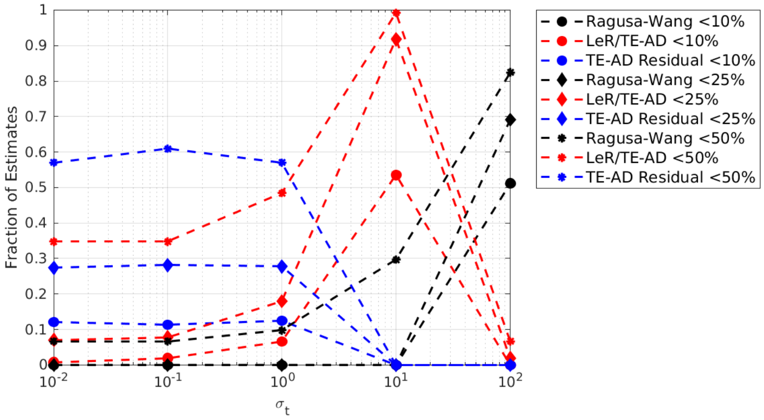

Figure 7.39 Fraction of cells with $|\theta_{ang.}^{(i,j)} - 1| \leq$ specified bounds vs. σ_t, $c = 0.5$, $N_X = N_Y = 32$, H^0

to exhibit the predicted bias in cases where the solution discontinuity effects are prevalent throughout the domain. The global DAZ indicator is cautious for all H^0 cases observed, although this is not a mathematical certainty. However, this shows that the DAZ indicator is still useful for H^0 cases, especially since it is the most computationally affordable indicator/estimator presented in this work. The local DAZ indicator continues to overestimate the true error for most cases as well. The LeR/TE-AD estimator is consistently more locally cautious than the RW estimator, regardless of optical thickness or scattering ratio. Unlike the H^1 cases, where the LeR/TE-AD estimator had a substantial advantage in terms of accuracy, the accuracy of the LeR/TE-AD estimator *vis-a-vis* the RW estimator is highly dependent on the scattering ratio due to the angular flux discontinuities inherent to H^0 problems, although at larger optical thicknesses the LeR/TE-AD estimator is superior. Because the true and TE-AD approximated residuals increase locally near the SCs and globally as a norm with decreasing mesh size for H^0

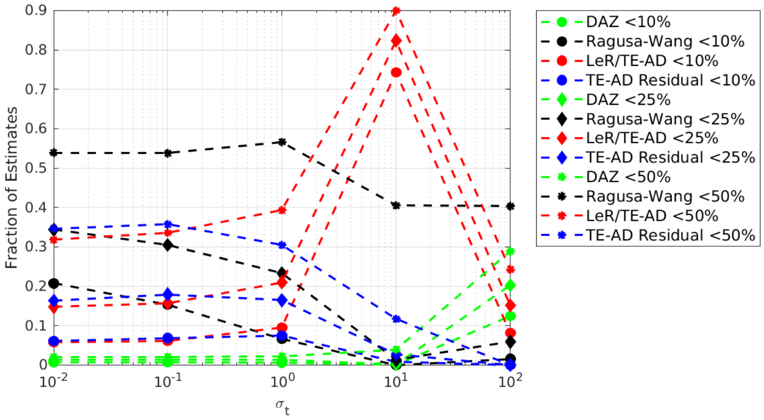

Figure 7.40 Fraction of cells with $|\theta_{ang.}^{(i,j)} - 1| \leq$ specified bounds vs. σ_t, $c = 0.5$, $N_X = N_Y = 512$, H^0

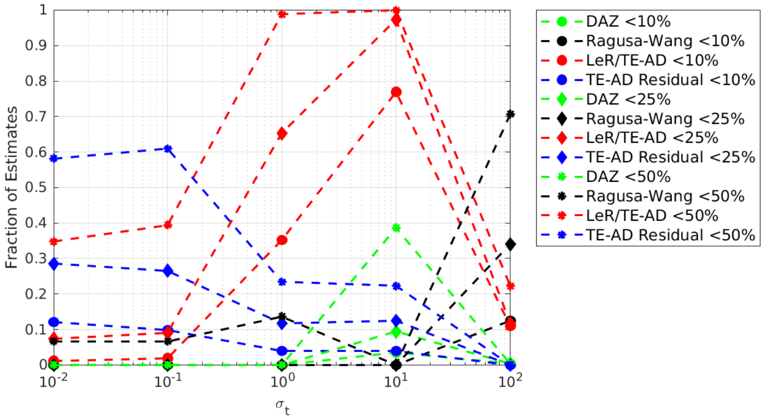

Figure 7.41 Fraction of cells with $|\theta_{ang.}^{(i,j)} - 1| \leq$ specified bounds vs. σ_t, $c = 0.9$, $N_X = N_Y = 32$, H^0

cases, it would not be recommended to rely on the residual approximation as an error estimate when the problem is H^0, although it does have some desirable features. Namely, the TE-AD residual approximation globally bounds the true error in all cases; however, it is not locally cautious in all cells.

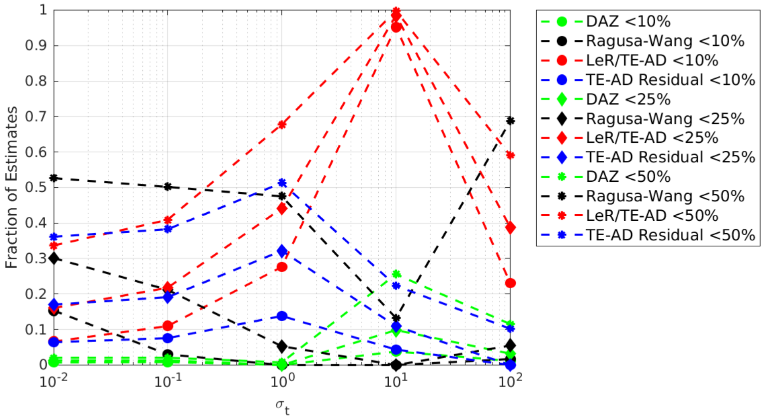

Figure 7.42 Fraction of cells with $|\theta_{ang.}^{(i,j)} - 1| \leq$ specified bounds vs. σ_t, $c = 0.9$, $N_X = N_Y = 512$, H^0

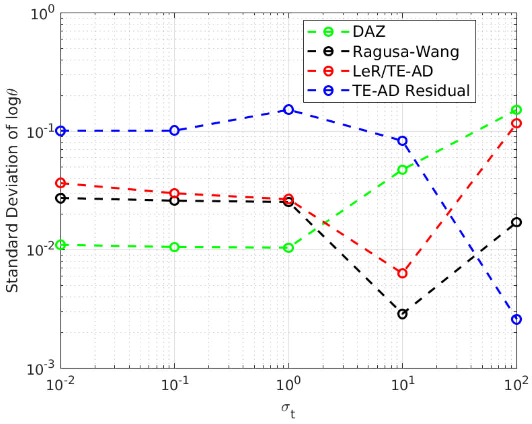

Figure 7.43 Standard deviation of $\log_{10} \theta_{ang.}^{(i,j)}$ vs. σ_t, $c = 0.1$, $N_X = N_Y = 32$, H^0

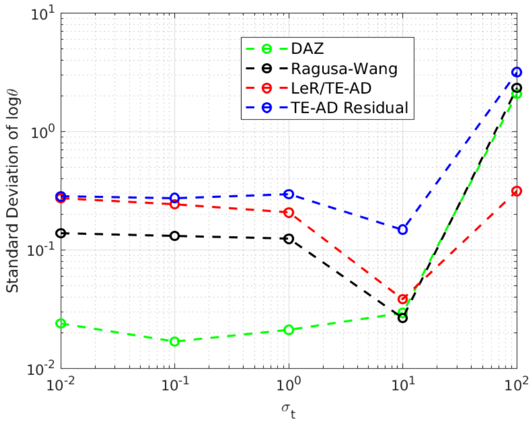

Figure 7.44 Standard deviation of $\log_{10} \theta_{ang.}^{(i,j)}$ vs. σ_t, $c = 0.1$, $N_X = N_Y = 512$, H^0

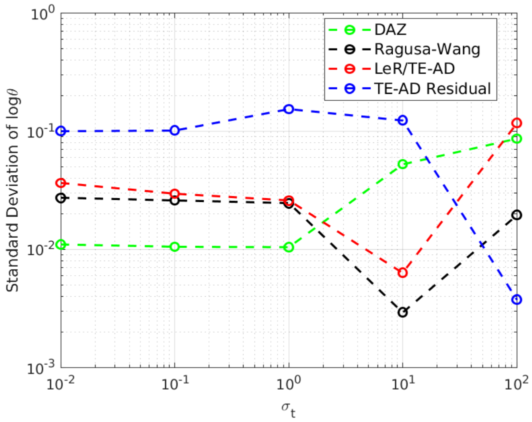

Figure 7.45 Standard deviation of $\log_{10} \theta_{ang.}^{(i,j)}$ vs. σ_t, $c = 0.5$, $N_X = N_Y = 32$, H^0

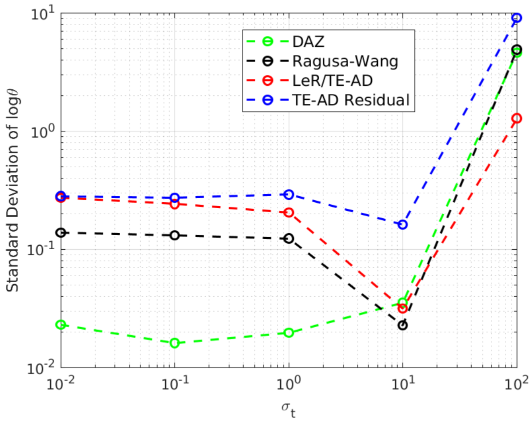

Figure 7.46 Standard deviation of $\log_{10} \theta_{ang.}^{(i,j)}$ vs. σ_t, $c = 0.5$, $N_X = N_Y = 512$, H^0

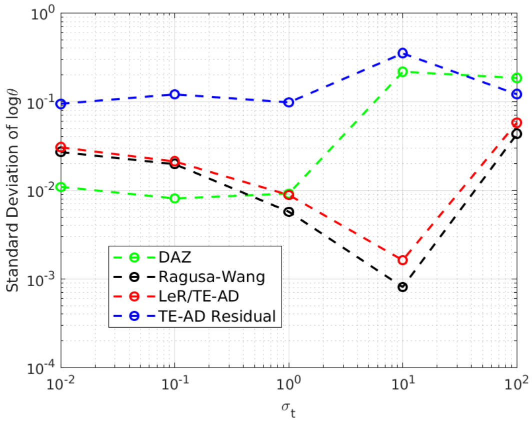

Figure 7.47 Standard deviation of $\log_{10}\theta^{(i,j)}_{ang.}$ vs. σ_t, $c = 0.9$,
$N_X = N_Y = 32,\ H^0$

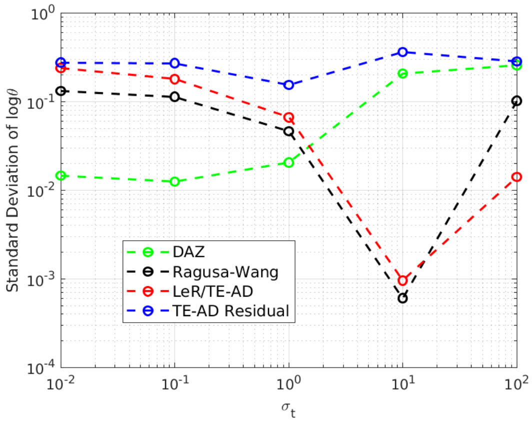

Figure 7.48 Standard deviation of $\log_{10}\theta^{(i,j)}_{ang.}$ vs. σ_t, $c = 0.9$,
$N_X = N_Y = 512,\ H^0$

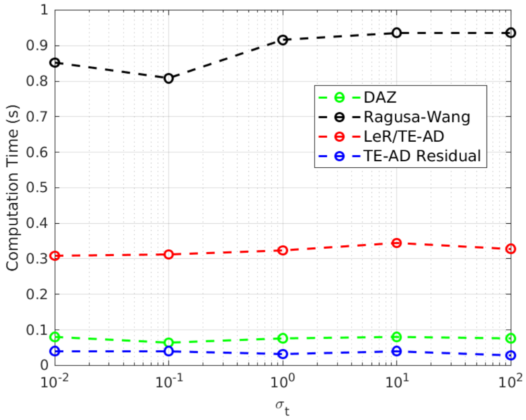

Figure 7.49 Computation time vs. σ_t, $c = 0.1$,
$N_X = N_Y = 32,\ H^0$

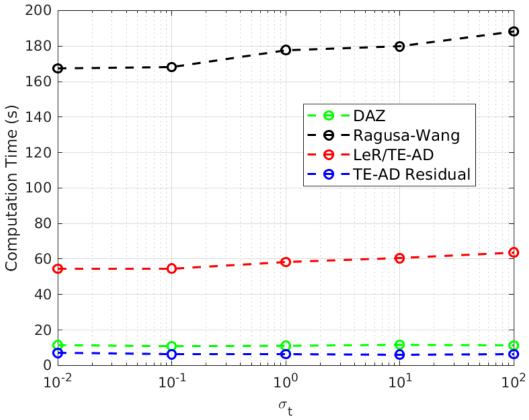

Figure 7.50 Computation time vs. σ_t, $c = 0.1$,
$N_X = N_Y = 512,\ H^0$

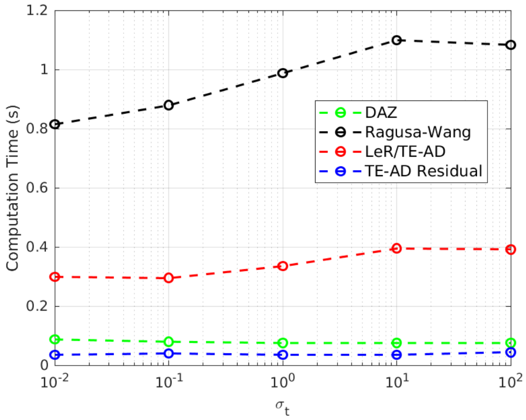

Figure 7.51 Computation time vs. σ_t, $c = 0.5$,
$N_X = N_Y = 32,\ H^0$

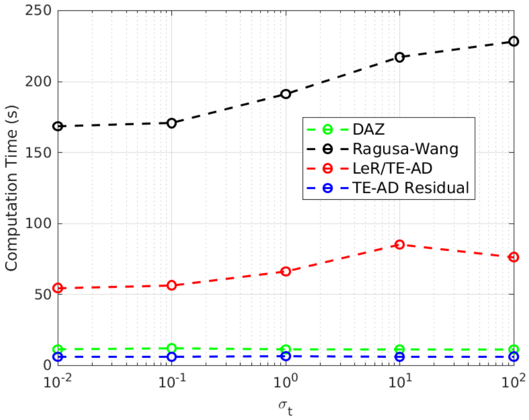

Figure 7.52 Computation time vs. σ_t, $c = 0.5$,
$N_X = N_Y = 512,\ H^0$

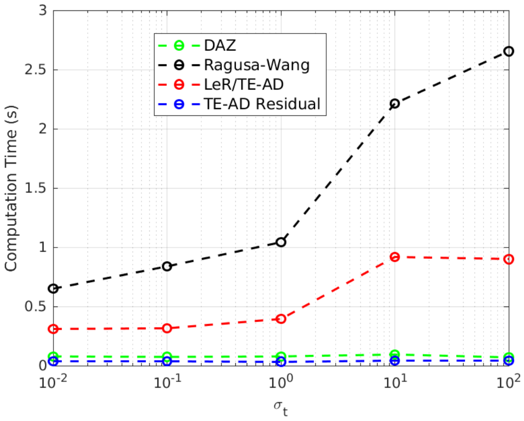

Figure 7.53 Computation time vs. σ_t, $c = 0.9$, $N_X = N_Y = 32$, H^0

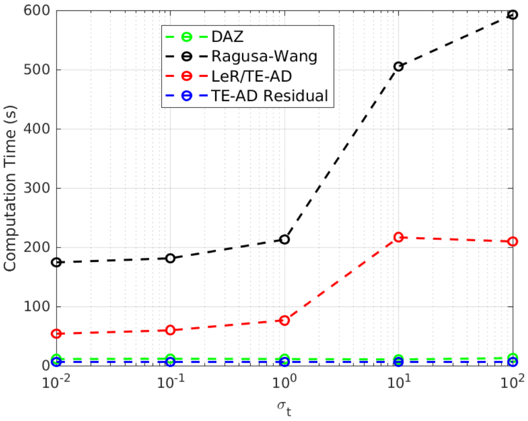

Figure 7.54 Computation time vs. σ_t, $c = 0.9$, $N_X = N_Y = 512$, H^0

Chapter 8

Conclusions

The residual source estimator has been derived for local and global spatial error estimation of the DGFEM-0 solution of S_N transport equation. By using MMS, this work has empirically proven the feasibility of using a residual approximation as an input to the residual source estimator by using the true residual as a fixed source in a transport-like problem to calculate the true error. A residual approximation method using Taylor Expansions to approximate the true solution has been demonstrated for DGFEM-0, as has the accompanying point-wise derivative approximation. By evaluating the LeR/TE-AD estimator, as well as the RW estimator and DAZ indicator/estimator, against true errors computed via MMS, several features of the LeR/TE-AD estimator, including advantages and disadvantages over the other estimation methods, were identified.

When implementing an error estimator, it was shown that comparing differences in the angular fluxes by implementing an "angular" norm gave the most accurate agreement with the true error. Nevertheless, the "scalar" norm is a useful quantity, and many of the trends in the angular estimators are mirrored in the behavior of the scalar estimators. For both LeR/TE-AD and RW estimators, using the scalar error estimator norm results in long "tails" of many orders of magnitude of deviation from the true scalar error norm as the mesh is refined. A major advantage the scalar form of the RW estimator has over the LeR/TE-AD estimator is that it does not require code modification or storing angular quantities in between source iterations, whereas the LeR/TE-AD estimator requires code modification to output angular quantities and storage of an angle-dependent TE-AD residual approximation regardless of whether the angular or scalar error norm is used. The DAZ estimator/indicator has no scalar norm variant as of yet, though even the angular norm version does not require storage of angular values, as these can be added to the local norm on-the-fly during the additional higher-order sweep; although, this would require code modifications.

The LeR/TE-AD estimator is a robust estimator. In H^1 problems, the LeR/TE-AD estimator is consistently the most accurate estimator regardless of scattering ratio and optical thickness, with very few exceptions. It gives good agreement with the true error away from SCs and interference-like regions that appear near the center of the domain. Unlike the RW estimator, which has an inherent bias to underestimate, the LeR/TE-AD effectivity values are generally near the ideal value of $\theta^{(i,j)}_{ang./sca.} = 1$. It is also more locally cautious (i.e., overestimates) than the RW estimator. The local DAZ indicator is far more locally cautious than the LeR/TE-AD estimator, however, especially at low-to-medium optical thicknesses. Globally, the LeR/TE-AD estimator performed well for H^1 cases. For both angular and scalar versions it maintains similar convergence order with the true error, even at very fine meshes, and it is also consistently the most accurate global estimator. However, unlike the global DAZ estimator, the LeR/TE-AD estimator is not cautious. The TE-AD residual approximation itself globally bounds the true error in the angular sense and in the scalar sense for every case except $N_X = N_Y = 2$. This suggests some usefulness as an error bound, since any code that uses the LeR/TE-AD estimator will necessitate computation of the TE-AD residual approximation. One disadvantage to using this quantity, though, is that an accurate TE-AD residual approximation will converge with a different order than the true error.

The LeR/TE-AD estimator has some failings, though. For example, in the H^0 cases it was shown that the local angular LeR/TE-AD estimator struggles *vis-a-vis* the RW estimator when the discontinuities in the angular flux are prominent, low-to-medium optical thickness and low-to-medium scattering ratio. The cause is two-fold due to an advantage in the RW estimator and a disadvantage in the LeR/TE-AD estimator. The RW estimator is advantaged because it does not exhibit the same bias as in H^1, and the LeR/TE-AD is disadvantaged because the derivatives in the TE-AD residual expression are not well approximated due to numerical spreading of error in the solution. The true residuals in cells that border SC-intersected cells are also large due to solution discontinuity, which the TE-AD residual approximations cannot accurately capture. However, one potential advantage to the LeR/TE-AD estimator is that the residual expressions could be modified on cells intersected by or bordering cells intersected by SCs, the locations of which are known *a priori*, with *no* additional computational burden for the transport-like problem and a minor, relative to the cost of the transport-like problem, computational burden for the residual computation. SC tracking algorithms ([19]) combined with modified SC residual approximations could provide more accurate residual approximations and be applied to an H^0 problem with minimal additional cost. The LeR/TE-AD estimator still maintains some advantages in the H^0 cases, though. It is more locally cautious than the RW estimator, although still not as cautious as the global DAZ indicator. As a global estimator it remains the most accurate estimator, but it is not cautious. The global DAZ indicator is cautious, but this is not a mathematical certainty (hence calling it an "indicator").

As a shape estimate, the LeR/TE-AD estimator was excellent for H^1 cases, although it was not as robust as the RW estimator. In H^0 cases, however, it was poorer than the RW estimator and DAZ indicator. Based on the accuracy metrics, though, one can see that a significant fraction of cells have effectivities within a 50% band of relative agreement with the true error, so the LeR/TE-AD estimator is not necessarily a bad shape function in H^0.

In terms of computational cost, in practice the LeR/TE-AD estimator is regularly 2-3 times cheaper than the RW estimator. The LeR/TE-AD estimator requires some post-processing of the DGFEM-Λ solution to compute the residual and a full transport-like problem with $N_X \times N_Y \times (\Lambda + 1)^2 \times N$ unknowns, where N is the total number of discrete ordinates over all quadrants/octants. The RW estimator requires less post-processing, but the full transport problem required has $4 \times N_X \times N_Y \times (\Lambda + 1)^2 \times N$ unknowns. While the unrefined solution can be prolonged onto the uniformly refined mesh to precondition the refined solution, thus reducing the computational burden of the additional transport solve, the data structure and computational time required by the RW estimator, particularly in an angular sense, is undoubtedly largest among all compared estimators. Future work should examine the effect on estimator accuracy of reducing the convergence criterion on the additional transport problems for the LeR/TE-AD and RW estimators. The DAZ estimator/indicator is cheap, as it only requires a single high-order sweep and some post-processing, and its cost is related solely to the number of unknowns and is invariant to factors like scattering ratio and optical thickness that would otherwise affect an estimator execution time in proportion to the number of iterations required to achieve convergence. The TE-AD residual approximation is the cheapest, but its usage as an error estimate is suspect due to its different order of convergence (including failure to converge for H^0 cases) with respect to mesh refinement locally and globally.

In addition to the special residual treatment on the SCs and a relaxation of convergence criterion on additional transport solves, several avenues of further research exist. Residual approximation methods other than the TE-AD method could be highly useful, though such methods are unknown to us at this time. Also, extending the LeR/TE-AD estimator to higher order DGFEM-Λ would be vital for continued investigation of the estimator, as DGFEM-0 would not be considered sufficient for most real-life problems. It is noted that the HOPS calculated in the DAZ indicator/estimator could be implemented in a direct error estimate. The HOPS generated by the additional sweep and used to approximate the residual and jump discontinuities could rather be used as a reference solution in a p-refinement-like scheme [30]. Preliminary results have shown this to be rather accurate, and if this trend is maintained, this estimator would have the advantage of being extremely cheap and providing the potential to be used in complement with the DAZ indicator/estimator at virtually no additional cost.

BIBLIOGRAPHY

[1] Madsen, N. K. “A Posteriori Error Bounds for Numerical Solutions of the Neutron Transport Equation”. *Mathematics of Computation* **124**.27 (1973), pp. 773–780.

[2] O’Brien, S. E. “*A Posteriori Error* Estimators for the Discrete Ordinates Approximation of the One-Speed Neutron Transport Equation”. MA thesis. Raleigh, North Carolina: North Carolina State University, 2012.

[3] Babuska, I. & Rheinboldt, W. “*A-Posteriori* Error Estimates for the Finite Element Method”. *International Journal for Numerical Methods in Engineering* **12** (1978), pp. 1597–1615.

[4] Babuska, I. & Rheinboldt, W. “Error Estimates for Adaptive Finite Element Computations”. *SIAM Journal on Numerical Analysis* **15**.4 (1978), pp. 1597–1615.

[5] Grätsch, T. & Bathe, K.-J. “A posteriori error estimation techniques in practical finite element analysis”. *Computers and Structures* **83** (2005), pp. 235–265.

[6] Wang, Y. & Ragusa, J. “Application of hp Adaptivity to the Multigroup Diffusion Equations”. *Nuclear Science and Engineering* **161** (1 2009), pp. 22–48.

[7] Ragusa, J. C. & Wang, Y. “A two-mesh adaptive mesh refinement technique for S_N neutral-particle transport using a higher-order DGFEM”. *Journal of Computational and Applied Mathematics* **223** (2010), pp. 3178–3188.

[8] Solín, P. & Demkowicz, L. “Goal-oriented *hp*-adaptivity for elliptic problems”. *Comput. Methods Appl. Mech. Engrg.* **193** (2004), pp. 449–468.

[9] Wang, Y. & Ragusa, J. C. “Standard and goal-oriented adaptive mesh refinement applied to radiation transport on 2D unstructured triangular meshes”. *Journal of Computational and Applied Mathematics* **230** (2011), pp. 763–788.

[10] O’Brien, S. & Azmy, Y. Y. “*A Posteriori* Error Estimators for the Discrete Ordinates Approximation of the One-Speed Neutron Transport Equation”. *International Conference on Mathematics and Computational Methods Applied to Nuclear Science & Engineering (M&C 2013)*. Sun Valley, Idaho, USA, 2013.

[11] Führer, C. & Kanschat, G. “A Posteriori Error Control in Radiative Transfer”. *Computing* **58** (1997), pp. 317–334.

[12] Fournier, D. et al. “Analysis of a hp-Refinement Method for Solving the Neutron Transport Equation Using Two Error Estimators”. *International Conference on Mathematics and Computational Methods Applied to Nuclear Science & Engineering (M&C 2011)*. Rio de Janeiro, RJ, Brazil, 2011.

[13] Adjerid, S. & Massey, T. C. “A posteriori discontinuous finite element error estimation for two-dimensional hyperbolic problems”. *Comput. Methods Appl. Mech. Engrg.* **191** (2002), pp. 5877–5897.

[14] Bank, R. & Weiser, A. “Some A Posteriori Error Estimators for Elliptic Partial Differential Equations”. *Mathematics of Computation* **44**.170 (1985), pp. 283–301.

[15] Kuzmin, D. & Korotov, S. “Goal-oriented a posteriori error estimates for transport problems”. *Mathematics and Computers in Simulation* **80** (2010), pp. 1674–1683.

[16] Segeth, K. “A review of some a posteriori error estimates for adaptive finite element methods”. *Mathematics and Computers in Simulation* **80** (2010), pp. 1589–1600.

[17] Prudhomme, S. et al. “Analysis of a Subdomain-Based Error Estimator for Finite Element Approximations of Elliptic Problems”. *Numerical Methods for Partial Differential Equations* **20** (2 2004), pp. 165–192.

[18] Duo, J. I. et al. “A posteriori error estimator and AMR for discrete ordinates nodal transport methods”. *Annals of Nuclear Energy* **36** (2009), pp. 268–273.

[19] Duo, J. I. “Error Estimates for Nodal and Short Characteristics Spatial Approximations of Two-Dimensional Discrete Ordinates Method”. PhD thesis. University Park, PA: The Pennsylvania State University, 2008.

[20] Fournier, D. et al. “Analysis of an *a posteriori* error estimator for the transport equation with S_N and discontinuous Galerkin discretizations”. *Annals of Nuclear Energy* **38** (2011), pp. 221–231.

[21] Lathouwers, D. “Goal-oriented Spatial Adaptivity for the S_N Equations on Unstructured Triangular Meshes”. *Annals of Nuclear Energy* **38** (2011), pp. 1373–1381.

[22] Jeffers, R. et al. “Goal-based h-adaptivity of the 1-D Diamond Difference Discrete Ordinate Method”. *Journal of Computational Physics* **335** (2017), pp. 179–200.

[23] Li, Z. et al. *Numerical Solution of Differential Equations: Introduction to Finite Difference and Finite Element Methods*. Cambridge, UK: Cambridge University Press, 2017.

[24] Richter, G. R. “An Optimal-Order Error Estimate for the Discontinuous Galerkin Method”. *Mathematics of Computation* **50**.181 (1988), pp. 75–88.

[25] Lewis, E. & W.F. Miller, J. *Computational Methods of Neutron Transport*. La Grange Park, Illinois: American Nuclear Society, Inc., 1993.

[26] Schunert, S. et al. “Comparison of the Accuracy of Various Spatial Discretization Schemes of the Discrete Ordinates Equations in 2D Cartesian Geometry”. *International Conference on Mathematics and Computational Methods Applied to Nuclear Science & Engineering (M&C 2011)*. Rio de Janeiro, RJ, Brazil, 2011.

[27] Schunert, S. “Development of a Quantitative Decision Metric for Selecting the Most Suitable Discretization Method for S_N Transport Problems”. PhD thesis. Raleigh, NC: North Carolina State University, 2013.

[28] Zienkiewicz, O. & Zhu, J. “The Superconvergent Patch Recovery and *A Posteriori* Error Estimates. Part 1: The Recovery Technique”. *International Journal for Numerical Methods in Engineering* **33** (1992), pp. 1331–1364.

[29] Wang, Y. & Ragusa, J. C. “On the convergence of DFEM applied to the discrete ordinates transport equation for structured and unstructured triangular meshes”. *Nuclear Science and Engineering* **163** (2009), pp. 56–72.

[30] Warsa, J. S. & Prinja, A. K. “p-Adaptive Numerical Methods for Particle Transport”. *Transport Theory and Statistical Physics* **28** (3 1999), pp. 229–270.